RADAR

Disaster Response Search and Identification Attritable Air Vehicle

[APRI0004] Aerospace design project

LIÈGE université

AIAA
SHAPING THE FUTURE OF AEROSPACE

RADAR

Length
19.68 ft

Wingspan
21.98 ft

Cruise altitude
30,000 ft
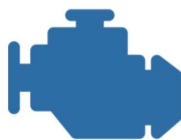
Takeoff distance
3,783 ft

Landing distance
1,695 ft

Range
4,757 nm
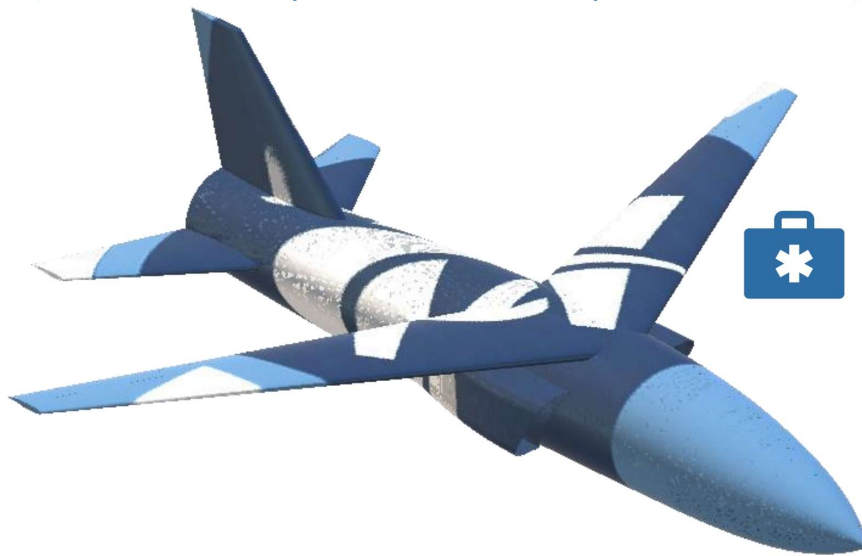
Aid packages
27

Cruise speed
467 kt

Dash speed
622 kt

Propulsion
Williams FJ33-5A

MTOW
5,485 lbs

ZFW
1,687 lbs
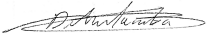
Cost
$ 1,430,800

RADAR

Disaster Response Search and Identification Attritable Air Vehicle

Student Name	AIAA Number		Signature
Emrah Altin	1339587		
Nabil Bouyakhrichan	1405833		
Wildy Mervil	1328123		
Sven Michiels	1404045		
Deogracias Mulamba	1404043		
Oumar Sow	1404044		
Alexandre Spits	1404039		
Robin Tamburrini	1406612		

Instructors: G. Dimitriadis and L. Noels

Teaching Assistants: A. Budo, A. Crovato, P. Dechamps and T. Lambert

Contents

1 Introduction

The frequency and intensity of natural disasters across the world are on the rise affecting millions of people. Thus, first responders are of the utmost importance in locating and rendering aid to those affected. Some disaster sites could be large or far away and thus the most efficient way of reaching and searching them would be to use an aircraft.

In this context, the American Institute of Aeronautics and Astronautics (AIAA) has posted a request for the design of a disaster response search and identification attributable air vehicle that can search a large area to identify those in need of help to deliver communication radios and drinking water.

The current state-of-the-art technologies are to use helicopter and in rare situations airplanes. Helicopters can take off and land in a space limited area. Due to their limited range and cruise velocity, helicopters are not able to search a large area quickly or reach disaster sites as quickly as an aircraft. For far to reach sites, piloted aircraft are used. These have the advantage of having an increased range and cruise velocity but are limited in the sites they can reach due to the potential loss of the pilot's life.

This justifies the proposed design called RADAR, as a **R**apid response **A**irborne surveillance system with **D**rop capabilities coupled with **A**ll-weather design aiming at **R**escuing victims on the ground. This is an improvement on the current technologies as it makes use of the advantages of a normal aircraft that can fly faster and search a larger area for longer while removing the pilots, therefore, allowing the aircraft to fly through non-ideal conditions. The aircraft is scheduled to enter into service in 2028.

The objective of this project is to design RADAR: a remote controlled search and rescue aircraft whos primary mission is to locate, identify and deliver water and a communication radio to the victims. The aircraft has the ability to complete tasks autonomously as well.

The overview of the report is as follows, a target market analysis, a design mission and requirements analysis and design choices and first estimations. Thereafter, component design and analysis followed by an analysis of the stability, aerodynamics, structure and performance. Finally, a trade-off study to determine on the best configuration and cost analysis to evaluate the economical viability.

Target market

The target market for search and rescue aircraft is typically government organisations and organisations that specialise in responding to emergencies.The current method of performing search and rescue using an aircraft is to use a helicopter. However, the range and flying time of helicopters are extremely limited. Thus, these organisations will require aircraft that are designed to be rapid and effective when searching and as such they feature advanced radar systems, thermal imaging cameras and high-speed communication systems. These aircraft need to be able to operate in non-ideal conditions to reach the disaster victims. Some countries of the world are more vulnerable to natural disasters due to their location, climate and topography.

Thus, the target market will depend on the frequency of natural disasters per year and the number of deaths as a result of the natural disasters.
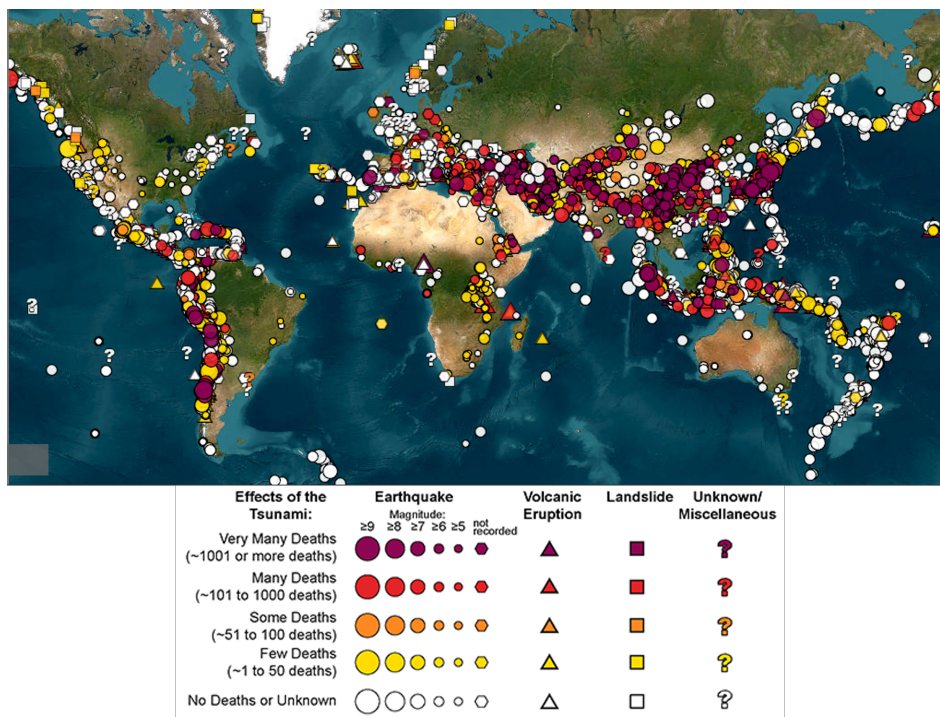
Figure 1.1: World map of natural disasters [1].

From Figure 1.1 the target market can be identified as the areas where there is a large concentration of casualties resulting from natural disasters. Currently, this is where a large majority of search and rescue operations take place. Thus, the target market is Western South America, Northern Middle East, South Asia and South East Asia.

2 Design missions and requirements

The aircraft is designed to enter the market in 2028 and accomplish the three mission goals as set out by the AIAA. The three missions will be carried out as follows. The main mission aims to locate and identify victims who require first responder help, even in challenging flight conditions. Once the victims are identified, the objective switches to delivering water and a communication radio to connect with emergency services. The secondary mission focuses on maximizing loiter and the third mission focuses on maximizing the range with no loiter. The main mission cruise is divided into three segments. The main mission's cruise is split into three segments. The aircraft will cruise at Mach 0.86 to arrive at the scene of the disaster as quickly as possible. Afterwards, the aircraft will loiter for five hours at Mach 0.7, this is to optimize the efficiency of the engine. This approach brings the loiter speed closer to the ingress and egress speeds, minimizing the speed differential at which the engine operates. Finally, the aircraft will egress at 0.86 to return to base as quickly as possible to prepare for the next mission.

The aircraft is remotely controlled as this allows the aircraft to be used in situations where it would be too hazardous to have a pilot in the aircraft. A remote-controlled system was selected as at the current the technology needed for an aircraft to fully operate autonomously from taxi, takeoff to landing and taxi is not fully developed under certain physical conditions. The aircraft can complete certain tasks such as ingress, loitering and egress autonomously. During a disaster, it is important to take full advantage of the aircraft capabilities, including its maximum loiter duration, to gather as much information and data as possible. This data can be used to develop an accurate and comprehensive understanding of the situation, which can aid in decision-making and facilitate effective responses. However, it is still critical to ensure that the aircraft can return to the airport as quickly as possible after the loitering period to transmit the collected data, reload supplies, and prepare for the next mission.

The flight plan for the main mission is shown in Figure 2.1

Table 2.1 shows the main mission requirements from the AIAA request for proposal (RFP) that the design will have to comply with. Note: unless otherwise indicated by [T] (surpassing threshold require-
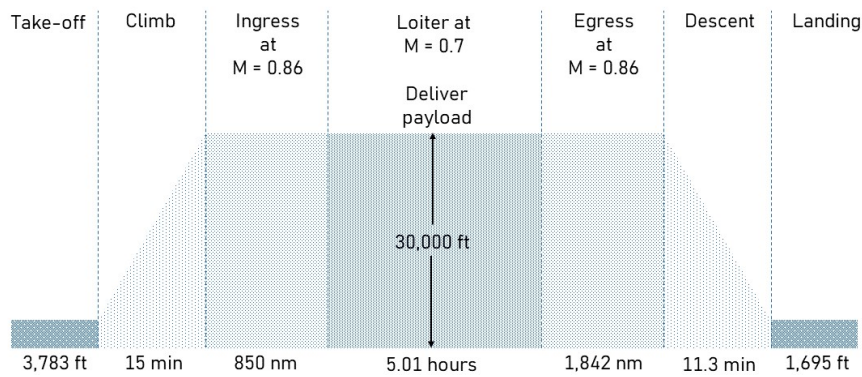
Figure 2.1: Flight plan of the main mission.

ments but not objectives), all the objective requirements were obtained.

Table 2.1: Design mission requirements.

	Value
Ingress range [nm]	850
Ingress speed [Mach]	0.86
Loiter time [h]	5.01
Dash speed [Mach]	0.93
Egress range [nm]	1842 [T]
Egress speed [Mach]	0.86
Reserve time [min]	45
Take-off distance [ft]	2857 [T]
Landing distance [ft]	886
Replenish time [min]	1.32
Payload weight [lbs]	783.1
Number of payload	27 [T]
Certification	FAA CFR 14 Part 23

2.1. Communication system

Unmanned aircraft are controlled by a ground control station, which uses a direct data link for take-off and landing while the aircraft is within the station's line of sight [2]. However, when the aircraft is out of sight of the ground control station, a satellite link control system takes over. The aircraft uses GPS to communicate its whereabouts to the ground station, the aircraft is also able to send other data via the same satellite link. Satellite communication offers the advantage of providing coverage in remote or damaged areas and high-speed data transmissions [3]. The disadvantages are that it requires a clean light of sight and due to the distance there can be latency or delays when sending information. This could be significant for time-sensitive operations. The use of a satellite link control system en-

sures that in the event that all land-based communication facilities have been destroyed, a reliable form of communication and control is used. It is anticipated that the number of satellites will continue to increase in the coming years, which will lead to greater competition and cost reductions in satellite communication. This trend is supported by [4] which projects the satellite communication market size to expand at a CAGR of 10.5% to reach $91.02 billion in 2027.

2.2. Identifying Victims

To identify the people in a disaster zone, a long-range thermal camera system is an ideal solution as it provides the ability to search in all-weather conditions during the day and night. The two types of thermal cameras suited to this are a mid-wave infrared spectral band camera (MWIR) and a long-wave infrared spectral band camera (LWIR) [5]. The choice to use a MWIR camera was decided upon for the following reasons: they perform better in warmer climates, this is crucial as the target market analysis revealed that the target market is countries with warmer climates, less affected by humidity and thus are perfect to use near large bodies of water, more suited for very long-range target detection at 30,000 ft distance or more and the thermal contrast is greater thus easier to identify the victims.

Thus, the optical camera system selected is the STAR SAFIRE 380-HD [6]. This camera features a MediumWave Infrared (MWIR) thermal imager, HD colour and low-light camera. The MWIR thermal imager is used to identify humans while the HD colour and low-light cameras are used to get a clear image of the disaster zone in good and bad conditions. The optical system has an ultra-long-range imaging performance allowing for a large area to be scanned. The system can operate autonomously thus it can identify the victims faster and more reliably than a human operator. The optical camera will be installed in the nose to have an uninterrupted view of the world below it via a porthole on the nose.

2.3. Package for the victims

To determine the quantity of fresh water needed, the number of victims and their daily water requirements needed to be known. The average daily water intake for an adult male is 0.98 gallons and for an adult female, it is 0.71 gallons [7]. Thus, assuming that the victims are in groups of a maximum of two individuals each, the minimum number of water to be delivered would be 1.69 gallons to account for the fact that the victims could be males. The assumption is that the victims will be stranded for at least six additional hours thus the amount of water delivered will be able to last one day. In this case, visits to

the same victims will not be made on the same mission. Considering the fact that the victims will be victims of a natural disaster a basic first aid kit will also be delivered to the victims. This is because a first kit is essential to have in an emergency. After all, it contains the basic medical supplies that can be used to treat injuries or illnesses while waiting for help to arrive. A satellite communication radio along with a flare will also be delivered to the victims. A flare is commonly used for signaling help in emergencies and thus in this case it will be used in conjunction with the radio so that it will allow the victims to communicate exactly where they are so that help can reach them as quickly as possible. Satellite radio allows for communication even when no cell towers are available thus it will allow for continuous updates with the operators if urgent medical care is needed.

The package is a rectangular box with dimensions of 9.84" x 5.88" x 7.92" and a volume of 458.24 cubic inches. A single package consists of two bottles of water, a first aid kit, a communication radio and a flare. The weight of each package is 14 lbs. The aircraft will carry 27 packages that will be stored in a special section in the fuselage.

Figure 2.2: Package to be dropped 2.2.

2.4. Delivery Method

A guided parachute system is selected as it is the most practical solution since it can deliver the package close to victims that may not be able to travel very far due to their injuries or the terrain. The package is equipped with a flare that is ignited when the main parachute is deployed to allow the victims to identify where the package has landed. The different precision aerial delivery systems by Airborne Systems were evaluated [8], i.e. the FC Mini, MicroFly 2, FireFly, 2K1T and FlyClops 2K parachute systems from Airborne Systems. The parachutes above were used as a reference to estimate the weight of a similar system to be able to carry the packages. Since the weight of the packages is significantly less than the minimum weight required by the Airborne Systems parachute. Therefore, an average of

the system weights and payload weights was taken and a linear relationship was found that could be used to approximate the weight of a similar system for the packages. The final weight of the guided parachute system for a single package was found to be 1.3 lbs. This is a safe approximation to ensure that if the packages are slightly overweight that the parachute system will still function as intended. As the guided parachute does not carry a fragile package, a perfect landing is not needed since the payload can withstand minor impacts. To facilitate the rescue crews, a tracker will be placed inside the parachute system which will allow the location of the victims to be pinpointed, the tracker can then be taken by the victims if they need to leave their current area.

2.5. Extraction mechanisms

Firstly, the packages will be dropped out of the cargo hold through trapdoors located on the bottom of the fuselage. The mechanism is responsible for the way in which the load leaves the aircraft. There are two main mechanisms currently in use for unmanned aerial vehicles. They are the auto extraction and gravity extraction system. The auto-extraction system uses an extraction parachute to pull the payload out of the aircraft before the main parachutes are deployed to slow the descent. The gravity extraction system uses the attitude of the aircraft to cause the payload to roll out of the aircraft before the main parachutes are deployed to slow the descent. Since the packages are not being delivered all at once, a mechanism is needed that could allow the packages to be delivered one by one. A novel approach is using a conveyor belt system similar to the ones found on a manufacturing line to allow the packages to be released out of the aircraft one by one.

2.6. Pressurization and temperature controls

The cargo bay of the aircraft will be pressurized. This is to ensure that the water bottles and first aid kits in the packages do not become damaged [9]. Thus, a pressurization system is needed to ensure the optimal pressure and temperature. The system is composed of 3 main components: the pressure hull, compressor, and outflow valve [10]. The pressure hull is an airtight section of the aircraft where air can not escape. For this aircraft, the pressure hull is the cargo bay where the pacakges will be stored. For jet engines, the compressor and a combination of valves allow high-pressure air from the engine to be directed into the pressure hull, thus allowing the pressure and temperature to be controlled. An outflow valve is installed to prevent the hull from being over-pressurized.

3 Methodology

The steps followed to determine the conceptual design of the Radar aircraft is presented in Figure 3.1. The study involves conducting numerical, empirical, and analytical investigations using MATLAB software, Siemens NX, and referencing several sources cited at the end of the document. At the very beginning, research work is performed to have a strong overview of existing aircraft for similar mission requirements. The main configuration characteristics can be chosen. This study then helps to make a first guess of the Maximum Take-Off Weight (MTOW), wing area, and power needs. From these first guesses, more detailed aircraft characteristics can be computed for each aircraft subsystem. Depending on the stability and performance, the process is repeated iteratively. After determining the geometry, a more detailed analysis is carried out to delve deeper into the aerodynamics and, more importantly, the performance aspects. The final step is to assess, with a trade-off study, that the designed aircraft maximizes performance and requirements.
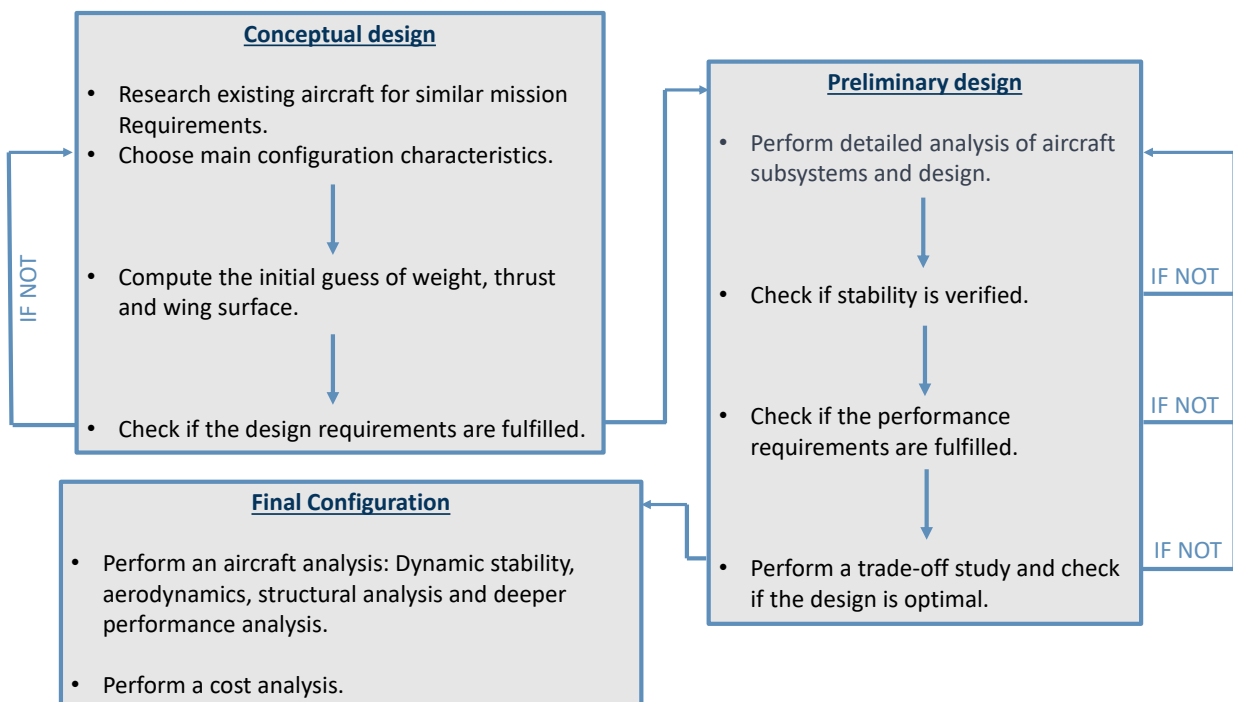
Figure 3.1: Flowchart of the design methodology.

4

Configuration

4.1. Existing configurations

The design of the aircraft was based on a review of existing aircraft designs which have a similar set of requirements. At the time of writing, no production-ready UAV existed that could meet the main requirements set out by the AIAA. Thus, a different class of aircraft were investigated. By comparing the existing configurations, a better approximation of the different parameters such as the maximum take-off weight, length and wing span could be made.

Long-range private jets were considered as they are known to have extremely long ranges and high speeds while not being as big as normal passenger commercial aircraft. The three private jets considered are shown in figure 4.1

Figure 4.1: Existing private jets: Gulfstream G650 (top left) [11], Dassault Aviation Falcon 8X (top right) [12] and Bombardier Global 7500 (middle bottom) [13].

The specifications of private jets are shown in table 4.1. From this it can be seen that the Gulfstream G650 and Dassault Aviation Falcon 8X can reach the required range, speed and landing distance however, all the private jets fail to meet the requirements for the take-off distance. Therefore, it will be important to consider a design that results in a shorter take-off distance. Nevertheless, these values served as a reference when approximating the initial main parameters of the aircraft.

Table 4.1: Specifications of existing private jets.

	G650	Falcon 8X	Global 7500
Max take-off weight (lbs)	53991	73000	106250
Length (ft)	98	79	111
Wingspan (ft)	98	86	104
Max speed (mach)	0.92	0.9	0.71
Range (nm)	7000	6450	7700
Take-off distance (ft)	5858	6000	5800
Landing distance (ft)	3182	2150	2850

4.2. Design choices and first estimations

4.2.1. First weight estimation

The first step is to estimate the maximum take-off weight W_0. All mission segment weight fractions are tabulated in the table 4.2. For warmup and take-off, climb, and landing weight factors, historical values are given in the P. D. Raymer's book [14].

Table 4.2: Mission-segment weight fractions.

Weight fractions	Value
Warmup and take-off W_1/W_0	0.97
Climb W_2/W_1	0.985
Ingress W_3/W_2	0.9019
Loiter W_4/W_3	0.7919
Egress W_5/W_4	0.7842
Loiter/Reserve W_6/W_5	0.9656
Landing W_7/W_6	0.9950

Weight factors for cruise and loiter phases are computed assuming the specific fuel for low-bypass turbofan. The lift-to-drag ratio is evaluated considering conventional wings. The mission fuel fraction is estimated to $(1 - W_7/W_0)$, with

$$\frac{W_7}{W_0} = \frac{W_1}{W_0}\frac{W_2}{W_1}\frac{W_3}{W_2}\frac{W_4}{W_3}\frac{W_5}{W_4}\frac{W_6}{W_5}\frac{W_7}{W_6}. \tag{4.1}$$

The reference considers a 6% allowance for reserve and trapped fuel, the total fuel fraction becomes $W_f/W_0 = 1.06(1 - W_7/W_0)$. The take-off weight estimation is computed as follows, considering no crew:

$$W_0 = \frac{W_\mathsf{p}}{1 - W_f/W_0 - W_e/W_0}. \tag{4.2}$$

The empty weight fraction W_e/W_0 is computed assuming a *UAV - TacRecce & UCAV*:

$$\frac{W_e}{W_0} = AW_0^C K_{vs}. \tag{4.3}$$

An iteration loop is performed for the two last equations to find $W_0 = 5513$ lbf.

4.2.2. First gross wing area and drag estimations

The aim is to create a wing that can operate efficiently at both ingress and egress speeds, as well as during loitering, since the time spent at each of these speeds is similar. By referring to the performance data presented in Table 2.1, it is possible to calculate the duration of time spent at each speed. Specifically, the loitering phase is expected to last for five hours, while the combined duration of the ingress and egress phases is expected to last for five hours and 18 minutes.

According to E. Torenbeek [15], for a high subsonic jet aircraft C_{D_0} and Oswald span efficiency factor e can take values 0.019 and 0.85, respectively. Derivating the lift-to-drag ratio, obtained assuming parabolic drag, it is possible to obtain the optimal C_L for a given aspect ratio. The latter is set to 10, explained later in section 5.1, and the corresponding optimal C_L is 0.71. Using a steady flight assumption and a lift coefficient of 0.35 at Mach 0.86 and 30,000 ft, a first estimation of the wing's surface area can be obtained.

$$S = \frac{W_0}{0.5\rho V^2 C_L} = 48.4 \text{ ft}^2. \tag{4.4}$$

The lift coefficient of the airplane at loiter speed will be equal to 0.53. Operating an airplane at a lift coefficient too close to the optimal value can cause aerodynamic instability, leading to loss of control, stalling, and potential crashes. To ensure a safe and stable flight, it is crucial to operate the airplane at a C_L that is below the maximum value, considering both aerodynamic and structural factors. In addition to avoiding aerodynamic instability, operating at a safe C_L helps prevent excessive loads on the wings, which can cause structural damage and compromise safety. It is important to note that a wing that is too small may have difficulty generating enough lift for takeoff, which can affect the overall performance and safety of the airplane. The report will include a tradeoff analysis of the wing surface area 7.1.

Assuming parabolic drag, a preliminary estimate of the drag can be calculated, resulting in 372 lbf at Mach 0.86 and 246 lbf at Mach 0.7.

4.2.3. Aircraft type

Two configurations exist for aircraft that fly in the transonic region: tube and wing configuration and a blended wing body. The tube and wing was selected for several reasons:

- it is a simple design that is easy and cheap to manufacture, which is important for an aircraft that is expected to be attritable;

- blended wing body is the more aerodynamically efficient design but it is complicated and expensive to manufacture [14].

4.2.4. Wing

Three main wing placement options are available: low, mid and high-wing. The high wing was selected for several reasons:

- since the aircraft will not be carrying passengers, there will be no need to have an emergency landing on the sea. thus, there are no other advantages to a low-wing configuration;

- the cargo space is not reduced in size like it would be with a mid-wing configuration[14];

- a shorter landing gear can be installed, thus reducing weight therefore floor of the aircraft can be closer to the ground which makes it easier to load and unload the payload into the aircraft;

- the landing gear can be stored in the fuselage allowing a larger fuel tank to be installed in the wings thus increasing the range of the aircraft;

- this configuration has increased roll stability;

- performs better in short take-off and landing as larger flaps can be installed and the wing tips are less likely to strike the ground.

Moreover, a high aspect ratio is important because it reduces drag and improves the lift-to-drag ratio, allowing for greater fuel efficiency and longer flight times.

4.2.5. Engine

To fly in the transonic region, a powerful engine is needed. The three most common types of engines found in this region are the turboprop, turbojet and turbofan. A single turbofan engine mounted in the fuselage was selected for the following reasons:

- turbofan engines are more efficient at producing thrust for a given amount of fuel and can reach higher speeds when compared to a turboprop engine;

- space is not of concern thus the space savings of a turbojet were not needed;

- a single engine is chosen for simplicity and low-cost reasons while still allowing the aircraft to reach the desired speeds;

- mounting the engine is the fuselage reduces the drag on the aircraft thus allowing it to fly faster and further [14].

4.2.6. Landing gear

Three types of landing gear configurations were considered, the tricycle, quadricycle and taildragger. The tricycle configuration was selected for several reasons:

- it is more directionally stable due to the centre of gravity being located between the front and rear wheels thus preventing ground looping [14];

- allows the aircraft to land with large crab angles;

- allows the aircraft to have a flat floor which increases the cargo space.

4.2.7. Empennage

Three possible tail configurations were considered: conventional, T-tail and V-tail. The conventional tail was selected for several reasons:

- the design is simple and easy to manufacture [14];

- weights less than the other configurations;

- offers an excellent level of control and stability due to its predictable response to flight inputs;

- less susceptible to turbulence and easier to control in an emergency;

- the most reliable configuration that exists.

4.2.8. CAD model

Figure 4.2: Front view of the aircraft.
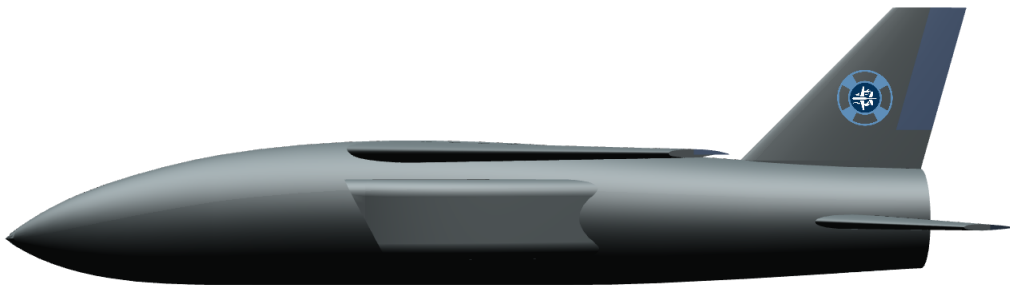
Figure 4.3: Side view of the aircraft.
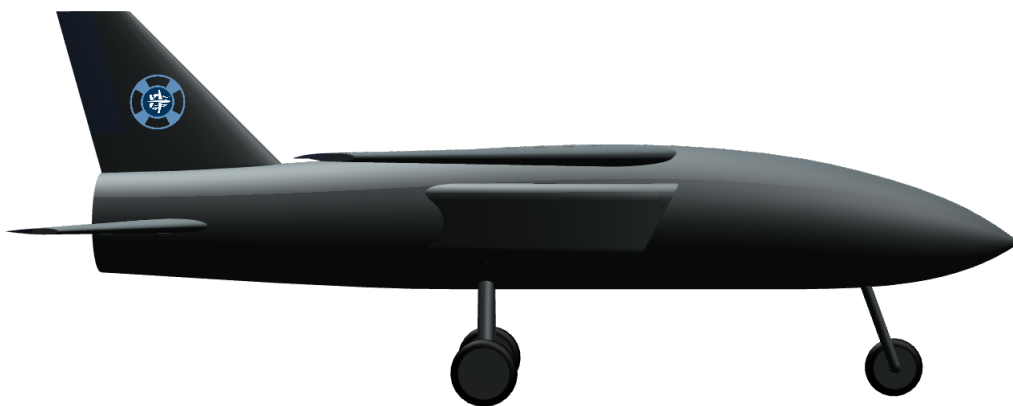
Figure 4.4: Side view of the aircraft with landing gears.
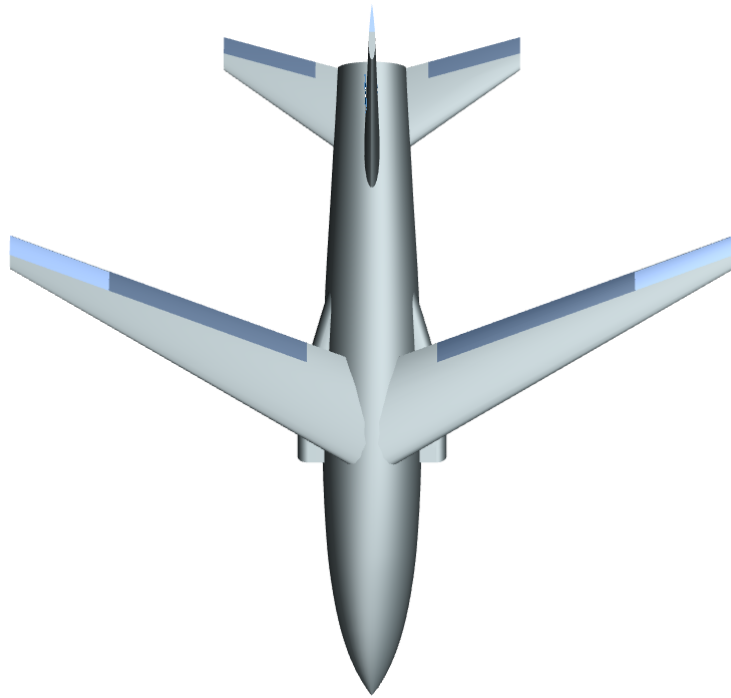
Figure 4.5: Top view of the aircraft.
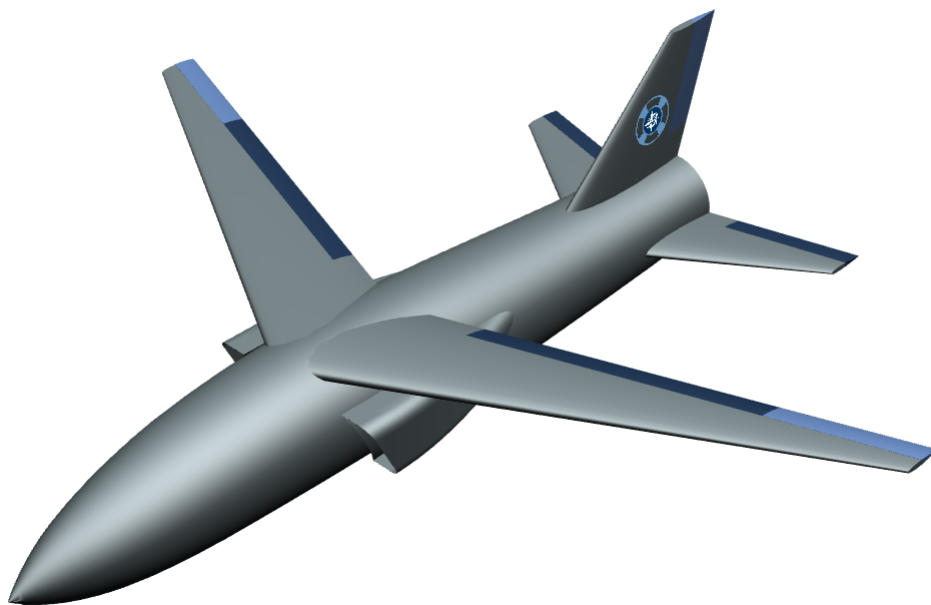
Figure 4.6: 3D view of the aircraft.

5 Component design

5.1. Wing design

The wing is a vital component of an aircraft and has a significant impact on its overall performance. This section outlines the design process for the wing, which involves determining basic and geometric parameters based on design requirements. The geometric planform of the wing is then established, followed by the design of high-lift devices that meet take-off and landing requirements. Control surfaces are subsequently designed.

The wing design is an iterative process, with various parameters being redesigned until the desired lift, drag, and pitching moment are achieved. The methodology described by Raymer in [14] is used to determine geometric parameters, while the high-lift devices are designed using the methodology presented by DATCOM 1978. The control surfaces are designed following the methodology described by Gudmunsson in [16].

Initial choices

In order to safely deliver packages over disaster areas, an aircraft design has been chosen that takes into consideration the potential challenges of these flight conditions. The design includes a high-wing configuration to maximize stability and a nose opening in the fuselage for convenient package storage. The dihedral angle has been maintained at 0 for ease of manufacturing, with negligible impact on maneuverability. However, given the aircraft's intended speed, which will be greater than 0.7 Mach, a wing sweep angle is necessary. The selection of the sweep angle will depend on the airfoil chosen and its critical Mach number.

Geometric planform

The geometric planform of the wing is designed by first determining the reference surface area, which has been estimated at 48.42 ft^2 during the preliminary design phase. This value was chosen based on the aircraft's intended lift coefficient of 0.35, which allows for optimal performance during cruise while also meeting the required takeoff and landing distances.

An aspect ratio of 10 has been selected for the wing, as it improves aerodynamic performance and

reduces drag during different mission phases, resulting in higher efficiency and longer range. However, to avoid structural issues, the aspect ratio has been limited to 10, which is within the range reported in literature for transport jets operating at similar speeds.

The taper ratio, which determines the lift distribution along the span, is also a critical parameter. A taper ratio of 0.3 has been chosen to achieve a lift distribution close to the ideal elliptical one, striking a balance between induced drag reduction and structural considerations. This value aligns with those commonly used in jet transport with similar performance expectations.

To prevent tip stall and improve lift distribution, a twist angle of -2° has been applied to the wing. This value falls within the range of 0 to -5° reported in literature and represents a reasonable compromise between competing design considerations.

The different geometric parameters of the wing are summarised in Table 5.1.

Table 5.1: Geometric parameters of the wing.

Parameters	Dimensions
Surface area [ft^2]	48.42
Aspect ratio [–]	10
Taper ratio λ[-]	0.3
Twist angle ϵ[°]	-2
Dihedral angle Γ[°]	0

5.1.1. Airfoil selection

The airfoil plays a crucial role in determining the optimal pressure distribution on the wing's upper and lower surfaces, creating lift with the lowest possible aerodynamic cost.

Since the aircraft has been designed and optimized for the cruise phase, the cruise conditions will be taken in order to choose the appropriate airfoil. During the cruise, the aircraft is flying at a speed of 0.86 Mach at an altitude of 30,000 ft, which falls within transonic conditions. Extensive research has shown that the supercritical airfoil family is the most appropriate choice for this flight condition, as it is specifically designed to minimize the side effects associated with shock formation.

The wing of the aircraft has been designed to have a specific lift coefficient of 0.35 during the cruise phase, which requires the supercritical airfoil to have a similar design lift coefficient to achieve effi-

ciency. The nomenclature for supercritical airfoils simplifies the selection process, with the first two digits following the dash indicating the design lift coefficient multiplied by 10. The airfoils contained in the supercritical family having a lift design coefficient the closest to 0.35 are the airfoils designated as NASA SC(2)-04XX where the XX corresponds to the maximum thickness of the airfoil expressed in percentage. In order to select the most suitable airfoil a comparison between the existing airfoils having a lift coefficient of 0.4 has been purchased. The comparison has been done by considering a Mach number of 0.7 because these airfoils have a critical Mach number which is lower than the cruise Mach number making it impossible to compare them under cruise conditions. However, the comparison made at a Mach number of 0.7 is reasonable since a sweep angle will be given to the wing reducing the Mach number seen by the airfoil. The comparison of the aerodynamic coefficient is represented in the Table 5.2.

Table 5.2: Comparison of the aerodynamic characteristics of different airfoils at Mach 0.7.

Airfoil	c_{l_α} [1/rad]	c_{m_0} [-]	α_{l0} [°]	c_{l_0} [-]	$(c_l/c_d)_{max}$ [-]	M_{crit} [-]
NASA SC(2)-0414	10.02	-0.115	-2.5	0.44	114	0.76
NASA SC(2)-0412	9.66	-0.103	-2.2	0.39	115	0.78
NASA SC(2)-0410	9.21	-0.0926	-2	0.34	94	0.8

In order to design an aircraft with optimal performance in cruise, certain criteria will be given a higher importance. The lift coefficient derivative,c_{l_α}, the lift coefficient at zero angle of attack,α_{l0}, and the lift to drag ratio,$(c_l/c_d)_{max}$ are among the key factors to be evaluated. The lift coefficient derivative represents the rate of change in lift generated by the airfoil in response to changes in the angle of attack. The airfoil with the highest lift coefficient derivative is preferred since it will produce more lift for a given change in angle of attack. Another important characteristic is the lift coefficient at zero angle of attack, which indicates the efficiency of the airfoil in generating lift while minimizing drag. A high lift coefficient at zero angle of attack is therefore desirable. Additionally, the lift to drag ratio is an important factor to consider as it indicates the overall efficiency of the airfoil in generating lift while minimizing drag.

After evaluating these aerodynamic characteristics, it was determined that the NASA SC(2)-0414 airfoil is the best option among the airfoils considered for the design of the aircraft, as it exhibits superior performance in terms of the lift coefficient derivative, lift coefficient at zero angle of attack, and have a lift to drag ratio similar to the best value.

However, the critical Mach number of this airfoil is lower than the actual Mach number in cruise. To

address this issue, a sweep angle of 27.6 degrees at the quarter chord was chosen to reduce the Mach number along the chord and bring it within the range suitable for the selected airfoil. With this sweep angle, the Mach number seen by the airfoil is reduced to 0.745, allowing for proper usage of the airfoil.

With all the geometric parameters being defined, it is now possible to represent the geometric planform of the wing (see Figure 5.1).
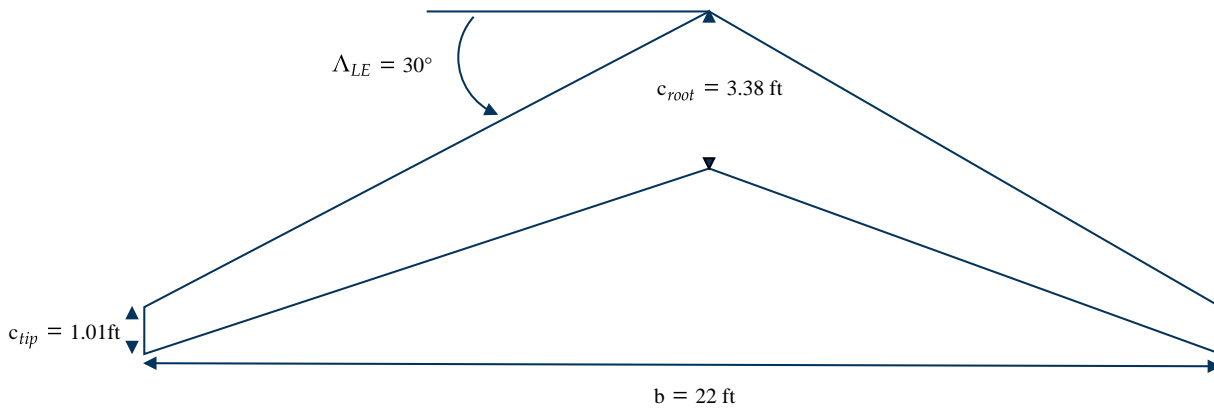
Figure 5.1: Representation of the geometric planform of the wing.

5.1.2. Control surfaces

High-lift devices

To enable proper landing and takeoff of the aircraft, the use of high-lift devices is necessary since the maximum lift coefficient provided by the wing alone is insufficient. Following the estimation described by DATCOM 1978, the high-lift devices have been designed to meet the takeoff and landing distance requirements. Single-slotted flaps were selected to avoid adding excessive complexity and cost to the wing, as slats or double-slotted flaps would do. Moreover, the structure of the wing might not support the double-slotted flaps. The geometry of the flaps is summarized in Table 5.3.

Table 5.3: Geometric parameters of the flaps.

Parameters	Dimensions
Flap start [$\%_{b/2}$]	12
Flap end [$\%_{b/2}$]	70
Flap chord c_f/c [$\%_{chord}$]	25

Using the DATCOM 1978 estimation based on the geometry of the flaps, the incremental 3D lift due to the deflection of the flaps has been computed. A lift increment of 0.8057 was obtained during landing when the flaps are deflected at 45 degrees, and a lift increment of 0.4512 was obtained during takeoff when the flaps are deflected at 20 degrees. The angle of deflection at takeoff was determined based on literature, which recommended a range of deflection between 10 and 20 degrees. We opted for the maximum deflection to achieve better performance during takeoff. By computing the maximum 3D lift coefficient of the wing, the maximum lift coefficient with the single-slotted deflected can be computed. The maximum 3D lift coefficient is computed based on the following formula from [15] taking into account the fact that the wing is tapered:

$$C_{Lmax} = cos\Lambda_{1/4} \cdot 0.95 \cdot \frac{(c_{lmax})_{root} + (c_{lmax})_{tip}}{2}. \tag{5.1}$$

Given the 2D maximum lift coefficient of the airfoil, the 3D maximum lift coefficient of the wing is equal to C_{Lmax}=1.8. Taking into account the 3D maximum lift coefficient of the wing, the 3D maximum lift coefficient in landing and takeoff can be computed by adding the lift increment of the flaps. These values are summarized in Table 5.4.

Table 5.4: Maximum lift coefficient of the wing at takeoff and landing.

Flight phase	C_{Lmax}
Takeoff (flaps deflected at 20°)	2.25
Landing (flaps deflected at 45°)	2.6

Ailerons

To achieve lateral control of an aircraft, ailerons are necessary. Ailerons are similar to plain flaps, except they are deflected differentially, causing one aileron to move up while the other moves down. These ailerons are located on the outboard portion of the left and right wings. The design process for ailerons involves determining the helix angle created by the wing when the aircraft rolls. Literature suggests that for subsonic aircraft, the helix angle should be above 0.07, while for supersonic aircraft, it should be above 0.09. For transonic aircraft, a reasonable helix angle would be around 0.08.

The initial sizing for the ailerons can be determined using the methodology proposed by Raymer [14]. Using this methodology, the dimensions of the ailerons can be fixed. Additionally, literature suggests that the maximum deflection angle for the ailerons should be δ_{max}^{up} = 20° and δ_{max}^{down} = 18° for the type of aircraft designed. These geometric parameters are summarized in Table 5.5.

Table 5.5: Geometric parameters of the ailerons.

Parameters	Dimensions
Aileron start [$\%_{b/2}$]	70
Aileron end [$\%_{b/2}$]	100
Aileron chord $c_f/c[\%_{chord}]$	25

The helix angle can be determined based on the previous information on the ailerons. In order to compute the helix angle, the roll authority, $C_{l\delta a}$, the roll damping derivative, C_{lp} and the likely aileron deflection, δ_a have to be computed. Based on the maximum deflection angle of the ailerons, the likely aileron delfection can be computed as:

$$\delta_a = 0.75 \cdot \frac{1}{2} \left(|\delta_{max}^{up}| + |\delta_{max}^{down}| \right).$$ (5.2)

The roll authority can be computed as:

$$C_{l\delta a} = \frac{C_{L\alpha}\tau(b_2^2 - b1^2)}{b^2},$$ (5.3)

where τ is the efficiency and is assumed equal to 0.45, b_1 and b_2 are respectively the start and end position of the ailerons measured from the center of the aircraft, b is the span of the wing and $C_{L\alpha}$ is the 3D lift coefficient derivative of the wing.

The roll damping derivative can be computed as:

$$C_{lp} = -\frac{C_{L\alpha} + C_{D0}}{6},$$ (5.4)

where C_{D0} is the drag produced by the wing and is assumed equal to 0.0016 according to the range provided by the literature [14] for a high subsonic aircraft.

Finally, the helix angle can be computed as:

$$Helix\ angle = \frac{-C_{l\delta a}}{C_{lp}} \cdot \delta_a.$$ (5.5)

As it can be seen, the helix angle is related to the 3D lift coefficient derivative of the wing. However, this derivative varies depending on the flight condition (loiter or cruise). So, the helix angle will be computed in the loiter phase and in the cruise phase and the values are summarized in the Table 6.16.

Table 5.6: Computation of the helix angle for different flight phases.

Parameters	Loiter ($Mach 0.7$)	Cruise ($Mach 0.86$)
Roll authority $C_{l\delta a}$ [1/rad]	0.3383	0.3218
Roll damping derivative C_{lp} [1/rad]	-0.9837	-0.935
Helix angle [rad]	0.0856	0.0856

The results presented in Table 5.6 shows that there is no difference in helix angle if the aircraft is in the cruise phase or loiter phase. Indeed, the helix angle is always equal to 0.0856. The design of the ailerons is validated since the helix angle is greater than 0.08 and lower than 0.09.

The geometric parameters of the ailerons and the high-lift devices being defined, it is possible to represent the control surfaces on the wing (see Figure 5.2).
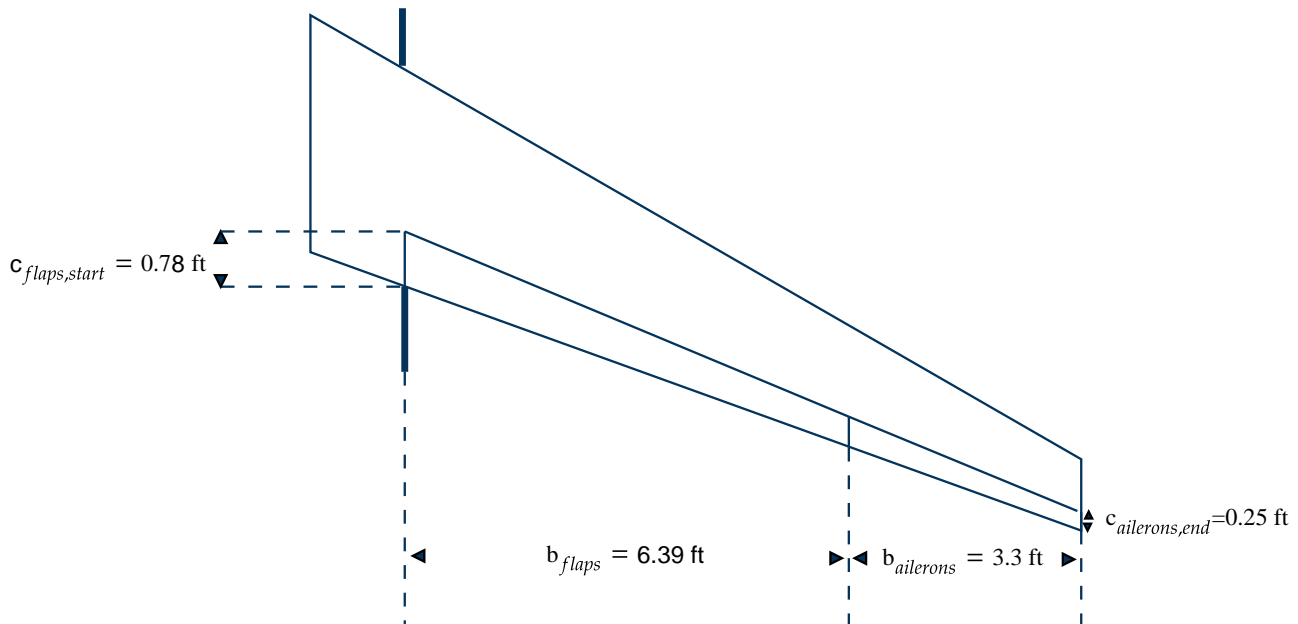
Figure 5.2: Representation of the control surfaces on the wing.

5.2. Tail, elevators and rudder

5.2.1. Tail arrangement

One of the main parts of an aircraft is the empennage which is usually composed of a vertical and horizontal tail. This component can produces a little fraction of the total lift required or generate a downlift (usually), but its main objective consists to provide trim, *i.e*, generating a force that balances the moment

produced by the aircraft. But there are two other important functions, the empennage must satisfy both stability and control in pitch and yaw, *i.e*, it must be sized in order to stabilize and provide enough maneuverability. This is achieved thanks to the control surfaces like rudders or elevators.

There are several types of empennages, but the conventional looks the most appropriate for the mission. This arrangement is the most used and is the best choice when developing a new design. It is composed of an horizontal surface generally placed in the middle of the rear fuselage and a vertical surface. On the other hand, as the same aircraft is used to transport and drop the payload, it is necessary to find a tail configuration that provides enough stability and control during the different phases of the flight. In addition, this type of tail has the lowest structural weight and cost, which are further advantages for the mission. Finally, a canard is not necessary in this case because the aircraft does not need to fly at high angles of attack, stability and control are achieved by using a classical empennage.

5.2.2. Design

Now that the tail configuration is chosen, the geometry of the vertical and horizontal tail must be determined. To do this, some typical values are used, *i.e*, AR in range 3-5 and taper ratio in range 0.2-0.4 for the horizontal tail. For the vertical tail an AR in range 0.6-2 and a taper ratio in range 0.2-0.4 [14]. The values used are shown in Tables 5.7 and 5.8.

Then, to obtain all the geometry, a historical approach is used which consists of using the tail volume coefficient method [14]. As the main goal of a tail is to counter the moments produced by the wing and provide a balanced aircraft, thus the tail size would be in some way related to the wing size. In the following expressions, the tail surfaces are given by a relation that takes into account the geometry of the wing and the tail arms.

$$S_{HT} = \frac{c_{HT}b_W S_W}{L_{HT}} \, , \tag{5.6}$$

$$S_{VT} = \frac{c_{VT}b_W S_W}{L_{VT}} \, , \tag{5.7}$$

Where c_{HT} and c_{VT} are the volume coefficients, which are typically in range 0.4-1 and 0.02-0.09 respectively. L_{HT} and L_{VT} the distance between the aerodynamic center of the wing and the aerodynamic center of the tail corresponding respectively to the vertical tail and horizontal tail. Finally, in the expres-

sions 5.6 and 5.7 the wing geometry is taken into account, *i.e*, the span, surface area and mean chord of the wing.

In addition, the vertical tail usually has a sweep angle in the range $[35\text{-}55°]$ and the horizontal tail approximately $5°$ more than the wing sweep angle [14]. Then, the geometry of the wing being known, the surfaces of the vertical and horizontal tail are determined. Finally, it can obtained the main geometrical parameters represented in Tables 5.7 and 5.8 or in Figure 5.3. AR, λ and volume coefficients are chosen in order to obtain a surface that verifies the equilibrium and that is close to what is used in the aeronautical industry.

Finally, the airfoil choice. The empennage airfoils are usually symmetric, the main requirements that will be achieved are a high lift coefficient and a large range of usable angles of attack. In addition, they are easier to manufacture and therefore inexpensive [14]. Thus, a NACA 0012 which is an usual airfoil is selected for both the horizontal and vertical tail.

Table 5.7: Horizontal tail parameters.

Parameters	Dimensions
AR [–]	4
λ [–]	0.4
S_{HT} [ft^2]	12.84
Elevator span b_E [ft]	2.87
Elevator chord C_E [ft]	0.56
Elevator surface S_E [ft^2]	2.50

Table 5.8: Vertical tail parameters.

Parameters	Dimensions
AR [–]	1.4
λ [–]	0.4
S_{VT} [ft^2]	9.1
Rudder height h_R [ft]	2.64
Rudder chord C_R [ft]	0.78
Rudder surface S_R [ft^2]	1.7213

In order to validate the geometry of the control and lifting surfaces, one needs to study the equilibrium of the aircraft.

At first, it can determined the angles of incidence of the wing and the horizontal tail with respect to the fuselage centerline. They are obtained considering a reference point of the flight. The latter corresponds to the weight of the aircraft at mid-flight, in other words, when the aircraft has consummed half of its fuel and dropped half of its payload. It yields, respectively for the wing and the tail : $i_w = 0.58°$ and $i_{HT} = -0.94°$. Then precise steps can be followed to obtain the angle of attack of the fuselage throughout the flight. Too high of an angle would mean that the equilibrium of the aircraft is not ensured.

- At first, it can be computed the lift coefficient of the aircraft at its current configuration : $C_L^* = \frac{W_{total}}{q \, S_W}$

where q $= 2.26$ psi is the dynamic pressure of the aircraft at mach 0.86 and at $30,000$ ft.

- Then, one can compute the lift coefficient distribution on the wing :

$$C_{\text{Lw}} = \frac{C_L^* - C_{m0} \frac{\bar{\bar{c}}}{L_{\text{HT}}}}{1 + (h - h_0) \frac{\bar{\bar{c}}}{L_{\text{HT}}}}$$

(5.8)

- Finally, the angle of attack of the fuselage at a given aircraft configuration can be therefore obtained : $\alpha_f = \frac{C_{\text{Lw}}}{C_{L_\alpha,\text{wing}}} + \alpha_{L_0 \text{ root}} - i_{\text{w}}$

Table 5.9: Evolution of the fuselage angle of attack during the aircraft flight.

	Ingress		Loiter		Egress	
	Start	End	Start	End	Start	End
α_f [°]	0.96	0.74	0.74	1.86	1.86	-0.33

The study of the equilibrium shows a huge influence of the position of the empennage, in particular the horizontal tail. For values of $L_{\text{HT}} = 9.1$ ft and $L_{\text{VT}} = 8.2$ ft, the angle of attack of the tail, $\alpha_T = \alpha_f + i_{HT}$, varies between 0.92 [°] and -1.27 [°]. In the meantime, the angle of attack of the wing, $\alpha_w = \alpha_f + i_w$, varies between 0.25 [°] and 2.44 [°]. Those values allow state that the aircraft remains at equilibrium during flight.

5.2.3. Control surfaces

Elevator

The two main requirements that the elevator must to satisfy are the take-off rotation and the longitudinal trim requirement. For the sake of simplicity only the first requirement is studied, it can be considered the most important [17]. To size the elevator, the angle of attack effectiveness parameter τ_{E} must be computed. This parameter depends on the equilibrium equations of the aircraft just before the take-off rotation, the aircraft and the airfoil geometry. In others words this parameter quantifies the elevator chord to chord ratio $C_{\text{E}}/C_{\text{HT}}$ so that the aircraft can rotate with a maximum up-deflection of 25°. The value of τ_{E} is equal to 0.62 and thus $C_{\text{E}}/C_{\text{HT}} = 0.41$. The elevator chord to chord ratio is typically in range $[0.2 - 0.4]$ [17]. The span elevator to span ratio $b_{\text{E}}/b_{\text{HT}}$ is approximated by a guess value from [17], $b_{\text{E}}/b_{\text{HT}} = 0.8$, the maximum down-defection is fixed to 20° [17].

Rudder

The two main requirements that the rudder must to satisfy are cross-wind landing and the coordinated turn requirement. Specially, cross-wind landing is a technique used by pilots to land an aircraft when the wind is perpendicular to the runway. The rudder prevent the aircraft from exiting the runway. However, the sizing of the rudder is a more complex task because it depends on the dynamic stability, more specifically on the rudder derivatives. Thus, certain percentages of what is usually designed are used, rudders generally begin at the root and extend to the tip of the tail or to about 80-90% of the tail span. Then, rudders and elevators are typically about 25-50% of the tail chord [14]. In order to have enough maneuvrability, we choose 40%, and the maximum deflection equal to 30° [17].
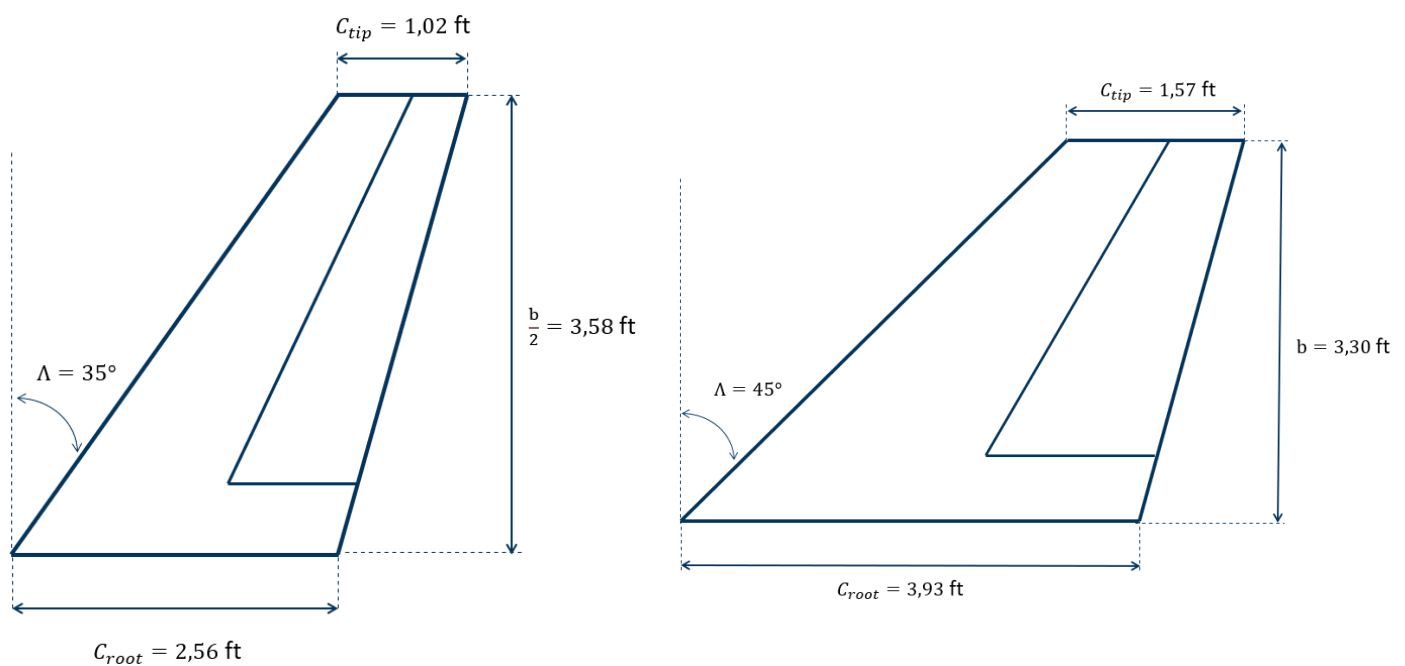
Figure 5.3: Empennage geometry: Horizontal tail & Elevator (left) , Vertical tail & Rudder (right).

5.3. Propulsion

This section is based on the drag corresponding to the final RADAR configuration. Further analysis is performed in the section 6.3.1 and provides drag coefficients for any point of the mission. The drag is simply obtained from the well-known formula $D = 1/2\rho V^2 S C_D$. The maximum drag acting on the RADAR, i.e. at the beginning of the mission, equals 330 and 394 lbf for, respectively, at flight's Mach number of 0.7 and 0.86.

5.3.1. Engine selection

The propulsion system is a very important aspect of aircraft design. First, the thrust from the propulsion system must balance the drag when the aircraft is cruising. And second, the thrust from the propulsion system must exceed the drag for the aircraft to accelerate.

The RADAR aircraft is designed to fly at transonic speeds (Mach 0.7 for loiter phase and Mach 0.86 for the cruise). Turbofans have the best efficiency at these speeds ($0.7 < M < 1$), according to Figure 5.4. Electric propulsion was also an option. The battery weight is proportional to energy content, but this weight does not reduce during the flight. Therefore battery-powered aircraft can only be considered for very small ranges (with the current state of the art). Hybrid turbofans could be a good compromise (higher efficiency and lower CO_2 emissions) but won't be available for 2028.
The aircraft's range and speed requirements were deemed suitable for jet and military aircraft that use turbofans. The decision to use either high or low-bypass turbofans will depend on efficiency goals. As the RADAR aircraft is small and doesn't have high drag, low-bypass turbofans are a viable option.
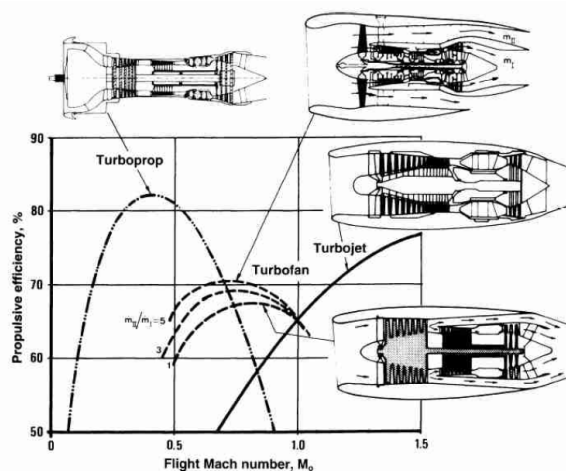
Figure 5.4: Different engine types comparison. The depicted diagram originates from Koen Hillewaert's course on propulsion [18].

Using multiple engines in an aircraft can enhance its thrust and safety compared to a single-engine setup, which can be troublesome if the engine fails. However, in the case of unmanned planes, opting for a single engine is a simpler and more cost-effective solution, since safety is not as critical without any pilots or passengers on board. Additionally, the aerodynamic drag to be compensated for is relatively low. The single-engine is placed at the rear of the fuselage. As the aircraft could be lost after 50 sorties with only Search and ID operations, the cost of the aircraft should be minimized and a single

engine has been chosen.

Two positions are plausible for the engine position at the rear of the aircraft: above or inside the fuselage. Since the aircraft does not carry any passengers, the engine's placement inside the fuselage is a viable option, as space within the fuselage is not a critical consideration. Moreover, fuel routing could be implemented more easily. If the engine were to be placed on top of the fuselage, the tail design would need to be altered. To retain the conventional tails, the single-engine is located within the fuselage, at the rear. The air intakes are discussed in section 5.3.2.

The primary objective is to identify an engine that can counteract drag at specified altitude and speed conditions, while also possessing a thrust level that is suitable for the engine's intended operational range. Any additional thrust should be reserved for takeoff/landing on limited runways, maneuvers, and achieving a dash speed of 0.9 if feasible. As the target speed for the aircraft design is Mach 0.86, with sufficient thrust reserve to enable optimal operation, i.e. approximately 80% of maximum thrust, it is highly likely that the maximum speed of 0.9 can be attained. The detailed calculation for this is presented in the performance analysis, as outlined in Section 6.5.4. As the wing's surface is quite small, a powerful engine will be required to take off.

In open-source databases, engines thrust and specific fuel consumption is only provided at static sea level. It is essential to convert the latter in flight conditions. Moreover, there is a difference between uninstalled and installed thrust. According to Raymer [14], the installed thrust is typically 4 to 8% lower than the uninstalled one. The uninstalled thrust measurements are done by putting the engine on a test bench, not inside an aircraft. Engine manufacturers communicate the uninstalled thrust.

The Thrust Specific Fuel Consumption can be computed as a function of the Mach number as developed in [19]:

$$\text{TSFC} = \text{TSFC}_0\sqrt{\theta}(1 + M)^n \tag{5.9}$$

where TSFC_0 is the static sea level TSFC, the load factor n is chosen in order to fit with experimental results, and θ is the ratio of temperature between the two atmospheric conditions.

Table 5.10 presents a selection of engines considered for the aircraft, with comparable specific fuel consumption values for loiter and cruise conditions due to similar bypass ratios. The table presents the most suitable engine version for the aircraft, as each engine has different versions with varying characteristics.

Table 5.10: Pre-selected engines characteristics. The information has been sourced from both the engine manufacturers' websites and reports issued by the European Union Aviation Safety Agency (EASA) [20]. Table values already incorporate the conversion of uninstalled to installed thrust, which accounts for an 8% increase.

	Static SL thrust [lbf]	T/W [-]	TSFC [lbs/h /lbf] ($M = 0.86$)	TSFC [lbs/h /lbf] ($M = 0.7$)	BPR [-]	Length [in]	Diameter [in]	Dry Mass [lbs]
GE Honda HF120	1926	4.13	N.A.	N.A.	2.9	59	26	466
P&W JT15D-5	2,728	4.31	0.77	0.71	3.3	63	27	633
P&W PW530A	2,656	4.31	0.61	0.57	3.7	60	32	616
P&W PW615F-A	1,342	4.34	N.A.	N.A.	2.8	49	30	309
P&W PW617F-E	1,740	4.59	N.A.	N.A.	2.7	54	30	379
Williams FJ33-5A	1,702	5.33	0.67	0.63	2.2	43	25	319
Williams FJ44-3AP	2,809	5.44	0.64	0.60	2.2	62	31	516

In [21], M. Bartel and T. Young suggest implementing an adjustment for engine thrust based on flight conditions. The correction takes into account altitude and Mach effects. Obtained results in flight conditions are presented in Table 5.11.

Table 5.11: Thrust correction values for various flight conditions based on [21], with the altitude assumed to be 30,000 ft.

	Thrust at $M = 0.7$ [lbf]	Thrust at $M = 0.86$ [lbf]	Thrust at $M = 0.9$ [lbf]
GE Honda HF120	486	464	461
P&W JT15D-5	670	637	633
P&W PW530A	639	607	603
P&W PW615F-A	341	326	324
P&W PW617F-E	483	424	459
Williams FJ33-5A	452	434	432
Williams FJ44-3AP	746	717	699

All engines selected produce thrust sufficient to compensate for the drag in each phase, except the P&W PW615F-A. For the selection, the engines may be classed into two groups of thrust. The higher thrust is provided by P&W PW530A and Williams FJ44-3AP. GE Honda HF120, P&W PW617F-E, and

Williams FJ33-5A produce a smaller thrust. It would be intriguing to explore the optimal engine in each thrust category and subsequently decide which thrust category holds greater preference.

The Williams FJ44-3AP is the best engine option due to its high thrust-to-weight ratio, compared to the other high-thrust engines. The P&W JT15D-5 has higher SFC and lower performance due to its older series.

Comparing the three remaining engines, the Williams FJ33-5A engine has a superior thrust-to-weight ratio compared to the other two engines, resulting in better acceleration, climb rate, and maneuverability. The FJ33-5A's compact size offers more design flexibility for smaller aircraft. The GE Honda HF120 and PW617F-E engines offer the advantage of operating closer to the optimal thrust setting during cruise conditions, but this comes at the cost of a lower thrust-to-weight ratio (T/W). However, using the Williams FJ33-5A, the takeoff performance is very close to the maximum takeoff distance threshold. Selecting another engine of the same thrust category is not viable because the takeoff distance would increase due to the decrease in the engine's thrust-to-weight ratio. The TSFC values for some engines are not readily available, including for the P&W PW600 series and GE Honda HF120, which is why a common SFC is used for comparing the three engines. The P&W PW617F-A and GE Honda HF120 have larger bypass ratios than the Williams FJ33-5A, so a better SFC is expected, but this cannot be confirmed without specific SFC values. It would be helpful to have these values to determine if the higher weight of the PW617F-A and HF120 engines is offset by their SFC.

The engine should ideally operate at around 80% of its maximum thrust during the cruise, and the second class of engines is best for near-optimal conditions. However, due to the small wing area of the aircraft, a more powerful engine may be necessary for takeoff requirements. Using plain flaps, lower thrust engines cannot achieve the required takeoff distance, so a trade-off between using single-slotted flaps or operating the engine at lower thrust levels must be made. Operating the engine at too low thrust can decrease fuel efficiency while optimizing the cruise phase is preferable. The Williams FJ33-5A is the best engine choice because it can provide the necessary thrust for takeoff while maintaining fuel efficiency, and it is also cost-effective.

In cruise conditions, the drag that the engine has to compensate for varies depending on the flight speed considered. Therefore, the efficiency of the engine related to the thrust setting also varies. Table

5.12 presents the drag and thrust setting over the mission.

Table 5.12: Evolution of the drag and thrust setting throughout the mission, i.e. at 30,000 ft. The drag values are obtained by following the methodology presented in section 6.3.1 and applying it to the specific configurations presented in the Table. The maximum operational thursts, depending on airspeed and altitude, for the Williams FJ33-5A are presented in Table 5.11.

	Ingress		Loiter		Egress	
	Start	End	Start	End	Start	End
Drag [lbf]	394	386	312	283	374	367
Thrust setting [%]	90.7	88.9	69.1	62.5	86.3	84.7

The engine thrust setting is a bit high for Mach 0.86 but allows maneuvers during the cruise. Loiter thrust setting decreases as drag reduces from Mach 0.86 to 0.7, improving turn performance for Search and Identification. The use of the engine in loiter phase is not optimal but acceptable. Reducing ingress/egress speeds can achieve more optimal conditions. A tradeoff is detailed in the section 7.

5.3.2. Air inlet design

The air inlet design of the RADAR drone was carefully considered, with two inlets placed on the sides of the fuselage instead of below it, in order to avoid disruptions when dropping packages. Placing the air intake in the nose was not considered optimal. The design requires an S-shaped duct to smooth out pressure gradients, and a straight line portion (in the fuselage body) to align the incoming flows. The capture-area ratio is set equal to 1 to power the engine at high angles of attack [14]. The air intake is cut off at a certain angle for this purpose as well. Moreover, the distance between the fuselage and the air inlet is an important aspect to avoid the dirty air of the boundary layer. This space must be studied further to evaluate if it reduces the aerodynamics of the aircraft. This has been inspired by the Alpha jet [22]. This type of inlet is called diverterless inlet.The design of the inlet is called diverterless.

5.3.3. Fuel volume

One could question the distribution of the total fuel weight inside the aircraft. It is the result of the process of considering the volume available inside the wing, which is filled with fuel, then the remaining mass of fuel is stored inside the fuselage. The computation of this volume takes into account the

geometry of the wing and writes as :

$$V_{fuel} = 0.54 \frac{S^2}{b} \left(\frac{t}{c}\right)_{root} \frac{1 + \lambda \sqrt{\tau} + \lambda^2 \tau}{(1 + \lambda)^2} \quad , \quad \text{with} \quad \tau = \frac{\left(\frac{t}{c}\right)_{tip}}{\left(\frac{t}{c}\right)_{root}} \quad\quad (5.10)$$

As $V_{fuel} = 41$ US Gallons and the density of kerosene is obtained trough documentation $\rho_{kerosene} = 51.2$ lbs $\cdot$ ft^{-3} [23], it enables to compute the total mass of fuel available in the wing and, by extension, the volume inside the fuselage, i.e. 312 US Gallons.

To estimate the mass of fuel required, the Breguet equation was used, taking into account the desired range and endurance objectives, as well as the initial weight estimate needed to obtain the lift-to-drag ratio. The specific fuel consumption of the Williams FJ33-5A engine is also considered in the calculation.

5.4. Fuselage

5.4.1. Fuselage geometry

The main purpose of the fuselage is to contain the components necessary for the aircraft and the mission, otherwise, it would not exist. Specifically, the fuselage must be able to hold the engine and air ducts, fuel, hydraulics, avionics, and electronics, the landing gear and retraction system, the payload and release system, and finally the batteries and the optical system that will detect the victims. Since the weight and volume of these elements can be calculated from [14], the total space required is determined:

$$\text{V}_{components} = 96.05 \, \text{ft}^3, \quad\quad (5.11)$$

To begin, given the operating speed ($\approx$ Mach 0.8) it is important to design a streamlined fuselage. This will aim to reduce drag. The fuselage is divided into three parts: the nose, the body, and the rear.

Firstly, we opted for the power series shape for the nose of the fuselage (Eq. 5.12).

$$y = \text{R} \left(\frac{x}{\text{L}_\text{N}}\right)^n \text{ with } n = 1/2, \qu\quad (5.12)$$

where R is the radius at the end of the nose and L_N is the length of the nose. This choice was motivated

by the fact that this type of design allows us to maximize the flight performance in the transonic region [24]. However, this nose shape has been a bit distorted to fit the fuselage body. The length is imposed, $L_N = 4.59$ ft, which is typically based on existing aircraft or in the range 3-5 ft from [14]. As it is usually done, this space will be dedicated to containing the optical system, the nose landing gear retraction system, and some avionics and electronics.

Then, the body of the fuselage contains most of the components. To fit the nose and the rear of the fuselage, and to have enough space, the body has a variable diameter of 2.64 ft and a length of 11.51 ft.

Since there is only one engine, it is placed at the back of the fuselage. The length and the diameter of the engine are 3.58 ft and 2.09 ft, respectively. In addition, the tail is slightly angled to prevent it from hitting the ground during takeoff, which will be discussed in more detail in the next section.

Finally, the Figure 5.5 shows a fuselage section with an overall length of 19.69 ft and a volume of 106.61 ft^3, 10% extra space is provided to prevent all components from being too tightly packed and thus allow for maintenance of the aircraft, but also to take into account the space occupied by the structure (frames, spars). Note that the section of the body has been approached by an equivalent constant diameter.
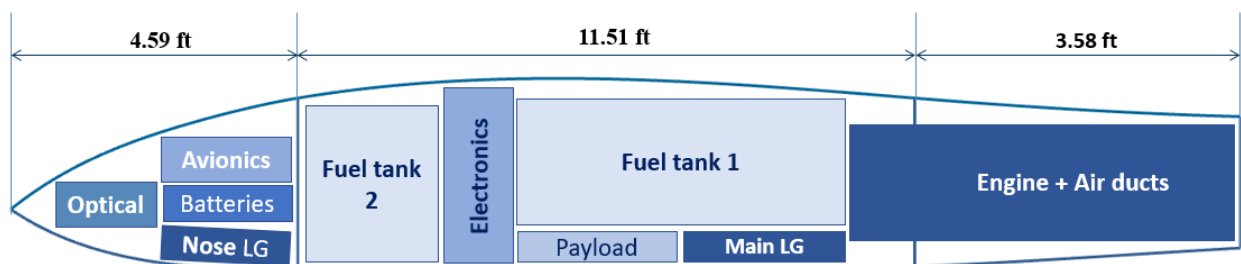
Figure 5.5: Fuselage section and components.

5.5. Landing gear design and position

It was decided to opt for a tricycle landing gear. This arrangement is the most commonly used today because it provides better ground stability and directional control [14] which can reduce the risk of ground accidents. This landing gear configuration is composed of two main wheels aftward of the c.g. and an

auxiliary wheel forward of the c.g.

The size of the main landing gears is computed by using the following formula from [14], which can gives both the diameter and the width:

$$(\text{diameter, width}) = A \, W_W^B \, ,$$

where A and B are two coefficients that depend on the type of aircraft and W_W the weight on the wheel. For the diameter, A and B are equal to 5.1 and 0.302 respectively. For the width 0.36 and 0.467 respectively.

Then, assuming that the main tires carry about 90% and the nose tire 80% of the aircraft weight. The nose tire is about 80% of the size of the main tires (acceptable assumptions for early conceptual design) [14]. In addition, only one nose-wheel (as it is commonly done for light aircraft and a few fighters) has been chosen. The dimensions of the landing gear are shown in Table 5.13.

Table 5.13: Parameters of the landing gears.

Wheel	Nose	Main
Diameter [in]	13.40	16.75
Width [in]	3.01	3.7680

There are several important criteria to consider when using this type of configuration. In particular, two ranges of angles must be respected to ensure that the tail does not hit the ground on landing and to measure the aircraft's tendency to overturn when taxied around a sharp corner. These angles are called respectively: the *tipback* angle and the *overturn* angle, in Table 5.14. As a reminder, the tipback angle is the angle at which the aircraft can turn without touching the ground on takeoff and the overturn angle is the angle between the main landing gear. It is recommended that the first be greater than $15°$ and the second be less than $64°$ [14]. Another condition is required in order to prevent the wing tip from touching down while manoeuvring. Indeed, it has been verified that the wing tip clearance is above 6" when the aircraft rolled $5°$. This condition was easily verified based on the aircraft high wing configuration.

Table 5.14: Tipback and overturn angles.

Tipback	Overturn
$16.07°$	$45°$

To ensure that the nose gear is not carrying too much or too little of the aircraft weight, $\frac{M_a}{B}$ should be greater than 0.05, and the ratio $\frac{M_f}{B}$ should be less than 0.20 (0.08 and 0.15 preferred), from [14]. Where B is the distance between the nose and the main wheels. M_a and M_B are respectively the distance between the aft CG and the main gear position and the distance between the fdw CG and the main gear position. The first ratio is equal to 0.13 and the second to 0.14, the position of the landing gears is indicated in Table 5.15 and in the Figure 5.5.

Table 5.15: Position of the landing gear from the aircraft nose.

	Nose	Main
Position [ft]	2.95	11.41

Finally, concerning the landing gear in the retracted position, the choice was to retract the gear into the fuselage. This choice was motivated by the fact that most high-wing aircraft use this configuration and can significantly reduce the drag during the flight of the aircraft.

5.6. Trapdoor

To design a hatch to safely drop packages from an aircraft at $30,000$ ft and Mach 0.86, several precautions must be taken. Firstly, the hatch must be resistant to aerodynamic forces, which means choosing the right material. Then, having a reliable release system to prevent accidental opening so as not to lose payload, minimizing the effects of air currents that could increase drag, and considering the impact of the release on the aircraft's stability. Finally, to ensure the safety and reliability of the hatch design, additional study and testing is required. The RADAR hatch starts at 50% of the fuselage length and is approximately the same size as the package to be dropped, *i.e*, $0.82 \times 0.49 \times 0.66$ [ft^3] (see Figure 2.2)

5.7. Material selection

The selection of appropriate materials is a critical aspect to consider when designing an aircraft as it can significantly impact the overall performance and safety of the aircraft. In the following paragraph,

we will delve into the various factors that must be considered when selecting materials for each aircraft component. [25]

First, The material selection for the wing is critical to guarantee the aircraft's performance and safety. Various factors such as strength, weight, and cost must be considered when choosing wing materials to achieve this goal. Composite materials are one of the most common materials used for the wings of UAV fighters. Composite materials can be made from a variety of materials. Carbon fiber is the most popular choice due to its high strength and low weight. In addition to composite materials, metal alloys such as aluminum and titanium can also be used for UAV fighter wings. Aluminum is lightweight and relatively inexpensive, but not as strong as some other materials. Titanium, on the other hand, is stronger and more durable than aluminum, but also more expensive.

The properties are listed in Table 5.16. We chose aluminum because it is cost-effective, despite its weight and strength being less favorable compared to the other two materials, they are still within an acceptable range.

Table 5.16: Properties of the material candidates for the wings

Material	Tensile strength [ksi]	Density [lb/in^3]	Cost [$/lb]
CFRP	200-500	0.055-0.065	10-30
Aluminum Alloys	40-90	0.1-0.11	0.75-2.5
Titanium	100-200	0.16	15-50

When selecting a material for the fuselage, the same factors as for the wings are taken into consideration. In addition, the fuselage may require materials that can absorb impact to protect the payload or crew compartment. However, in the case of a UAV designed for carrying water and radio equipment, impact resistance may not be as essential. Therefore, we have chosen aluminum for the fuselage due to its favorable cost and acceptable weight and strength characteristics.

Again, the same factors are taken into account for the tail. However, it requires materials that can withstand high stresses, as it is responsible for providing stability and control during flight. Materials such as titanium or steel alloys, which have high strength and stiffness, are commonly used for tail components. Other materials such as composites and aluminum alloys can also be used for tail components. These materials can offer advantages in terms of weight reduction and ease of manufacturing. The main properties of these materials are listed in Table 5.17. We selected Carbon Fiber Reinforced Polymer for the tails due to its favorable strength-to-weight ratio.

Table 5.17: Properties of the material candidates for the tails

Material	Tensile strength [ksi]	Stiffness [Msi]	Density [lb/in^3]	Cost [$/lb]
CFRP	200-500	8.5-10.5	0.055-0.065	10-30
Aluminum Alloys	40-90	10-11	0.1-0.11	0.75-2.5
Titanium	100-200	16-18	0.16	15-50
Steel	75-220	29-30	0.283-0.304	0.5-5

Finally, the landing gear is another crucial component of the aircraft that requires careful consideration when selecting materials. The materials used for the landing gear must be able to withstand high stresses and loads during takeoff, landing, and taxiing. The materials must also be durable and resistant to wear and tear to ensure the landing gear's longevity and reliability. Common materials used for landing gear include high-strength steel alloys, titanium alloys, and aluminum alloys. Based on the properties outlined in Table 5.18, we have selected high-strength steel for its favorable combination of high strength and low cost.

Table 5.18: Properties of the material candidates for the landing gears

Material	Tensile strength [ksi]	Stiffness [Msi]	Density [lb/in^3]	Cost [$/lb]
Aluminum Alloys	40-90	10-11	0.1-0.11	0.75-2.5
Titanium	100-200	16-18	0.16	15-50
High-strength Steel	250-300	30-32	0.283-0.292	0.6-1.5

In conclusion, Table 5.19 summarizes the main materials chosen for each component of the aircraft.

Table 5.19: Material selection for each aircraft component.

Aircraft Component	Selected Material
Wing	Aluminum Alloy 7075
Fuselage	Aluminum Alloy 7075
Tail	Carbon Fiber Reinforced Polymer
Landing Gear	High-Strength Steel

5.8. Weight and center of gravity

The weight of the main aircraft components are computed trough using analytical formulas found in the Raymer's book. However, there are notable exceptions. The weight of engine is given trough manufacturer data for the retained engine of the aircraft. It is the same for the optical system. Furthermore, the minimal values of the payload and the avionics' weight are fixed by the requirements for the aircraft.

Table 5.20: Weight and center of gravity of each component in the aircraft's maximum takeoff weight configuration.

Components	Weight [lbs]	Position of COG [ft]
Fuel in the fuselage	1 933.5	10.23
Wing + Fuel in the wing + Hydraulics	897.9	10.17
Engine	319	17.89
Payload + guided parachutes	783.1	9.84
Optical system	110.2	0.36
Air induction system	373.7	13.77
Fuselage	170.3	10.33
Electronics	449.7	9.64
Avionics	66.6	1.43
Instruments	10.01	1.42
Batteries	70.8	8.64
Main landing gear	108.6	2.95
Nose landing gear	37.4	11.41
Vertical tail	31.8	17.71
Horizontal tail + Hydraulics	19.4	16.33
Hydromechanical system of control surfaces	12.6	1.42
Maximum take-off weight	5 484.7	10.24
Maximum empty weight	2 519.44	10.29

The mass of batteries has been computed such that the power they provide ensures the requirement of the available cruise electrical power. They have been selected such that their energy density equates 8.5 [kWh · kg^{-1}]. Thus, it ranges between 5 and 12 [kWh · kg^{-1}] which are the energy densities given by the state-of-the-art[26].

It can be noticed that the mass corresponding to the hydraulics is distributed between the wing and the horizontal tail. The mass attributed to the hydraulics can be specified and it equates : $W_{\text{hydraulics}} = 38.36$ lbs.

One can notice that both the fuel in the fuselage and the payload are variable weights in addition to being the most significant weights. Therefore it is necessary that they are being close the center of gravity of the aircraft to prevent their destabilizing effect.

For further precisions, the center of gravity of the aircraft have been computed following the formula below, by taking into account the contributions of the different components :

$$x_{cg} = \frac{\sum m_i \, x_i}{\sum m_i} \tag{5.13}$$

where m_i is the mass of the component i and x_i corresponds to the position its center of gravity. A

better idea of the positions of the different components was in the fuselage section (Section 5.5).

This yields the most forward and the most backward aircraft center of gravity respectively $x_{\mathsf{cg,mf}} = 10.24$ ft and $x_{\mathsf{cg,mb}} = 10.29$ ft. They correspond respectively to a full aircraft configuration and an empty configuration.

5.9. Repairability

Estimating the reliability and maintenance involves evaluating the design and construction to determine the level of difficulty in performing the tasks. This involves identification, accessibility, complexity and replacement [27]. Wheels and tyres: Easy repair-ability. This is because they are changed as one unit, easy to access and the process to change them is straightforward. The tyres are also able to be re-treaded which is significantly less expensive than buying a new one. Windows and frames: Easy repair-ability. The aircraft features only one window on the bottom side of the nose which is easy to access without the need for any lifting devices. The process for replacing a window and frame is straightforward. Battery: Easy repair-ability. The battery is easy to access. The procedure for replacing it is very simple. Avionics: Easy repair-ability. The avionics is located in the nose of the aircraft, with access doors allowing easy access. Engine: Easy repair-ability. The engine is located in the fuselage at the rear of the aircraft. It is easy to access as multiple engine doors allow the major components of the engine to be accessed. Surface: Easy repair-ability. The skin is made of aluminium which is an easily malleable material thus making it easy to fix dents and cracks. However, the tail is manufactured from carbon fibre thus the repair ability is significantly more difficult as specialised equipment is needed.

6 Aircraft analysis

6.1. Static stability

Even if the aircraft is designed for performance following the requirements of the AIAA, it must ensure stability conditions in order to be able to fly safely. Therefore, a thorough analysis of the stability can be made by differentiating the pitch, the yaw and the roll stability.

6.1.1. Pitch stability

Relying on the equilibrium of the aircraft at each flight configuration, it is possible to determine the static stability of the aircraft. In pitch, this stability is essentially defined by the static margin :

$$K_n = -\frac{\partial C_m}{\partial C_{Lw}} \tag{6.1}$$

In order to have a sufficiently stable and maneuverable aircraft, the static margin has to be chosen such that $K_n \in [5, 15]\%$.

At first one needs to determine the neutral point of the aircraft. The latter corresponds to the aerodynamic center of the aircraft. It can be computed its non dimensional value relative to the leading edge of the wing as such :

$$h_n = h_0 + \frac{S_{HT} \, L_{HT}}{S_W \, \bar{\bar{c}}} \frac{C_{L_{\alpha,\text{tail}}}}{C_{L_{\alpha,\text{wing}}}} \left(1 - \frac{\partial \epsilon}{\partial \alpha}\right) - \frac{\partial C_{m,\text{fus}}}{\partial C_{Lw}} \tag{6.2}$$

where $\frac{\partial \epsilon}{\partial \alpha}$ is the downwash derivative with respect to the angle of attack and $\frac{\partial C_{m,\text{fus}}}{\partial C_{Lw}}$ accounts for the fuselage contribution, given by the empirical correlation of Gilruth and White [28]

Therefore, since the static margin also accounts for the distance between the neutral point of the aircraft and its center of gravity, it writes :

$$K_n == \frac{x_n - x_{cg}}{\bar{\bar{c}}} \tag{6.3}$$

where, $x_n = 13.87$ ft is the position of the neutral point relative to the nose of the aircraft. For the RADAR aircraft the static pitch stability is verified, as depicted in the following figure (Figure 6.1).
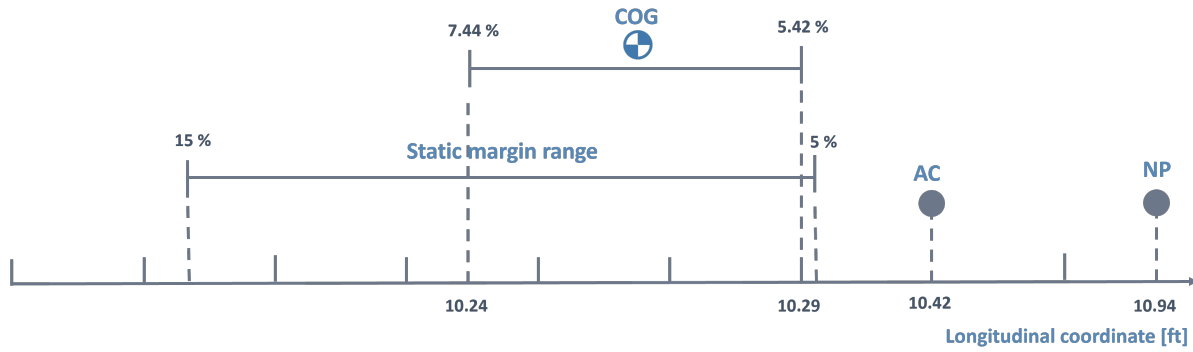
Figure 6.1: Evolution of the aircraft's center of gravity compared to the static margin range.

6.1.2. Yaw stability

The yaw stability can be assessed by verifying that the derivative of the yaw moment is negative:

$$\frac{\partial C_N}{\partial \beta} < 0 \tag{6.4}$$

Moreover the derivative of this yaw moment can be decomposed into different participation which include the involvement of the fin, the wing and the fuselage. These two last values can be found : $C_{N\beta,\text{fuselage}} = -0.1449$ and $C_{N\beta,\text{wing}} = -0.017$ since high-mounted wings have been chosen. Furthermore, the derivative of the yaw moment due to the fin yields : $C_{N\beta,\text{fin}} = C_{L_{\alpha,\text{fin}}} \frac{S_{VT} L_{VT}}{S_W b} = 0.0779$. Finally, the derivative of the yaw moment coefficient equates $C_{N\beta} = -0.0841$ which ensures lateral stability.

6.1.3. Roll stability

The roll stability can be ensured by considering the layout of the aircraft. In order for it to be stable in roll, one must ensure that center of gravity of the lifting surfaces is located above the center of gravity of the rest of aircraft components. And, since the RADAR aircraft features a top-mounted wing with no dihedral, the center of gravity of the rest of the components is necessarily below the wing. Therefore the aircraft is stable in roll.

6.2. Dynamic stability

The analysis of dynamic stability was carried out using the methodology described in the course of Flight Dynamics and Control (University of Liège) [29], which utilizes the USAF DATCOM approach [30].

to estimate aerodynamic derivatives empirically. These derivatives are then employed in the linearized equations of motion for an aircraft as presented in the mentioned course. The aforementioned aerodynamic derivatives can be found in Table 6.1. The computations were conducted at an altitude of 30,000 ft and under Mach 0.86.

Table 6.1: Dynamic stability and control derivatives for the RADAR aircraft. The methodology utilized was in accordance with the USAF DATCOM approach, as referenced in [30].

Longitudinal		Lateral	
C_{L_α}	5.307		
C_{D_α}	0.144		
C_{M_α}	-0.425		
C_{L_u}	0.750	C_{n_p}	0.067
C_{D_u}	0.063	C_{l_p}	-0.098
C_{M_u}	0.012	C_{y_p}	-0.032
C_{L_q}	5.106	C_{n_r}	-0.315
C_{D_q}	0	C_{l_r}	0.123
C_{M_q}	-14.972	C_{y_r}	0.032
$C_{L_{\dot\alpha}}$	1.332	C_{n_v}	0.319
$C_{D_{\dot\alpha}}$	0	C_{l_v}	-0.061
$C_{M_{\dot\alpha}}$	-9.662	C_{y_v}	-0.414

The stability derivatives are used to construct the state-space form of the equations of motion:

$$\dot{\mathbf{x}}(t) = \mathbf{A}\mathbf{x}(t) + \mathbf{B}\mathbf{u}(t), \tag{6.5}$$

where $\mathbf{x} = [u\ v\ w\ p\ q\ r\ \varphi\ \theta\ \psi]^T$ is the system states vector, i.e. velocities and angular velocities of the aircraft, and $\mathbf{u} = [\ \eta\ \zeta\tau]^T$ is the system inputs, i.e. the deflection angles for the ailerons, elevator, and rudder, as well as the thrust change. The latter is neglected for turbofans.

As in static stability, the pitch stability can be decoupled from the roll and yaw stability. Therefore, the equations of motion are usually split into longitudinal and lateral sets. Knowing this and the aerodynamic derivatives, it is possible to rewrite the linearized equations of motion in the state-space form. The aircraft is dynamically stable as all the real parts of the eigenvalues of $\mathbf{A}$ are negative (cf. Table 6.2). The aerodynamic derivatives for control surfaces were not included in the analysis since they are part of matrix $\mathbf{B}$, which is not involved in the eigenvalues of matrix $\mathbf{A}$. Moreover, since the analysis concentrates on the cruise condition, their influence is insignificant.

Table 6.2: Eigenvalues of **A** for longitudinal and lateral equations of motion of RADAR.

Longitudinal	Lateral
-0.7339 + 2.3163ii	0
-0.7339 - 2.3163i	0.0274
-0.0029 + 0.0578i	-1.0174
-0.0029 - 0.0578i	$-0.4810 \pm 5.6562i$

The flying qualities of the Radar aircraft are evaluated according to M.V. Cook [31] for flight phase category B (cruise) and presented in the two following subsections.

6.2.1. Longitudinal vibration modes

The two complex conjugated pairs from the longitudinal part of Table 6.2 represent two oscillatory vibration modes. These modes of vibration, called phugoid and short-period oscillations, are characterized by their frequencies and damping ratio presented in Table 6.3. The phugoid mode has a very large period oscillation with low damping while the short period oscillation mode represents a highly damped motion. To satisfy the level 1 requirements, the damping ratio for the phugoid should be higher than 0.04, while it should be between 0.30 and 2.00 for the short-period oscillations mode. According to M.V. Cook [31], there are no requirements on the frequencies, but "it is suggested that handling difficulties may become obtrusive if the frequency ratio of the modes $\omega_p/\omega_s \leq 0.1$", which is not the case.

Table 6.3: Frequencies and damping ratios of the longitudinal modes.

	Phugoid	Short period oscillations
Frequency ω [rad/s]	0.0579	2.430
Damping ratio ζ [-]	0.0497	0.302

It is reasonable to deduce that the obtained results are logical due to the short-period mode exhibiting a comparatively higher damping ratio and a significantly higher frequency in contrast to the phugoid mode.

6.2.2. Lateral vibration modes

The complex conjugate eigenvalues correpsonds to the only oscillatory mode, i.e. the dutch roll. There remain two non-oscillatory modes characterized by a time constant. The roll subsidence mode corresponds to the most negative real eigenvalue, representing high damped motion. The spiral mode is

characterized by a large time constant and represents low damping. It normally corresponds to the lowest negative eigenvalue, but in this case this value is positive but very close to zero. The remaining eigenvalue equal to zero is due to the fact that aircraft have little or no restoring moment in the roll direction. The Level 1 flying qualities are respected for lateral modes $\omega_{Dutch\,roll}\zeta_{Dutch\,roll} > 0.15$, $\tau_{Roll\,subsidence} < 1.4$, and $\tau_{spiral} > 28.9$.

Table 6.4: Frequencies, damping ratios, and time constants of the lateral modes.

	Frequency ω [rad/s]	Damping ratio ζ [-]	Time constant τ [s]
Roll subsidence	-	-	0.333
Spiral mode	-	-	36.461
Dutch roll	5.677	0.085	-

6.3. Aerodynamics

In this section, we will conduct a detailed analysis of the aerodynamic characteristics of an aircraft to obtain more accurate results than those achieved in the conceptual design phase. The aerodynamic study will be divided into two parts: lift analysis and drag analysis. For lift analysis, we will employ DART-Flo (Discrete Adjoint for Rapid Transonic Flows) [32], which is an open-source C++/Python unstructured finite-element solver for full-potential problems developed at the University of Liège. DARTFlo enables us to simulate the airflow around the aircraft's wing and compare the obtained results with the empirical data used in the conceptual design phase. It is worth mentioning that only the wing's aerodynamics will be studied on DARTFlo. On the other hand, the drag analysis will be based on an empirical evaluation following Torenbeek's Synthesis of Subsonic Airplane Design [15].

6.3.1. Drag analysis

Based on the guidelines provided in Torenbeek Appendix F and G [15] for estimating the aircraft drag in cruise and low-speed configurations respectively, the total drag was decomposed into several components as illustrated in Figure 6.2. During the study the cruise has been segmented into three distinct phases, namely ingress, loiter, and egress, while the low-speed phase has been subdivided into take-off and landing phases.
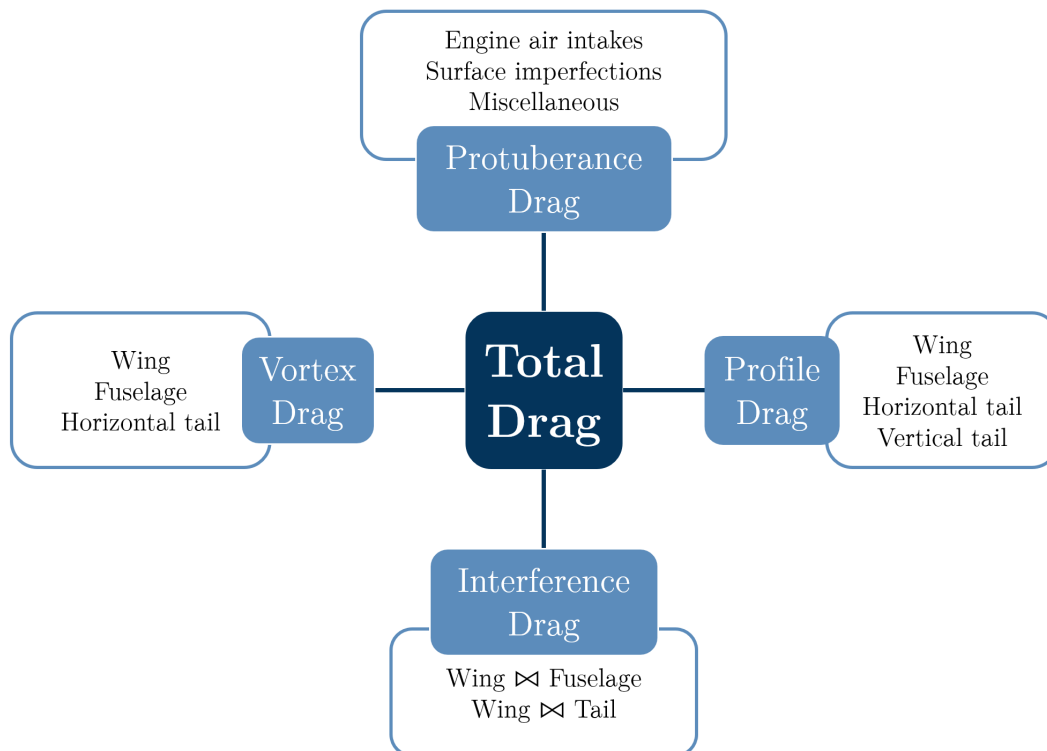
Figure 6.2: Drag breakdown.

Several assumptions have been made in the calculation of our different contributions. First, when calculating the vortex drag, all main aircraft parts have been considered as isolated bodies in order to be able to calculate it accurately using classical potential flow theory. Then, for the calculation of the vortex drag, the wing, the fuselage and the tail have been assumed to have fully turbulent boundary layer due to the high cruise speed. Moreover, to calculate the vortex drag, we initially assumed that the aircraft parts were smooth and the flow was incompressible. However, we later relaxed these assumptions to incorporate the effects that are encountered in reality.

- **Vortex drag** is primarily caused by the formation of wing tip vortices. These vortices redirect the airflow downwards, resulting in a decrease in the effective angle of attack experienced by the wing. As a result, there is a reduction in the lift and an increase in the drag produced by the wing. In order to compute the vortex drag, a correlation method is used. The latter approximates the results of the Prandtl Lifting Line Theory for the wing and the tail. Additionally, a correction factor is applied to account for the wing twist. Furthermore, the fuselage vortex drag is computed based on experimental data, using a correlation method.

- **Profile drag** arises from the interaction between the air and the aircraft surface. It is mainly caused by the boundary layer and regions of separated flows around an isolated aircraft com-

ponent. Profile drag can be further divided into two components: skin friction drag and pressure drag. To estimate profile drag, a corrected flat plate analogy is used, which accounts for the effects of lift. The calculation of profile drag is based on the skin friction coefficient C_F of a flat plate with a fully turbulent boundary layer provided by Prandtl-Schlichting [33]:

$$C_F\Big|_{\text{incomp}} = \frac{0.455}{\log_{10}(Re)^{2.58}} \ .$$

(6.6)

As we operate at transonic speed, we had to take into account the effects of compressibility. This has been done by the following formula proposed by Clauser [34].

$$C_F\Big|_{\text{comp}} = C_F\Big|_{\text{incomp}} \left(1 + 0.15 \, M^2\right)^{0.58} \ .$$

(6.7)

- **Interference drag** results from the interactions between different components of the aircraft (neglected in the vortex drag computation). In the preliminary design phase, it is challenging to evaluate interference drag accurately. However, some correlations are available to account for the most important effects such as viscous interference at the intersections of the components and the downwash effect on the horizontal tail due to wing lift. It should be noted that this contribution can be negative. Indeed, this can occur when the interference between the different components of the aircraft results in a beneficial aerodynamic effect. Despite being a minor contributor to the overall drag coefficient, interference drag should not be overlooked as it can become significant, particularly at high angles of attack.

- **Protuberance drag** includes various sources of drag that cannot be attributed to other categories, such as surface imperfections (neglected in the profile drag computation), undercarriage and miscellaneous lift-dependent drag. To accurately evaluate the drag contribution of these components, all external parts of the aircraft must be considered. Empirical corrections and statistical data were required to estimate the drag due to protuberances and imperfections. This calculation involves a combination of known geometries (intake scoop drag) and statistical data (drag of rivets, joints, gaps and leaks) to accurately predict the drag contribution of these components.

Drag Polar

Formation of the drag polar is made possible through the established drag breakdown. Calculating the j drag components, given by the equation $C_{D_j} = A_j + B_j C_L + D_j C_L^2$, is a necessary step in this process. The value of C_{D_j} is obtained as $C_{D_j} = (C_D S)_j/S$, where $(C_D S)_j$ represents the drag area, and S represents the gross wing area. Subsequently, the drag areas can be summed up to determine the total drag coefficient C_D. The equation for C_D can be expressed as

$$C_D = \frac{\sum_j (C_D S)_j}{S} = A + B C_L + D C_L^2. \tag{6.8}$$

(a) Drag polar in ingress and egress.

(b) Drag polar in loiter.
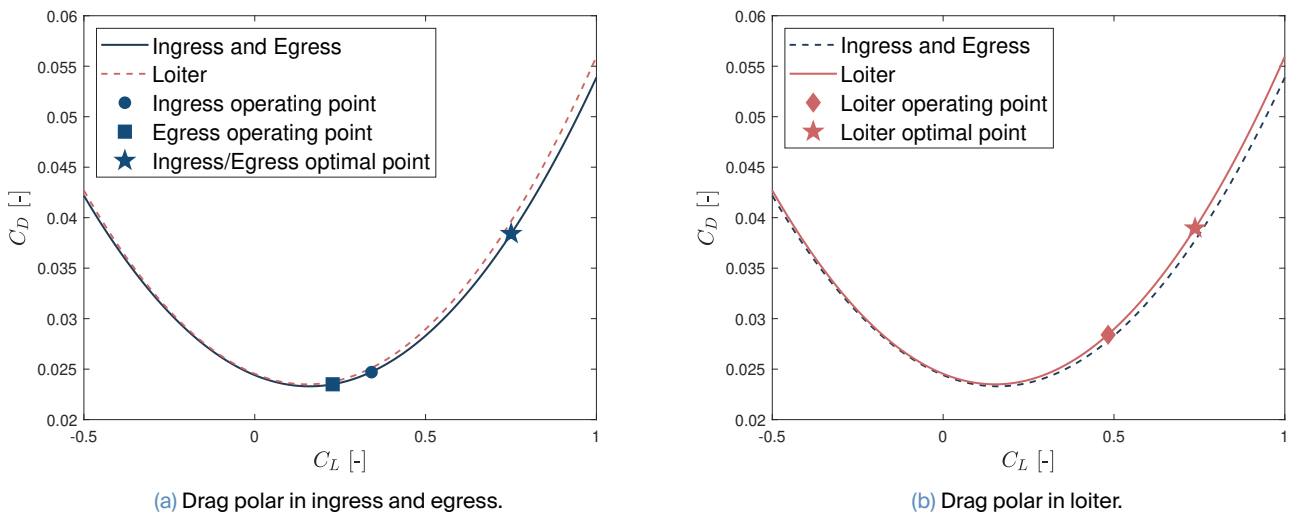
Figure 6.3: Drag polar in Cruise with the position of the working and optimal points.

The primary objective of a C_L/C_D plot is to identify the maximum lift-to-drag ratio (L/D) of the aircraft. However, during take-off and landing, the focus shifts from maximizing this ratio to generating a significant amount of lift at the expense of drag. For instance, during takeoff, the priority is to produce a high amount of lift, while during landing, the goal is to reduce speed *i.e.* produce drag and touch down gently *i.e.* produce lift. As a result, emphasis was placed on Cruise polar drag rather than Low-speed polar drag because the analysis of the maximum L/D (or C_L/C_D) ratio is less relevant during these phases. For the sake of readability, the ingress and egress phases have been analysed independently of the loiter phase. Nevertheless, their respective plots are displayed in dashed line to highlight their proximity (see Figure 6.3). It is worth noting that the ingress and egress phases are so similar that their respective curves overlap. Therefore, they share the same optimal point.

Although Figure 6.3 indicates that we are not operating at the optimum, it does not necessarily indicate poor aircraft design. It is important to recognize that in practice, an aircraft cannot always fly at its optimum due to structural limitations. Optimal flight conditions typically result in high aerodynamic forces, which could compromise the structural integrity of the aircraft. Furthermore, operating too close from the optimum can result in instability in the aerodynamics of the aircraft, which can lead to a loss of control and increase the risk of stalling and crashing. Therefore, a balance between achieving optimal performance and ensuring safe operation under various conditions must be struck. Further information on the operating points, particularly on the operating C_L and C_D, can be found in the independent analysis conducted in the following paragraphs.

Cruise

In order to particularise our study to the cruise phases it is necessary to impose a lift coefficient C_L in order to extract a drag coefficient C_D. After determining the C_L values for each phase such that half of the fuel of the concerned phase has been consumed, the C_D values were obtained based on the polar drag.

Table 6.5: Cruise configurations.

	C_L	C_D
Ingress ($M = 0.86$)	0.3418	0.0247
Loiter ($M = 0.7$)	0.4830	0.0284
Egress ($M = 0.86$)	0.2281	0.0235
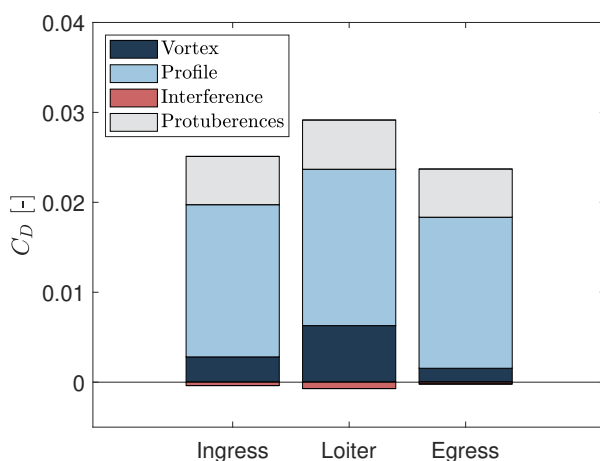
(a) Contributions of drag sources.
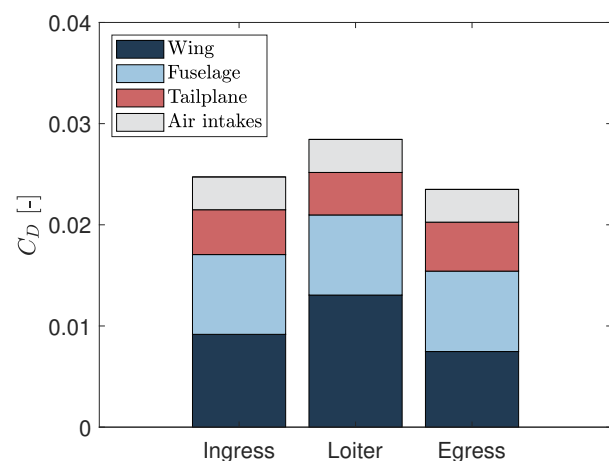
(b) Contributions of aircraft parts.

Figure 6.4: Contributions of the drag coefficient C_D during the cruise phases.

Two distinct approaches were employed to analyse the drag coefficient. The first approach involves separating the various drag sources based on physical characteristics (vortex, induced, interference and protuberance), while the second approach examines the contributions from different parts of the aircraft (wing, fuselage, tailplane and air intakes). These distinct contributions are depicted in Figure 6.4a and Figure 6.4b, respectively. It should be noted that the interference drag makes a negative contribution but it is currently negligible (on the order of 10^{-4}). Its impact will be further analyzed in the takeoff and landing phases.

It is important to emphasize that the C_L computations have been performed for the mid-fuel configuration. However, it is possible to calculate the drag coefficient at any point during the mission as demonstrated in Section 5.3 and as it will also be explored in Section 6.5. As a result, it is not surprising to encounter varying drag coefficient values in these sections.

Take-off and Landing

In principle, all drag contributions discussed during cruise phases undergo some modifications when flaps are deflected. However, only the most relevant corrections needed will be discussed. The low-speed phases analysis will start with the polar drag in the clean configuration *i.e.* cruise. Then, the focus will be on the increase in the profile, vortex, and trim drag coefficients as a result of flap deflection. Furthermore, the influence of both undercarriage extension and ground effect will be considered.

- **Drag due to the extension of retractable undercarriage** is mainly due to the increase in the profile component. As the landing gear is extended, it creates additional surface area which leads to an increase in the pressure drag component. Moreover, the landing gear creates a non-streamlined shape, which generates turbulence and separation of the airflow. To determine the drag associated with the undercarriage, the frontal surface of the two main wheels, the nose wheel, and the length of the landing gear legs, were taken into account. An empirical formula, which included a factor based on Helmholtz's theorem was then used to deduce this term.

- **Ground effect** refers to the increase in lift and decrease in induced drag that occurs when an aircraft is flying close to the ground. This is because the ground creates a cushion of high-pressure air that reduces the amount of air flowing around the wingtips and hence the vortices that contribute to induced drag. However, the decrease in induced drag can be partially offset by an increase in the profile drag, which results from the compression of the air between the wing and

the ground. The calculation of the reduction in vortex drag has been based on the vortex drag of the wing without the influence of ground effect. Furthermore, the computation of the reduction in drag due to ground effect also accounted for a term related to the profile drag of the wing, which is caused by the reduced effective flow velocity (different from that due to the compression of the air). It should be noted that the calculation did not take into account the effects on trim drag (vortex drag of the horizontal tail). This is due to the considerable amount of effort that would be required to accurately calculate it, which may not be justifiable given the inherent inaccuracies in the computation.

At take-off the *single slotted* flaps are deployed with a deflection angle $\delta_f = 20°$ while at landing it is $\delta_f = 45°$. It is worth mentioning that the lift coefficient has been calculated again during the middle of the phase *i.e.* at a point where half of the fuel allocated for that phase had already been used up.

Table 6.6: Low-speed configurations.

	C_L	C_D
Take-off ($\delta_f = 20°$)	0.7634	0.2126
Landing ($\delta_f = 45°$)	0.9905	0.3618

(a) Contributions of drag sources.

(b) Contributions of aircraft parts.
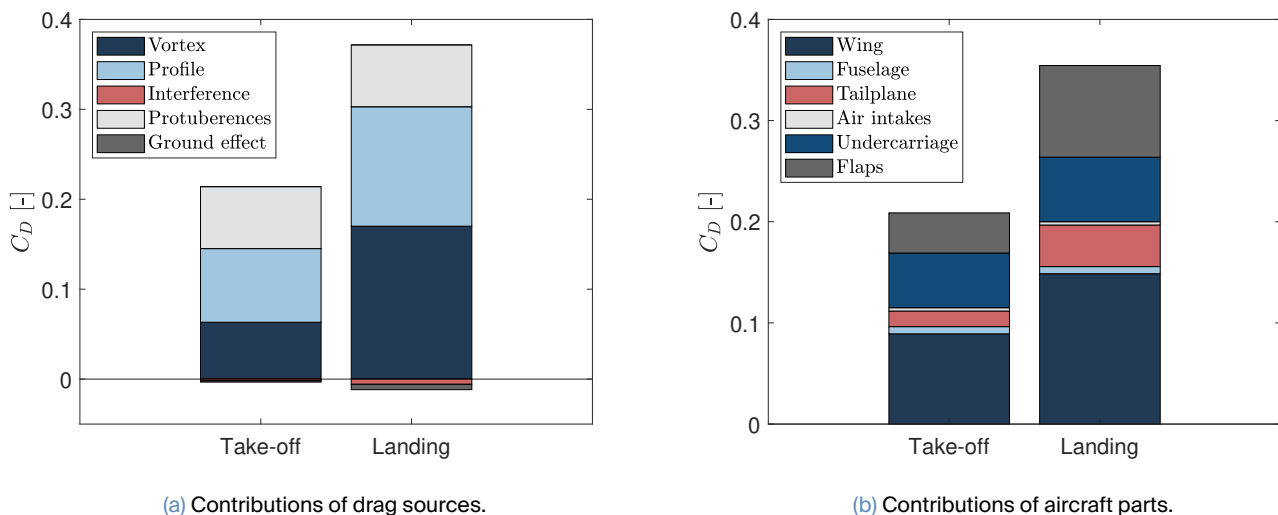
Figure 6.5: Contributions of the drag coefficient C_D during the low-speed phases.

One significant finding is the negative effect of drag interference, which becomes particularly pronounced at high angles of attack. Interestingly, this component has a negative value, meaning that it actually reduces drag. This result, which seems physically impossible at first, is discussed in Torenbeek Section F-4.2 (Appendix F) where a negative drag increment for high-wing configuration is associated

with the wing/fuselage interference. Moreover in Section F-4.4 (Appendix F), it is stated that "[...] *It is noted that* [Wing/tailplane interference] *can represent a negative term, i.e. a drag reduction".* In addition, as expected, we observe a decrease in drag coefficient due to the ground effect.

Engine failure

The drag increment in steady flight following engine failure can be estimated by computing the engine windmilling drag.

- **Engine windmilling drag** occurs when the engine compressor and turbine blades rotate due to the airflow, even though the engine is not providing power. In practice, we therefore encounter this situation when an engine fails or is intentionally shut down in flight. To evaluate the increase in drag related to this case we use a formula based on the speed of the aircraft, the area of the nozzle, the diameter and type of the engine (high bypass, low bypass...).

$$\Delta C_{D_{\text{Ingress}}} = \Delta C_{D_{\text{Egress}}} = 0.0121 \qquad \text{and} \qquad \Delta C_{D_{\text{Loiter}}} = 0.0122 \ . \tag{6.9}$$

These increments lead to the following drag coeffients (Eq.6.10). Theses correspond to increases of 48%, 43% and 73% respectively which may significantly impact the gide distance of the aircraft.

$$C_{D_{\text{Ingress}}} = 0.0367 \qquad C_{D_{\text{Loiter}}} = 0.0406 \qquad C_{D_{\text{Egress}}} = 0.0355 \ . \tag{6.10}$$

6.3.2. Lift analysis

The second phase of the aerodynamic investigation is specifically allocated for the purpose of examining the lift behavior of the wing. The study involves an exploration of the wing lift behavior under various flight conditions such as cruise and loiter, while also varying the angle of attack. In addition, the examination involves a comparative analysis of the total drag produced by the aircraft and the drag produced solely by the wing with respect to the findings of the drag analysis. Furthermore, this study includes a comparison between the empirical correlations and the simulation results obtained through DART.

Lift produced by the wing

As the primary component responsible for producing lift, the wing plays a crucial role in aircraft performance. Thus, analyzing the lift generated by the wing and ensuring its adequacy throughout different flight phases is of utmost importance. To achieve this, an investigation of the wing lift behavior as a function of the angle of attack is conducted. Based on this analysis, an optimization of the angle of

incidence of the wing on the fuselage is carried out to produce the required lift during cruise, utilizing the DART simulation. The comparison between the results obtained from the empirical data and the numerical data is presented in Table **??**.

Table 6.7: Optimization of the angle of incidence of the wing on the fuselage for cruise conditions (M 0.86) using DART.

Parameter	Empirical	DART
Angle of incidence, i_w [°]	1.16	1.16
Aircraft lift coefficient at zero AoA, C_{L0} [-]	0.31	0.35

Now that the optimal angle of incidence has been established, it is possible to examine the evolution of the lift produced by the wing in relation to the angle of attack of the fuselage. The comparison between the numerical and empirical data is visually presented in Figure 6.6

(a) Cruise (Mach 0.86)   (b) Loiter (Mach 0.7)
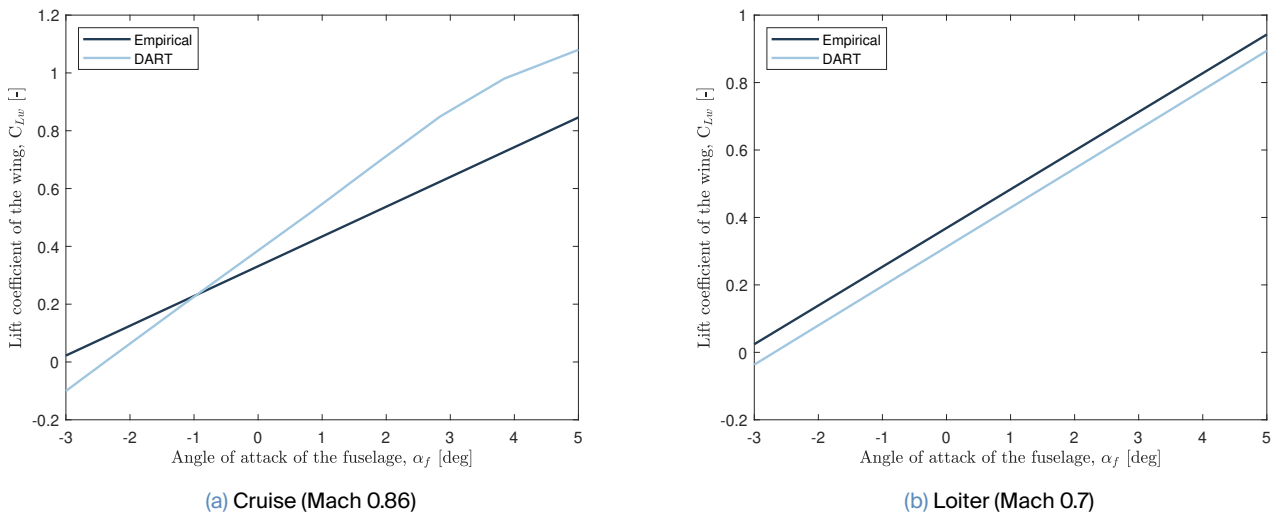
Figure 6.6: Evolution of the lift produced by the wing with respect to the angle of attack.

By examining the graphs presented, it is feasible to update the lift curve slope of the wing through the implementation of the results obtained from the DART simulation. The comparison and subsequent update of the lift curve slope of the wing for both flight phases are condensed and presented in Table 6.8..

Table 6.8: Comparison of the lift curve slope of the wing in cruise and loiter conditions.

Parameter	Cruise	Loiter
Lift curve slope of the wing, $C_{L_{\alpha w}}$ (DART) [1/rad]	9.33	6.67
Lift curve slope of the wing, $C_{L_{\alpha w}}$ (Empirical) [1/rad]	5.9	6.57

Lift distribution on the wing

The distribution of lift along the span of the wing can be determined using DART in cruise and loiter. The distribution of lift along the half span of the wing is represented on Figure 6.7.

(a) Cruise (Mach 0.86)

(b) Loiter (Mach 0.7)
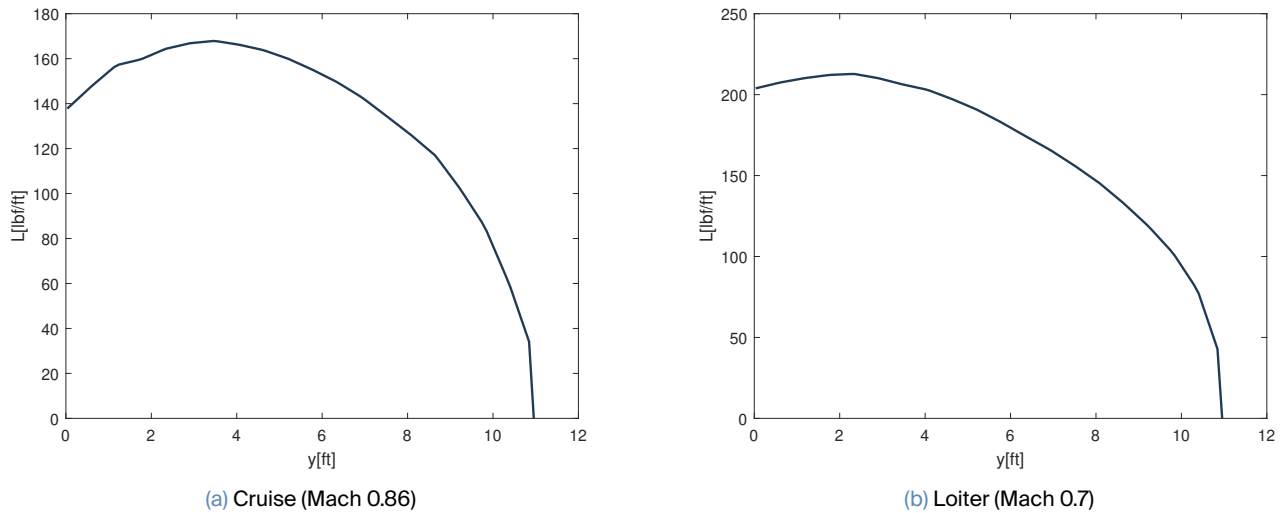
Figure 6.7: Lift distribution along the span of the wing in different flight phases.

Comparison of the drag produced by the wing

A comparison can be made between the drag computed with DART and the one computed in the drag analysis. The comparison is summarized in Table 6.9 for the cruise and loiter phases.

Table 6.9: Comparison of the drag coefficient of the wing computed with DART and computed during the drag analysis.

	Cruise (Mach 0.86)	Loiter (Mach 0.7)
Drag coefficient of the wing,C_{Dw} (DART) [-]	0.0164	0.012
Drag coefficient of the wing,C_{Dw} (Drag analysis) [-]	0.0092	0.0131
Drag coefficient of the wing,C_{Dw} (Empirical correlation) [-]	0.0209	0.0252

Upon inspection, it can be observed that the drag values computed using DART differ from those computed during the drag analysis in cruise conditions. This disparity can be attributed to the assumptions made during the DARTFlo simulation. Specifically, DARTFlo considers an inviscid flow around the wing, meaning that the effects of viscosity are neglected. In the presence of a shock wave, such as in cruise conditions, the drag is overestimated. This occurs because the shock wave's effects on the drag are not fully captured since the shock wave generates viscous effects such as turbulence and boundary layer thickening, which are not accounted for under the assumption of an inviscid flow.

Comparison of the drag produced by the aircraft

A further comparison can be carried out between the results obtained from the DART simulation and the empirical correlations, by evaluating the drag of the entire aircraft. This can be achieved by comparing the drag polar of the aircraft throughout different flight phases. The comparison of the drag polar is presented in Figure 6.8.

(a) Cruise (Mach 0.86)   (b) Loiter (Mach 0.7)
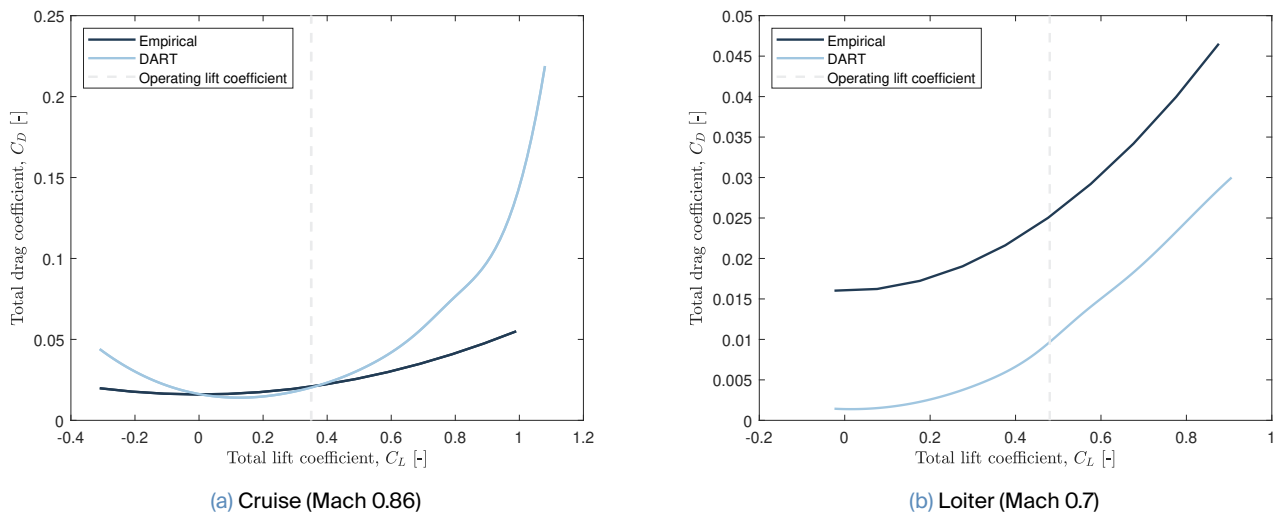
Figure 6.8: Comparison of the drag polar in cruise and loiter conditions between the empirical correlations and DART.

The comparison between the drag polar obtained from the empirical correlations and the DART simulation reveals that the drag polar curves are highly consistent in cruise conditions. In contrast, the empirical correlations tend to overestimate the drag in loiter conditions, which appears to be an anomaly when compared to the results provided by DART. Therefore, it is advisable to rely on the drag values estimated by DART, as they appear to provide more accurate results.

6.4. Structural analysis

During the conceptual design of the aircraft, the structural analysis allows to define the internal layout which will be able to withstand the diverse loads encountered by the aircraft. As a semi-monocoque structure is often chosen for the aircraft, the internal layout generally consists of stringers, frames, ribs and spars. Thus, the first step is to determine the flight envelope. This result will help identify the flight phases where the aircraft endures the most severe loads. The obtained aerodynamic loads can be analyzed to determine the loads acting on the rear fuselage and at the wing root. This will then lead to the analytical structural design of the considered parts. Such analysis can be completed by the finite

element analysis which can also be used as a comparison to the analytical results.

6.4.1. Placard diagram

The Placard diagram highlights the evolution of the aircraft velocity with respect to altitude. In order to perform this diagram, the design cruise velocity needs to be obtained. Its value is $V_c = 543.2572$ kts, it corresponds to the dash speed and it will be explained in the section 6.5.4

It can be noticed that, above the design altitude, the aircraft flies at the design Mach number M_c corresponding the design cruise velocity V_c. Yet, below the design altitude, it is of significant matter to keep the drag of the aircraft constant with altitude. Therefore, the true airspeed needs to decrease with altitude. In order to get rid of the altitude dependency, the equivalent velocity can then be used :

$$V_e = \sqrt{\frac{\rho}{\rho_0}} \, V_{\text{true}} \tag{6.11}$$

where ρ_0 represents the density at sea level in ISA conditions and ρ defines the density at the considered altitude.

It is also necessary to consider the design dive velocity as it defines as the maximum attainable velocity of the aircraft. The design dive mach number M_D can then be defined as follows :

$$M_D = \min\{M_{D1}, M_{D2}\} \tag{6.12}$$

where $M_{D1} = 1.25 \, M_c$ and M_{D2} corresponds the mach number obtained after a 20-second dive at $7.5°$ followed by a 1.5-g pullout

Furthermore, the ceiling, defined as the altitude where the density becomes too small to produce enough lift, is found to be 38735 [ft]. To obtain the value, one needs to examine the climb performance, which will be elaborated on in the next section. In addition, the requirements of the aircraft are such that the design cruise altitude is equal to 30000 [ft].

6.4.2. Maneuver envelope

The maneuver and gust envelopes highlight the different loads encountered by the aircraft in several critical conditions corresponding to different airspeeds. The goal is to unveil a flight envelope within
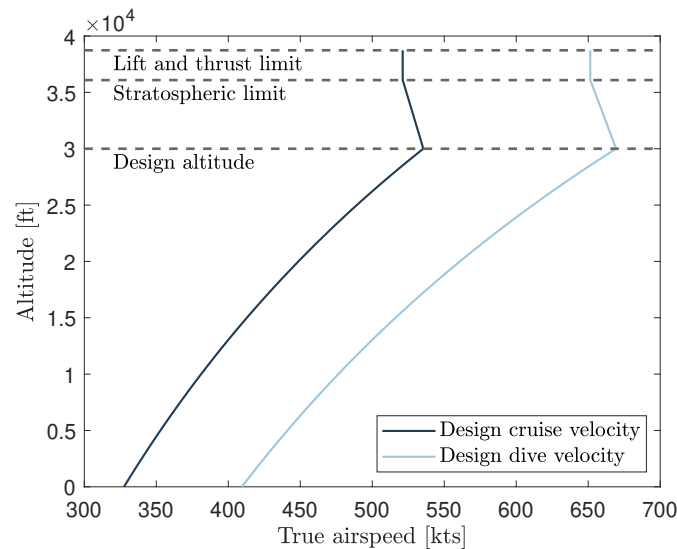
Figure 6.9: Placard diagram for the RADAR aircraft with the design altitude 30000 ft.

which the aircraft can navigate without fearing any structural damage. Hence, in this part, it will be summarized the methodology in order to obtain the flight envelope.

At first, it is necessary to consider the load factor. The extremum values of the load factor that the aircraft can bear are given by the AIAA requirements.

Moreover, the design cruise and dive velocities are prominent parameters of the flight envelope are have been obtained in the previous subsection (Sec 6.4.1).

The design maneuvering speed, V_A, constitutes, as well, a significant velocity in the maneuver envelope. In effect, it defines the velocity below which the aircraft must be capable of withstanding full deflection of its control surfaces. It is defined as $V_A = \sqrt{n_{\max}}\, V_{\text{sl}}$ where $V_{\text{sl}} = \sqrt{\frac{2W}{\rho_0\, C_{\text{L,MAX}}\, S_{\text{ref}}}}$ represents the stall speed of the aircraft.

The maneuver envelope can be achieved by computing the positive and negative stall lines. These are defined in the following equation (Eq.6.4.2). One must be cautious that the airspeed considered for the maneuver envelope is the equivalent airspeed.

$$n_+(V) = \rho_0 \frac{V^2\, S_{\text{ref}}\, C_{L_{\max}}}{W} \quad \text{and} \quad n_-(V) = -\rho_0 \frac{V^2\, S\text{ref}\, C_{L_{\max}}}{W} \tag{6.13}$$

As the aircraft is subjected to gust loads, it is of particular importance to take them into account in the structural loads encountered by the aircraft. The maximal equivalent gust speed has been obtained experimentally for different altitudes. Therefore, it can be found trough interpolation for the design altitude of the aircraft and it yields : $U_{\text{E,C}} = 36.2867$ [ft/s] and $U_{\text{E,D}} = 18.1433$ [ft/s]
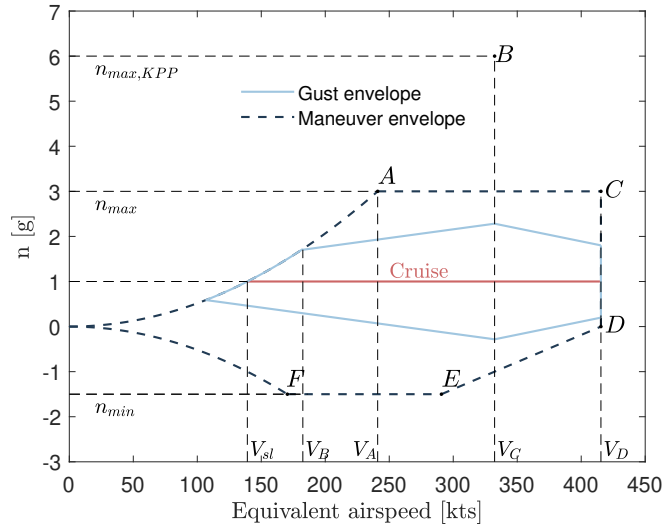
Figure 6.10: Maneuver envelope and gust envelope for the RADAR aircraft at the altitude 30000 ft.

Furthermore, the regulation authorities allow manufacturers to alleviate the gusts encountered. Therefore, it can be used gust-related parameters such as the aircraft mass ratio, μ_g, which will lead to the gust alleviation factor, F.

$$\mu_g = \frac{2\,(W/S_{\text{ref}})}{\rho\,\bar{\bar{c}}\,C_{L_{\alpha,\text{plane}}}\,g} \quad \text{and} \quad F = \frac{0.88\,\mu_g}{5.3 + \mu_g} \tag{6.14}$$

This leads to the computation of the gust load factor (Eq. 6.15). The latter parameter, as shown in Fig. 6.10, strongly influences the flight envelope and therefore the maneuvering velocities of the aircraft.

$$n_{g,C\pm} = 1 \pm \frac{F\,U_{\text{E,C}}\,V_e\,C_{L_{\alpha,\text{plane}}}}{498\,(W/S_{\text{ref}})} \quad \text{and} \quad n_{g,D\pm} = 1 \pm \frac{F\,U_{\text{E,D}}\,V_e\,C_{L_{\alpha,\text{plane}}}}{498\,(W/S_{\text{ref}})} \tag{6.15}$$

Table 6.10: Relevant equivalent velocities of the flight envelope.

	Velocities [KEAS]
Stall speed, V_{s1}	139.1118
Design maneuvering speed, V_A	240.9487
Design speed for maximum gust, V_B	182.4843
Design cruise speed, V_C	327.5527
Design dive speed, V_D	409.4409

Table 6.11: Relevant load factors at cruise altitude (30000ft).

n_{min} [–]	n_{max} [–]	$n_{\text{max,KPP}}$ [–]
-1.5	3	6

Note that $n_{\text{max,KPP}}$ corresponds to the Minimum Free Flight Loads, which is one of the Key Performance Parameters (KPPs) defined by the American Institute of Aeronautics and Astronautics (AIAA).

Thereafter, the analytical and finite element study will be conduced considering several critical velocities and load factors in the flight envelope. They are displayed in the following table.

Table 6.12: Critical load factors for the RADAR aircraft.

	Load factor [-]	Velocities [ft/s]
A	3	240.9487
B	6	327.5527
C	3	409.4409
D	0	409.4409
E	-1.5	286.6086
F	-1.5	170.3765

6.4.3. Aerodynamic loads

This section aims at defining the different loads acting on the aircraft during the critical flight conditions. Therefore, a system of equations will be solved for the considered conditions. Some parameters can be already taken into account following the FAR 23.423 and FAR 23.441 regulation such as the maximum pitch acceleration $\ddot{\theta} = 60°/s^2$ and the maximum yaw angle $\psi = 15°$. The other terms of the system of equation can be displayed below :

- L_W and L_T are respectively the lift of the wing and that of the horizontal tail

- D_W and D_T are respectively the drag of the wing and that of the horizontal tail

- nW is the weight term accounting for the load factor

- T is the thrust generated by the engine

- D_b is the body drag

- M_W and M_T are respectively the pitching moment induced by the wing and by the tail
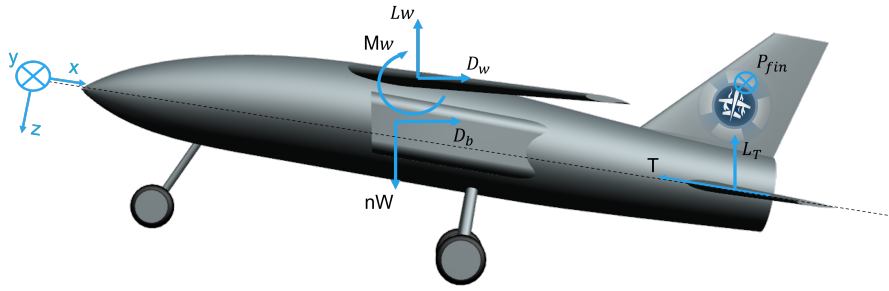
Figure 6.11: Representation of the aerodynamical loads.

Therefore, the vertical forces equilibrium and moment equilibrium around the wing root leading edge can be displayed :

$$
\begin{cases}
L_W + L_T = n\,W - T\,\sin(\alpha) \\
L_T\,l_{L_T} - L_W\,l_{L_W} = I_\theta\,\ddot{\theta} - M_T - M_W - D_b\,l_{D_b} + D_T\,l_{D_T} - D_W\,l_{D_W} - T\,l_{\text{thrust}}
\end{cases}
\tag{6.16}
$$

where, l_i represents the lever of the considered force i and I_θ is the moment of inertia of the fuselage around the center of mass, computed through the CAD study.

Furthermore, another equation must be accounted for to complete the system of equations constituted of three unknowns (α, L_W, L_T). It leads to the equation of the lift of the wing:

$$
L_W = \frac{1}{2}\,\rho\,V^2\,S_{\text{ref}}\,C_{L_{\alpha,\text{wing}}}\,\sin(\alpha - i_w)
\tag{6.17}
$$

where, α and i_w correspond to the angle of attack and the angle of incidence, respectively. The angle of incidence is the angle between the wing and the fuselage.

The fin loading can also be computed considering the maximum yaw angle :

$$
F_{\text{fin}} = \frac{1}{2}\,\rho_0\,V_e^2\,S_{HT}\,a_T\,\psi
\tag{6.18}
$$

where a_T is the vertical tail lift curve slope.

Table 6.13: Aerodynamic loads applied on the wing, on the tail and on the fuselage at the critical envelope points.

	A	B	C	D	E	F
α [°]	16.6746	17.6795	7.3443	2.5099	-2.2658	-10.6175
L_W [$10^3 \cdot$ lbf]	17.9680	35.4616	19.1550	2.1971	-7.1320	-7.5931
L_T [$10^3 \cdot$ lbf]	-0.9428	-1.2804	-2.0543	-2.2153	-1.4272	-0.8899
F_{Fin} [$10^3 \cdot$ lbf]	0.5704	1.0541	1.6470	1.6470	0.8070	0.2852
M_{fus} [lbf.ft]	153.2437	283.2017	442.5027	442.5027	216.8263	76.6219

6.4.4. Structural loads

In the next subsections, it will be analyzed the structural loads acting on the rear fuselage and at the wing root. The rear fuselage starts with a section located at the wing root trailing edge.

6.4.5. Structural loads acting on the fuselage

It is, at first, necessary to determine the forces that are applied at the aft of the fuselage. Those are :

- W_{tf} the added weights of the tail and the fin,

- W_{e} the weight of the engine,

- W_{rf} the weight of the rear fuselage.

Since different cuts have been considered on the rear fuselage, one can then retrieve the structural loads on each section of the fuselage.

$$
\begin{cases}
T_{yi} = -F_{\text{fin}} \\[2mm]
T_{zi} = -\left(n\left(W_{\text{tf}} + W_{\text{e}} + W_{\text{rf}}\right) - L_T\right) \cos\left(\alpha - i_w\right) \\[2mm]
M_{yi} = \left(n\left(x_{\text{tf}}^i W_{\text{tf}} + x_{\text{e}}^i W_{\text{e}} + x_{\text{rf}}^i W_{\text{rf}}\right) - L_T\, x_{ac}\right) \cos\left(\alpha - i_w\right) \\[2mm]
M_{zi} = F_{\text{fin}}\left(x_{\text{tf}} - x_i\right) \\[2mm]
M_{xi} = -F_{\text{fin}}\, z_{tail}
\end{cases}
$$

where, x^i represents the distance of the forces relative to the considered section i.

The following table displays the loads acting on the rear fuselage for different flight conditions at the root section of the rear fuselage. Indeed this section bear the highest loads.

Table 6.14: Structural loads at the fuselage root section for the different critical flight conditions.

	A	B	C	D	E	F
T_y [$10^3 \cdot$ lbf]	-0.5704	-1.0541	-1.6470	-1.6470	-0.8070	-0.2852
T_z [$10^3 \cdot$ lbf]	-2.1521	-3.7040	-3.3298	-2.2134	-0.7757	-0.2348
M_x [$10^3 \cdot$ lbf.ft]	-1.1524	-2.1296	-3.3275	-3.3275	-1.6305	-0.5762
M_y [$10^3 \cdot$ lbf.ft]	9.1908	16.1888	13.5123	8.0320	2.0951	0.1446
M_z [$10^3 \cdot$ lbf.ft]	2.0697	3.8249	5.9765	5.9765	2.9285	1.0349

6.4.6. Structural loads acting on the wing

In this part, it will considered the loads acting on the wing root. One can be reminded the local coordinate system selected for this part of the study. The origin is taken at the wing root leading edge. The x-axis is directed along chord of the wing root and is positive when oriented to the trailing edge. The y-axis is directed along the span of the half-wing. And finally the z-axis is positive downwards.

Since fuel weight can counterbalance lift, the critical case is achieved when the fuel tank is empty. Therefore, in the analysis, the weight of fuel, W_{fuel}, is not taken into account. The forces considered in the analysis include wing lift, L_W, and wing drag, D_W, which act at the aerodynamic center (x_{ac}, y_{ac}, z_{ac}). Additionally, the weight of the wing itself, W_{wing}, and the weight of components within the wing, such as the hydraulics (W_{hyd}), are also considered. Finally, the analysis also takes into account the pitching moment around the aerodynamic center.

Finally, using the vertical and the moment equilibrium, the structural loads acting on the wing root can be found as such :

$$
\begin{cases}
T_x = & \left(n \cdot \left(\frac{W_{\text{wing}}}{2} + \frac{W_{\text{hyd}}}{2}\right) - \frac{L_W}{2}\right) \cdot \sin(\alpha - i_w) + \frac{D_W}{2} \cdot \cos(\alpha - i_w) \\[2mm]
T_y = & 0 \\[2mm]
T_z = & -\left(n \cdot \left(\frac{W_{\text{wing}}}{2} + \frac{W_{\text{hyd}}}{2}\right) - \frac{L_W}{2}\right) \cdot \cos(\alpha - i_w) + \frac{D_W}{2} \cdot \sin(\alpha - i_w) \\[2mm]
M_x = & \left(n \cdot \left(\frac{W_{\text{wing}}}{2} \cdot y_{\text{cg}} + \frac{W_{\text{hyd}}}{2} \cdot y_{\text{hyd}}\right) - \frac{L_W}{2} \cdot y_{\text{ac}}\right) \cdot \cos(\alpha - i_w) - \frac{D_W}{2} \cdot y_{\text{ac}} \cdot \sin(\alpha - i_w) \\[2mm]
M_y = & \frac{1}{2} M_{\text{wing}} + \left(n \cdot \left(\frac{W_{\text{wing}}}{2} \cdot x_{\text{cg}} + \frac{W_{\text{hyd}}}{2} \cdot x_{\text{hyd}}\right) - \frac{L_W}{2} \cdot x_{\text{ac}}\right) \cdot \cos(\alpha - i_w) - \frac{D_W}{2} \cdot x_{\text{ac}} \cdot \sin(\alpha - i_w) \\[2mm]
M_z = & -\left(n \cdot \left(\frac{W_{\text{wing}}}{2} \cdot y_{\text{cg}} + \frac{W_{\text{hyd}}}{2} \cdot y_{\text{hyd}}\right) - \frac{L_W}{2} \cdot y_{\text{ac}}\right) \cdot \sin(\alpha - i_w) + \frac{D_W}{2} \cdot y_{\text{ac}} \cdot \cos(\alpha - i_w)
\end{cases}
$$

Table 6.15: Structural loads at the wing root section for the different critical flight conditions.

	A	B	C	D	E	F
T_x [$10^3 \cdot$ lbf]	-2.1168	-4.4572	-0.5966	0.4358	0.1036	-0.5393
T_y [$10^3 \cdot$ lbf]	0	0	0	0	0	0
T_z [$10^\cdot 3$ lbf]	7.7370	15.1636	8.6059	1.1171	-3.0911	-3.2713
M_x [$10^3 \cdot$ lbf.ft]	-37.6802	-73.6462	-45.4192	-10.8418	11.5011	14.1453
M_y [$10^3 \cdot$ lbf.ft]	-26.2956	-51.5409	-29.2360	-3.7734	10.5253	11.1324
M_z [$10^3 \cdot$ lbf.ft]	11.2177	23.2374	7.0963	2.3692	1.6738	3.2459

6.4.7. Structural design

The structural design is defined by an analysis carried out on the rear fuselage and at the wing root. In order to achieve this analysis, the rear fuselage's internal layout is composed of stringers and frames covered by a skin. As for the wing, the structure is similar constituting of stringers, spars and ribs with a skin coat. It is necessary to precise that both structures follow an idealized model where the stringers are modelized by booms carrying direct stress only while the skin carries shear stress.

6.4.8. Material

Aluminum 7075 alloy is assumed to be used for both the fuselage and wing skin. Moreover, for this analytical study, a safety factor s = 1.5 is considered to limit the admissible maximum direct and shear stresses, taking into account the tensile strength of Aluminum 7075, which is around $\sigma_y = 82650$ psi. By applying this safety factor, we can find the maximum tensile and shear stress that can be applied to the material without risking failure

$$\sigma_{max} = 55114 \text{ psi} \quad \text{and} \quad \tau_{max} = \frac{\tau_y}{s} = 31908 \text{ psi}$$
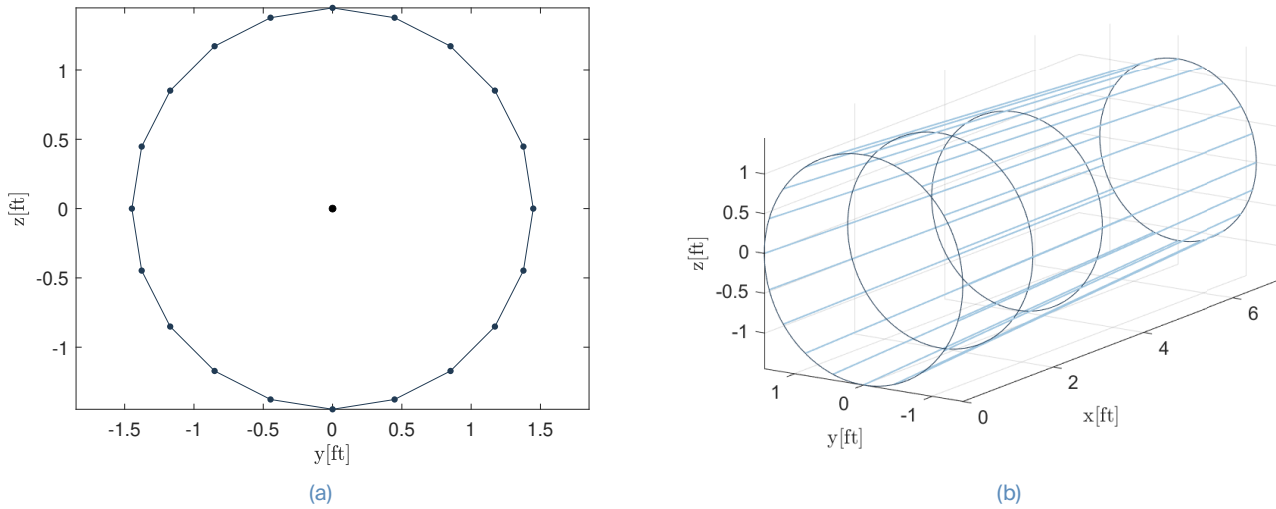
6.4.9. Rear fuselage

Figure 6.12: Representation of the idealized rear fuselage: (a) 2D representation of the fuselage cut located at the wing's trailing edge centered around the centroid indicated by a black dot. (b) 3D representation of the tapered wing.

The figure above highlights a rear fuselage that is composed of 20 stringers placed around circular frame. Due to this doubly symmetrical geometry of a rear fuselage cross section, the centroid can be found directly as the center of the circular section. Furthermore, it can be assumed that the stringers have the same cross section area B. The latter can be found by computing the direct stresses carried by each stringer. Therefore, it is necessary to compute the inertia per unit area which yields :

$$I_{\text{yy}}^i/B = \sum_j z_j^2 \quad ; \quad I_{\text{zz}}^i/B = \sum_j y_j^2 \quad ; \quad I_{\text{yz}}^i/B = 0 \text{ m}^2 \quad \text{by symmetry} \tag{6.19}$$

with (y_j, z_j) the coordinate of the jth boom with respect to the centroid located at the origin (0, 0).

At this point, it becomes possible to display the direct σ_{xx}^i carried by the stringer i. That leads to the equation of $B\,\sigma_{xx}^i$ which is more convenient for the study since it makes use of the inertia per unit area.

$$\sigma_{\text{xx}}^i = \frac{(I_{\text{zz}}\,M_y + I_{\text{yz}}\,M_z)\,z_i - (I_{\text{yz}}\,M_y + I_{\text{yy}}\,M_z)\,y_i}{I_{\text{yy}}\,I_{\text{zz}} - I_{\text{yz}}^2} \tag{6.20}$$

$$\Rightarrow B\,\sigma_{\text{xx}}^i = \frac{((I_{\text{zz}}/B)\,M_y + (I_{\text{yz}}/B)\,M_z)\,z_i - ((I_{\text{yz}}/B)\,M_y + (I_{\text{yy}}/B)\,M_z)\,y_i}{(I_{\text{yy}}/B)\,(I_{\text{zz}}/B) - (I_{\text{yz}}/B)^2}$$

The minimal cross-section area of the stringers is obtained by ensuring that the direct stresses do not exceed the maximum allowable stress such that $\| B\,\sigma_{\text{xx}}^i \| \leq B\,\sigma_{\text{max}}$. Therefore B_{min} can be retrieved with the following formula : $B_{\text{min}} = \max(\| B\,\sigma_{\text{xx}}^i \|)/\sigma_{\text{max}}$

The considered area $B_{\min}$ can then be computed for the critical points of the flight envelope. Finally, a minimum area of 0.0208 in² is found for the critical case **C**.

Skin thickness

The rear fuselage skin thickness required to withstand shear flow results from lateral and vertical shear loads, respectively T_y and T_z, along the M_x torque. Therefore, for a considered section j, the shear flow of the panel $i + 1$ can be decomposed into three contributions which are respectively the shear flow due to T_y, the shear flow due to T_z and the shear flow due to torque M_x. When the contributions are added together it yields :

$$q = q^i - \frac{T_y}{I_{zz}^j}\, y_j - \frac{T_y}{I_{zz}^j}\, y_j + \frac{M_x}{2\pi D_j^2/4}$$

One can notice that the equations are simplified due to the symmetry of the problem which translates to the inertia I_{yz}^j being null.

The minimum thickness of the skin can be determined by examining the section that contains the panel with the highest shear flow, which is considered to be the critical case.

$$t_{min} = \frac{q}{\tau_{\max}} = 0.0032 \text{ in}$$

We also observe that this corresponds to critical case B, which is the same critical case as for the minimal beam area.

Now, a finite element analysis can be performed in order to assess the results of the analytical structural analysis. The Finite element analysis is carried out on the NX software. The analysis uses 1D and 2D elements that have been affected by virtual thickness in order to accelerate computational time. Furthermore, as the case **C** has been identified throughout the analytical process as the most critical flight envelope point, it will be studied for the computation on NX. Furthermore, The fuselage cut located at the wing's trailing edge will be treated as clamped with respect to the boundary conditions. As for the loads, we consider the self-weights of the fuselage, engine, and tails, as well as the force applied at the aerodynamic center of the tail.

The sizing of the structural elements of the rear fuselage has been given by the analytical studies and it yields :

0.12 in

0.06 inc

0.2 in

0.12 in

Figure 6.13: Geometry of the fuselage stringers.
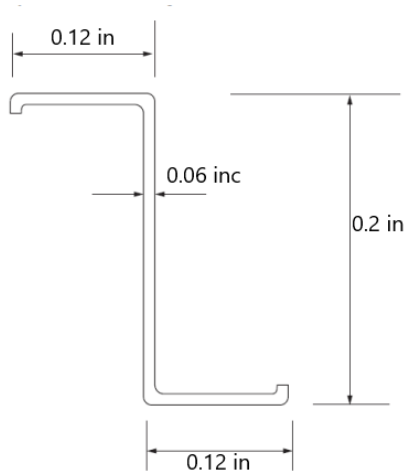
Table 6.16: Sizing of the finite element model of the rear fuselage.

Components	Thickness/Area	Quantity
Skin	0.0032 [in]	-
Frames	0.2635 [in^2]	11
Stringers	0.0208 [in^2]	39

It leads to the figures 6.14 accounting for the deflection of the rear fuselage and the direct and shear stresses.

(a) Displacement field of the fuselage for critical flight condition **C**.

(b) Bending stress distribution of the fuselage for critical flight condition **C**.

(c) Shear stress distribution of the fuselage for critical flight condition **C**.

Figure 6.14

One can, now, analyze the Von-Mises stress along the rear fuselage. It shows that the maximum Von-Mises stress is obtained at the cut of the rear fuselage. Furthermore, it can the noticed that the upper part of the fuselage is in tension while the lower part is compressed. This accurately depicts the

physical behavior of the fuselage. Indeed, since the tail produces a downward lift, the lever arm will induce a moment that will compres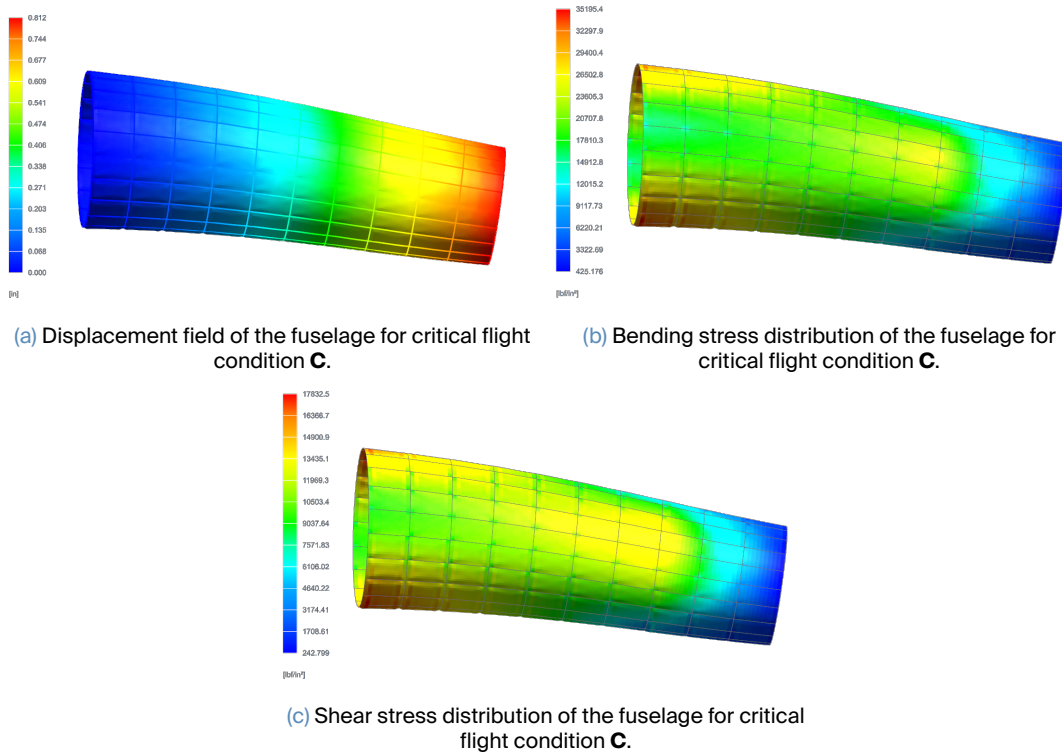s the lower part. Moreover, it can be noticed that the shear stress of the material is not exceeded. Therefore, the material is safe from being damaged.

It can be seen that the values of direct and shear stress have been overestimated by the analytical analysis. This is directly due to the assumption that the booms only carry direct stress while the skin panels carry shear stresses. In addition, the maximum deflection of the fuselage seems acceptable since it only constitutes a small percentage of the rear fuselage length. Finally, in both methods, the maximum direct and shear stress is in the range of the material used. It confirms that the boom section and the skin thickness, coupled with resistant material, ensure a reliable structure.

Table 6.17: Comparison of the maximum direct and shear stresses on the fuselage section.

	Max. deflection [in]	$\max\left(\|\sigma_{xx}\|\right)$ [lbf/in²]	$\max\left(\|\tau_{xy}\|\right)$ [lbf/in²]
Analytical	-	55114	31908
NX	0.812	35195	17832.5

6.4.10. Wing root section

Boom area
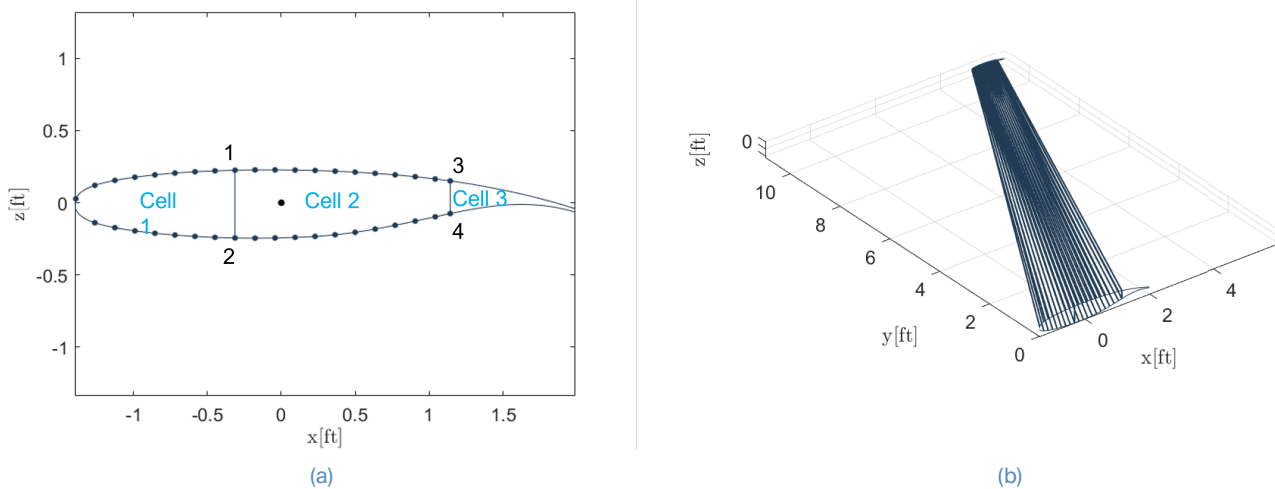
Figure 6.15: Representation of the idealized wing: (a) 2D representation of the root cross-section centered around the centroid indicated by a black dot. (b) 3D representation of the tapered wing.

As mentioned earlier, the wing consists of three cells, comprising of two spars and $n = 39$ evenly spaced stringers distributed around the two cells. No structural reinforcement has been accounted for the third cell since it contains the control surfaces. Furthermore, the spars are delimiting the cells.

Similarly to the rear fuselage, the stringers of the wing can be supposed to possess the same cross section area B. But in the absence of any symmetry, the centroid location of wing root section (x_C, 0, z_C) need to be computed and it yields :

$$x_C = \frac{\sum_j B_j\, x_j}{\sum_j B_j} = \frac{\sum_j x_j}{n} \quad \text{and} \quad z_C = \frac{\sum_j B_j\, z_j}{\sum_j B_j} = \frac{\sum_j z_j}{n} \tag{6.21}$$

One can then compute the inertia per unit area of the wing root section in order to find the direct stress σ_{yy}^i carried by the stringer i and, by extension, the value of $B\,\sigma_{yy}^i$

$$\sigma_{yy}^i = \frac{(I_{zz}\, M_x + I_{xz}\, M_z)\,(z_i - z_C) - (I_{xz}\, M_x + I_{xx}\, M_z)\,(x_i - x_C)}{I_{xx}\, I_{zz} - I_{xz}^2}$$
$$\Rightarrow B\,\sigma_{yy}^i = \frac{((I_{zz}/B)\, M_x + (I_{xz}/B)\, M_z)\,(z_i - z_C) - ((I_{xz}/B)\, M_x + (I_{xx}/B)\, M_z)\,(x_i - x_C)}{(I_{xx}/B)\,(I_{zz}/B) - (I_{xz}/B)^2} \tag{6.22}$$

In the same way as for the rear fuselage, the minimal cross-section area of the stringers is such that the direct stress does not exceed the maximum allowable direct stress. And as expected the case **B** of the envelope points leads to $B_{\text{min}} = 0.2171\ \text{in}^2$. Therefore each stringer will have the same cross-section area $B = B_{\text{min}}$.

Skin thickness

The skin thickness can be computed considering the total shear flow through the wing root section. But, first, one must determine the open shear flow that writes as :

$$q_0(s) = -\frac{I_{zz}\, T_z^{\text{web}} - I_{xz}\, T_x^{\text{web}}}{I_{xx}\, I_{zz} - I_{xz}^2}\left[\sum_{i:s_i \leq s} z_i\, B\right] - \frac{I_{xx}\, T_x^{\text{web}} - I_{xz}\, T_z^{\text{web}}}{I_{xx}\, I_{zz} - I_{xz}^2}\left[\sum_{i:s_i \leq s} x_i\, B\right] \tag{6.23}$$

with,

- the web loading :

$$\begin{cases} T_x^{\text{web}} = T_x - \sum_i P_y^i\, \frac{\delta x^i}{\delta y} \\[2mm] T_z^{\text{web}} = T_z - \sum_i P_y^i\, \frac{\delta z^i}{\delta y} \end{cases} \tag{6.24}$$

- P_y^i, the loading in boom i which is obtained by assuming that the load follows the boom direction. Therefore, in the scope of this study, $P_y^i = \sigma_{yy}^i\, B$

- $\frac{\delta x^i}{\delta y}$ and $\frac{\delta z^i}{\delta y}$ represent the tapering of the wing.

The process of computing the wing skin thickness can be summarized trough two major steps. At first, it needs to be computed the open shear flow on each cell then it will be applied a correction which allow to retrieve the result.
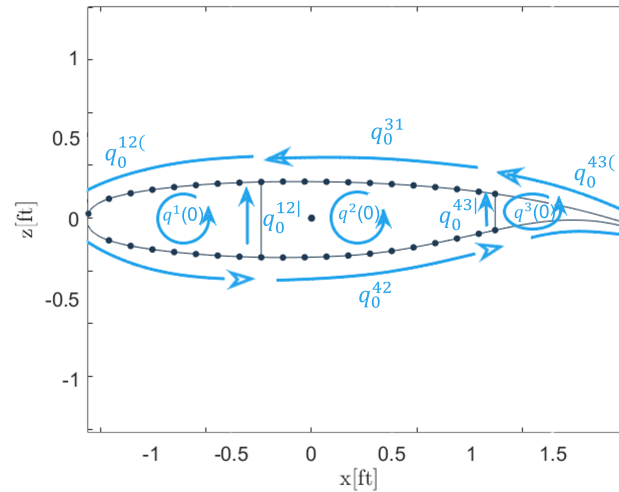

Figure 6.16: Visualization of the open shear flow and the corrected shear flow on each cell.

And, therefore, it is possible to retrieve to minimum thickness of the skin for each point of the flight envelope. The minimum thickness obtained is $t_{min} = 0.0954$ in. Once again, it can be observed that this situation aligns with critical case **B**, which happens to be identical to the critical case for the minimal beam area.

By noticing the symmetry of the wing, only the half-wing can be used for the Finite element analysis. Therefore, it implies that half the loads are taken while a fixed constraint is considered at the wing root cut. For the structural parts, the stringers and the ribs are modeled as 1D elements with virtual section areas. In the meanwhile, the skin of the wing and the web of the spar are modeled as 2D elements with a virtual thickness. The CAD model will be used for the rear fuselage is illustrated in Fig. 6.17. We assume that the wing root is fixed in terms of boundary conditions. In regards to the loads, we include the weight of the fuselage and hydraulics, as well as the lift and drag forces, which are modeled by applying a pressure differential on the surface of the wing. Finally, since the analytical procedure has identified case **B** as the most critical flight envelope point for the wing, it will be specifically examined in the NX computation.
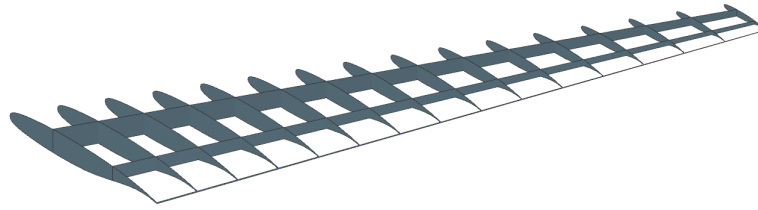
Figure 6.17: Internal structure of the wing which consists of ribs and spars.

The sizing of the structural elements of the wing has been given by the analytical studies and it yields:
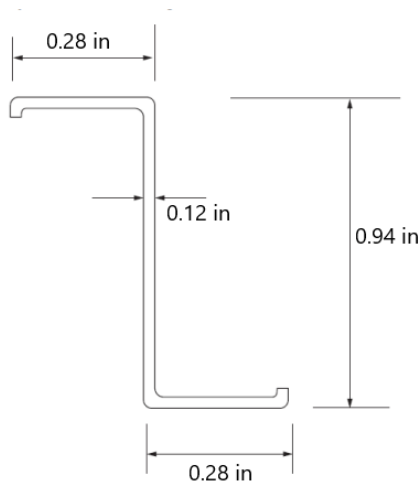

Figure 6.18: Geometry of the wing stringers.

Table 6.18: Sizing of the finite element model of the wing.

Components	Thickness/Area	Quantity
Skin	0.0954 [in]	-
Ribs	0.0954 [in]	16
Spars	0.0954 [in]	2
Stringers	0.2171 [in^2]	39

It leads to Figs. 6.19 accounting for the deflection of the rear fuselage and the direct and shear stresses. The maximal deflection of the wing is equal to 18.93 inches and it happens at the wing tip. As excepted, the deflection of the wing is such that the upper section of the wing root is compressed while the lower section is in tension.

Finally, it can be analyzed the maximum direct and shear stress of the structure. Similarly to the fuselage, the direct and shear stresses of the wing also highlight differences. It is primarily due to the hypotheses made on the stress distribution on the stringers and on the skin. Furthermore, while the lift and drag are applied on one point in the analytical study, they result from a pressure distribution in the finite element analysis. One more reason can be that, in the analytical process, the third cell of the wing is not taken into account which affects the stress distribution. Nevertheless, the values of direct and shear stresses do not exceed the maximum allowable stresses of the material which validate the structural parameter choice for the wing.

(a) Displacement field of the wing for critical flight condition **B**.

(b) Bending stress distribution of the wing for critical flight condition **B**.

(c) Shear stress distribution of the wing for critical flight condition **B**.
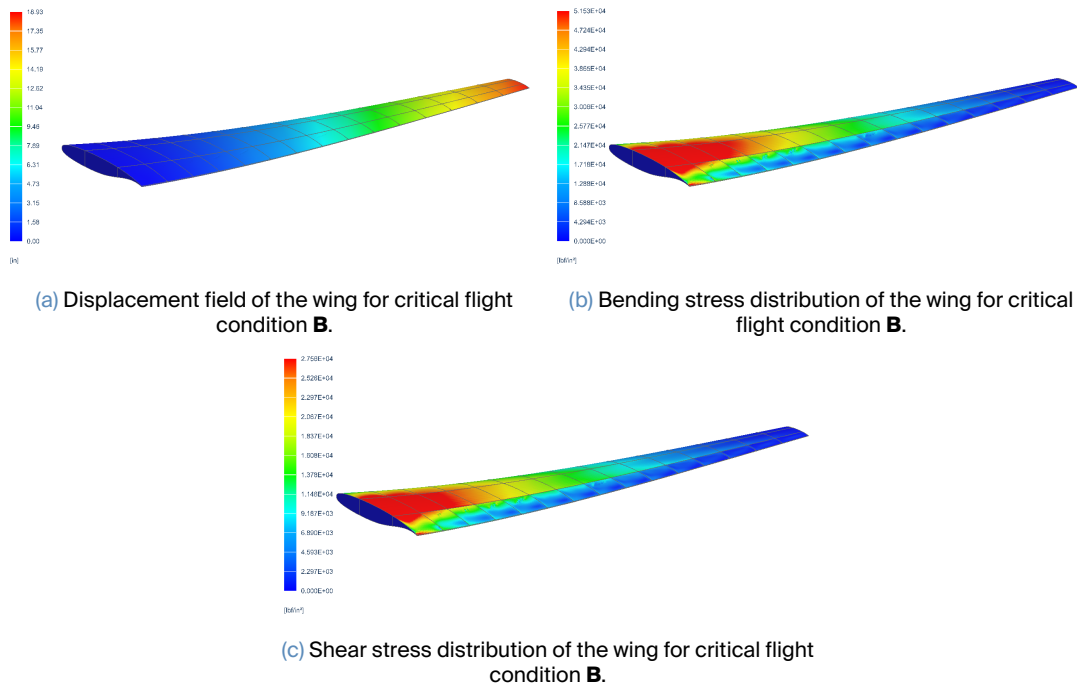
Figure 6.19

Table 6.19: Comparison of the maximum direct and shear stresses on the wing root section.

	Max. deflection [in]	$\max(\|\sigma_{xx}\|)$ [lbf/in^2]	$\max(\|\tau_{xy}\|)$ [lbf/in^2]
Analytical	-	55114	31908
NX	18.93	51530	27560

6.5. Performance Analysis

The methodology presented by Gudmundsson [16] is used to compute the performance analysis of RADAR for each flight phase in this section.

6.5.1. Range analysis

The Request for proposal requires a long ferry divided into three flight phases for the main mission:

- Cruise ingress range: 850 nm at Mach 0.86,

- Loiter time: 5h at Mach 0.7,

- Cruise egress range: 2000 nm at Mach 0.86.

The design of the aircraft is precisely aimed at meeting these ranges. According to 14 CFR Part 23 regulations [35], it is mandatory to include additional fuel for the purpose of safety in case the aircraft

needs to land at an alternate airport nearby. An additional loiter of 45min is available after attempting to land at the intended destination. The mission and reserve requirements are synthesized in Figure 6.20. The second and third missions are additionally outlined with the objective of optimizing loiter and range, correspondingly. Let us prioritize the primary mission and concentrate on it initially. The Breguet range and endurance equations are simplified assuming constant airspeed and attitude cruise/loiter, i.e.

$$R = \int_{W_i}^{W_f} \frac{V}{gSFC}\frac{C_L}{C_D}\frac{1}{W}dW = \frac{V}{gSFC}\frac{C_L}{C_D}\ln\frac{W_i}{W_i - W_{fuel}},$$
$$E = \int_{W_i}^{W_f} \frac{1}{gSFC}\frac{C_L}{C_D}\frac{1}{W}dW = \frac{1}{gSFC}\frac{C_L}{C_D}\ln\frac{W_i}{W_i - W_{fuel}}.$$
(6.25)

and evaluated for previously described phases at an altitude of 30,000 ft. The average lift and drag coefficients throughout the entire cruising segments can be considered as the values that would be obtained for the scenario of carrying a full payload with half fuel burned. Figure 6.20a displays the computed cruise range and endurance based on the various parameters available. The computations are performed in the worst case for the payload, i.e. no drop during the flight. Note that the aircraft has been designed for the objectives but the drag analysis reveals that the drag increases with respect to the parabolic drag assumption. This is mostly explained by the downward lift produced by the horizontal tail. The fuel weights have been reorganized to prioritize ingress and loiter, as they are the most interesting for the mission.

(a) Principal mission.

(b) Secondary missions.
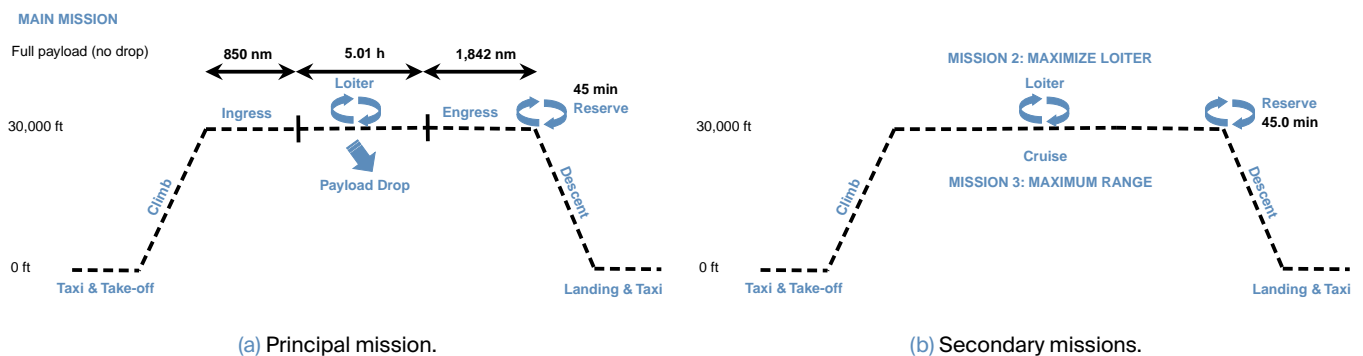
Figure 6.20: Description of primary and secondary missions. The performance of the aircraft for the main mission (ingress-loiter-egress) is displayed above.

To analyze the secondary missions, payload range diagrams will be utilized since both missions are performed at a constant speed. The repartition of the fuel consumption during the main mission is further detailed in section 6.5.2. The fuel tanks have been designed for the main mission, i.e. no

additional fuel can be added.

The payload-range diagrams for cruising at two different speeds are presented in Figure 6.21. These diagrams demonstrate how the maximum range changes as the payload varies. The ranges presented were computed using Eq. 6.25, where the lift-to-drag ratio was evaluated at half of the maximum fuel weight. The ferry ranges, which are the ranges at no payload, were calculated by deducting a fraction of the payload weight from the total weight. The ferry ranges that have been calculated are as follows: for the Mach 0.86 cruise, the range is 5164 nautical miles, while for the Mach 0.7 cruise, the range is 6401 nautical miles, which corresponds to 15.5 hours of endurance. At the maximum takeoff weight, the range for the Mach 0.86 cruise is 4701 nautical miles, while for the Mach 0.7 cruise, the range is 5855 nautical miles, which corresponds to 14.2 hours of endurance. The reserve fuel refers to the amount required to fly for 45 minutes. The maximum takeoff weight equals 5717 lbs.

(a) Maximum loiter at $M = 0.7$.

(b) Maximum range at $M = 0.86$.
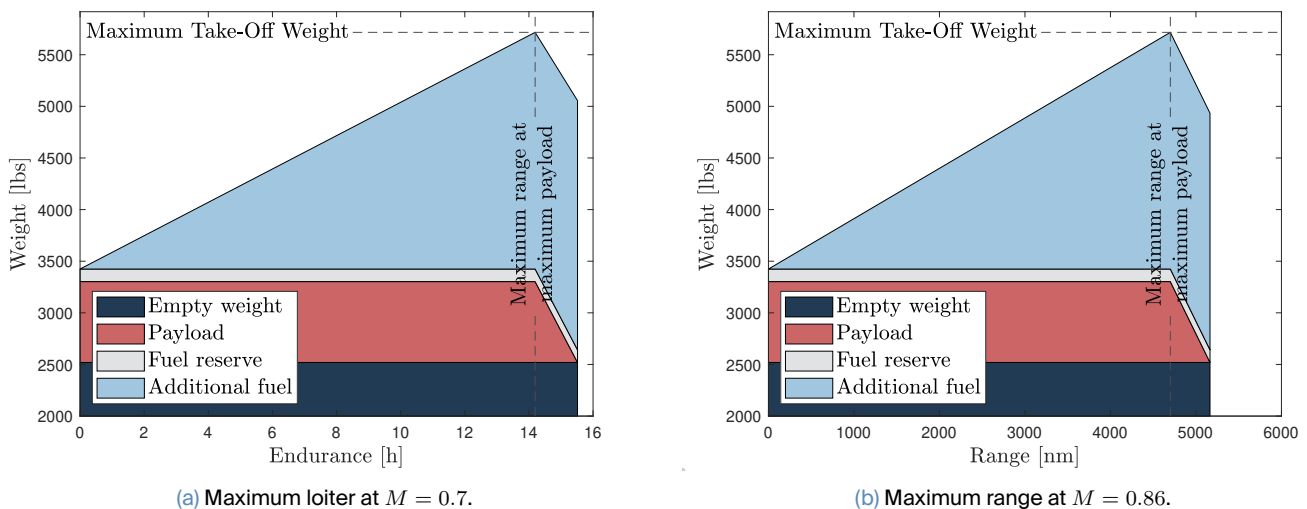
Figure 6.21: Payload range diagram for loiter and cruise speeds at 30,000 ft.

6.5.2. Fuel analysis

This section details the calculation of the total mass of fuel required for the specified mission. The Williams FJ33-5A engine uses kerosene. The fuel masses required for ingress, loiter, egress, and reserve are computed using the range equation, i.e. Eq. 6.25. The fuel consumption of secondary phases has been determined with approximations according to the course *Conceptual Design* [28]. The taxi and takeoff fuel weight is estimated to be 0.35 % of the total weight. The same approximation was used for the taxi and landing fuel weight. The takeoff and taxi fuel weight is relatively small compared to common airplanes. As the RADAR aircraft is a small aircraft, engine warm-up was neglected. The

climb weight approximation is determined using:

$$W_{\text{climb}} = \frac{1}{100}\left(\frac{\text{cruise altitude [ft]}}{31600\text{[ft]}} + \frac{1}{2}M_{\text{cruise}}^2\right)W_{\text{TO}}. \tag{6.26}$$

The total mass of fuel is $m_{\text{fuel}} = 2414$ lbs. As explained, the fuel tanks are designed for the primary mission. The fuel mass build-up is depicted in Figure 6.22.
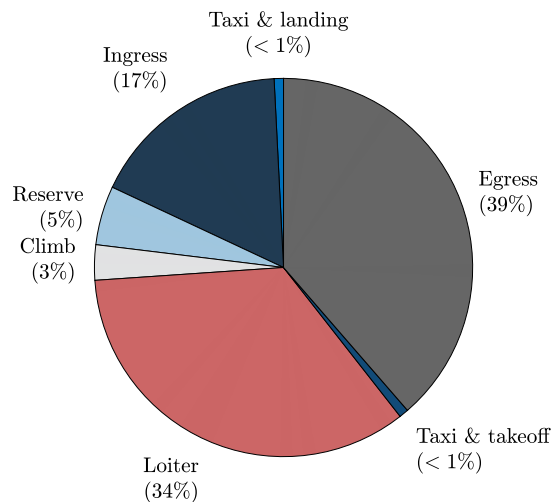
Figure 6.22: Repartition of the fuel consumption.

The fuel flow rate of an airport fuel pump can vary depending on the type of pump, the size of the airport, and other factors. However, the typical fuel flow rates range from 200 to 600 gallons per minute (GPM) [36]. The total fuel capacity of the aircraft is 352 gallons. Thus, assuming a fuel flow rate of 200 GPM. The maximum total refuel time is 1.76 minutes.

6.5.3. Take-off/landing distances

A determining parameter in the take-off and landing distances is the stall speed. The smaller the stall speed the shorter the take-off distance. The stall speed in landing and take-off is computed by considering the maximum lift coefficient of the wings. In the take-off and landing conditions, the maximum lift coefficient is increased by the use of high-lift devices and these devices have been determined using section 5.1.2. According to Raymer [14], the stall speed in takeoff and landing configuration can be computed based on the maximum lift coefficient with high-lift devices (cf. section 5.1.2). These stall speeds are equal to 117 kts for takeoff and 84 kts for landing.

Take-off

Figure 6.23 illustrates the various take-off segments, which have been identified as:

- Acceleration from the release of the brakes to lift-off speed, considering 1 second free roll time.

- Transition and climb to an obstacle clearance of 30 ft.

Figure 6.23: Take-off distances at sea-level conditions for wet and dry concrete runway. Gudmundsson's reference book [16] provides the ranges of ground roll friction coefficients for 'brakes off' configuration on various surface types. The airspeeds for ground run, lift-off, transition, and climb are defined by the 14 CFR Part 23 [35].

The lift of the aircraft is increased by deflecting plain flaps at 20°. The ground run acceleration on a flat runway is

$$a = \frac{g}{W}(T - D - \mu(W - L)),$$ (6.27)

where the thrust is the maximum thrust developed at sea level. The ground run distance is simply deduced $S = V^2/2a$. Note that the induced drag must be corrected for ground effect. The drag for the ground run D takes into account the added drag due to flaps and the correction of the induced drag for ground effect. The take-off distance at sea level are computed for different braking ground friction coefficients in Figure 6.23. The aircraft was designed with only one engine, so it does not require the same assessment as aircraft with multiple engines when determining the take-off distance in the event of an engine failure.

Landing

As illustrated in Figure 6.24, the landing distance is decomposed in multiple phases:

- Unpowered approach phase at an angle of 3° starting from 30 ft clearance obstacle to the flare height.

- Flare stage from the flare height to touchdown.

- 1 second roll time before applying the braking systems.

- Braking from touchdown speed to a complete stop.
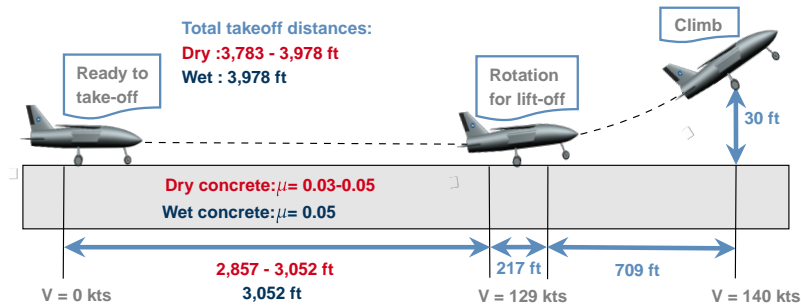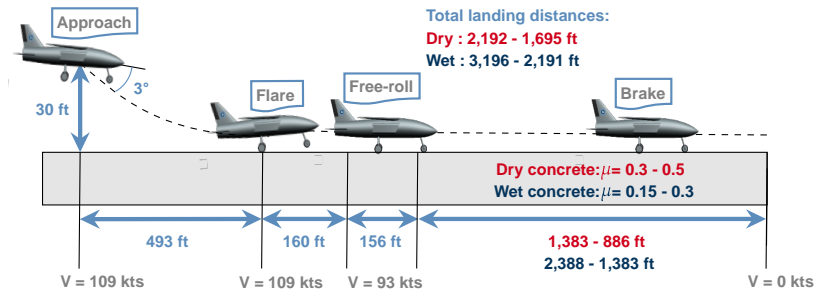

Figure 6.24: Landing distances at sea-level conditions for wet and dry concrete runway. Gudmundsson's reference book [16] provides the ranges of ground roll friction coefficients for 'braking' configuration on various surface types. The airspeeds for approach, flare, touch-down and braking are defined by the 14 CFR Part 23.

The lift of the aircraft is increased by deflecting plain flaps at 60°. The braking deceleration on a downhill slope γ is

$$a = \frac{g}{W}(T - D_{\mathsf{ldg}} - \mu(W - L) + W\sin\gamma), \tag{6.28}$$

which, in our case, simplifies for a flat runway ($\gamma = 0$). The distance is simply deduced $S = V^2/2a$. Assuming no thrust reverser, the thrust is small during landing and considered negligible here. The drag after touchdown D_{ldg} takes into account the added drag due to flaps and the correction of the induced drag for ground effect. The landing distance at sea level is computed for different braking ground friction coefficients in Figure 6.24.

Altitude sensitivity

High altitude airports have lower air density, making it harder for aircraft to generate lift, requiring a longer runway for takeoff and landing. The reduced engine performance at higher altitudes can also add to this challenge, necessitating longer runways to ensure safe operations.

The sensitivity of the runway distances to altitude and surface type is presented in Figure 6.25. It can be seen that the altitude deviation results in larger changes in takeoff over a 30 ft obstacle, when compared to landing. Furthermore, it should be noted that the coefficient of friction exhibits significant variation depending on the landing surface type.

(a) Take-off runway.

(b) Landing runway.
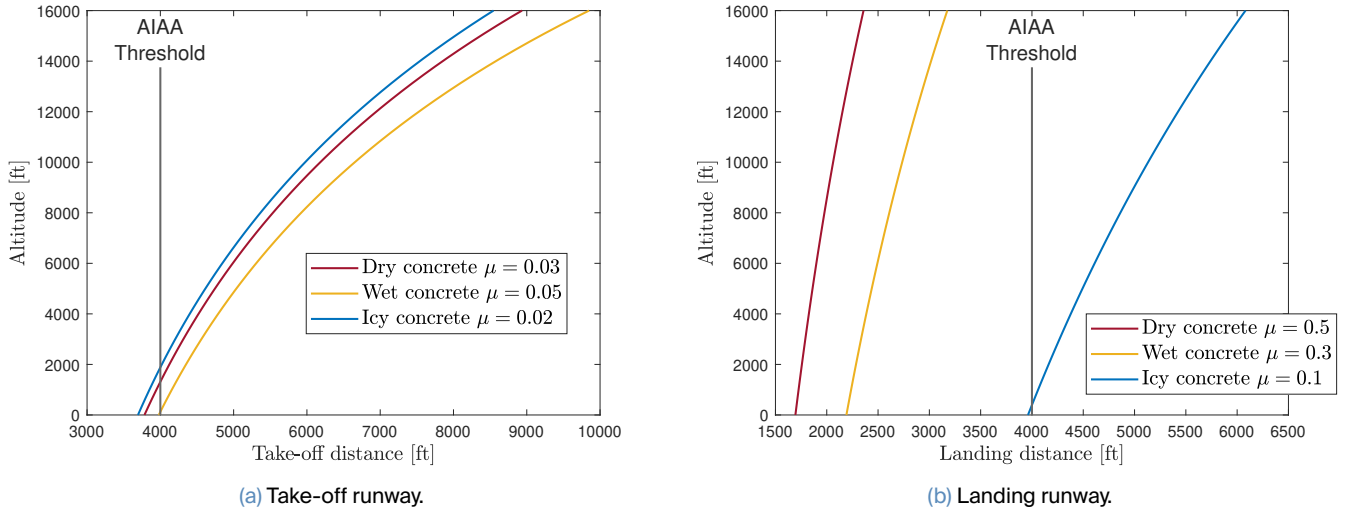
Figure 6.25: Sensitivity study showing the effect of altitude and ground friction coefficient on the take-off and landing distances. Gudmundsson's reference book [16] provides the ranges of ground roll friction coefficients for both 'brakes off' and 'braking' configurations on various surface types.

6.5.4. Dash speed

The dash speed is the maximum velocity at which the airplane can fly in desired flight conditions. In other words, this is the speed reached when the engine generates its maximum power. In steady flight conditions,

$$D = \frac{1}{2}\rho_\infty V_\infty^2 S C_D = T, \qquad (6.29)$$

and the maximum velocity in level flight is mostly controlled by the maximum thrust available. The RADAR's weight varies during the flight as the fuel is consumed, inducing changes in lift produced and so the drag also changes.

Throughout the mission, i.e. flying at 30000 [ft], the dash speed (Mach) reached by the Williams FJ33-5A engine is represented in Table 6.20. The sequential phases of the aircraft's mission can be denoted as A, C, and E, which correspond to the beginning of ingress, loiter, and egress, respectively. Furthermore, phases B, D, and F indicate the respective aircraft configurations when half of the fuel from the ingress, loiter, and egress phases have been depleted. The variability in the relative increase of the

Table 6.20: The progression of the aircraft's attainable maximum speed during the course of its mission.

	A	B	C	D	E	F
Mach dash [-]	0.9218	0.9251	0.9276	0.9312	0.9331	0.9334

maximum Mach number across different phases is attributed to variations in the fuel burned between

(a) Rate of climb.   (b) Climb angle.
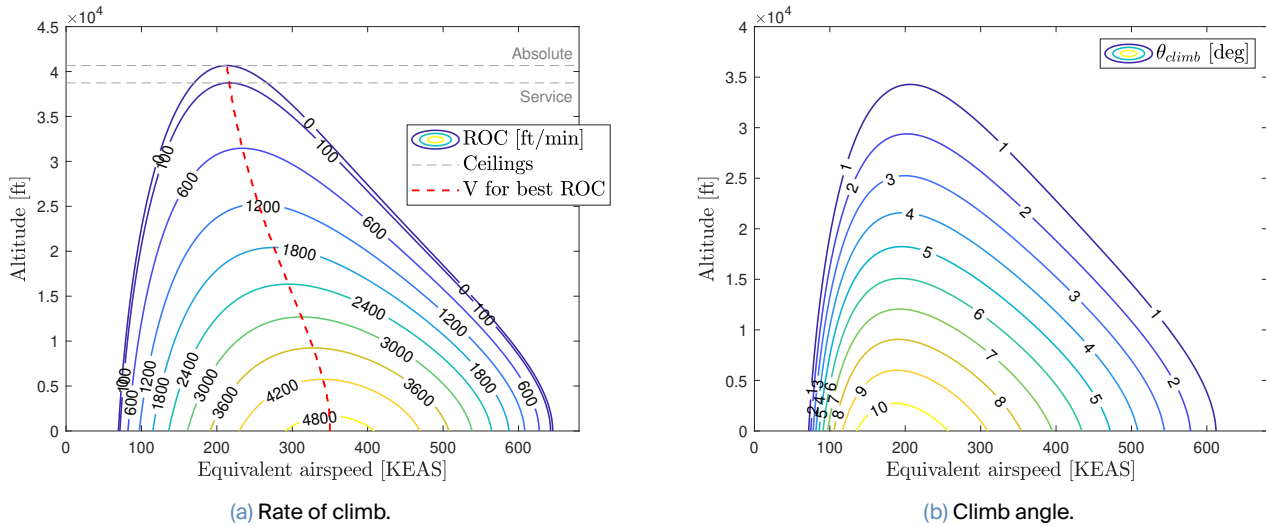
Figure 6.26: Representation of (a) the achievable rate of climb and (b) the angle of climb.

each phase. A discernible trend is observed wherein the engine encounters increasing difficulty in augmenting the aircraft's velocity at higher Mach numbers.

6.5.5. Climb

In this section, the climbing performance of the RADAR aircraft is evaluated. The climb angle θ is obtained from the force balance of the aircraft during climb:

$$
\left.\begin{array}{l}
L = W \sin\theta \\
T = D + W \sin\theta
\end{array}\right\} \Rightarrow \theta = \arcsin\left(\frac{T-D}{W}\right),
$$

where the maximum available thrust is computed based on the thrust relation [21], explained in the propulsion section 5.3, and the total drag force is evaluated under the assumption of a quadratic drag model. The equations of motion are adapted to a steady climbing flight. The airplane's climb capabilities can be evaluated using the Rate of Climb (ROC) indicator, which is an excellent measure and computed in this way

$$
ROC = V\sin\theta = \frac{TV - DV}{W}. \tag{6.30}
$$

The Figure 6.26 presented below illustrate the relationship between the climb angle and the climb rate, considering both altitude and speed.

The time required to reach the target altitude $h = 30,000$ ft from the sea level is determined from the following expression

$$t_{\text{climb}} = \int_0^h \frac{dh}{\text{ROC}} \tag{6.31}$$

and the horizontal distance covered during the climb can be obtained with

$$x_{\text{climb}} = \int_0^{t_{\text{climb}}} \frac{\text{ROC}(h)}{\tan \theta_{\text{climb}}} dt. \tag{6.32}$$

According to S. Gudmundsson [16], if a specific velocity, such as the airspeed for best ROC at sea level, is sustained during ascent, the rate of climb (ROC) will decline in a manner that is approximately linear. By conducting numerical integration through the decomposition of ascent into short, piecewise linear segments, we can then determine the time and distance required to complete the climb. Another approach is to consider the velocity corresponding to the best ROC at the different altitudes. Essential attributes of the climb are listed in Tables 6.21 and 6.22.

Table 6.21: Key climb performance parameters at sea level.

Parameter	Value
Best ROC at sea level [ft/min]	4,990
Airspeed for best ROC at sea level [KEAS]	350
Climb angle for best ROC at sea level [deg]	2.9
Best climb angle at sea level [°]	10.7
Airspeed for best climb angle at sea level [KEAS]	184
ROC for best climb angle at sea level [ft/min]	3,464
Computed absolute ceiling [ft]	40,666
Computed service ceiling [ft]	38,735

When evaluating a constant velocity, the rate of ascent utilized is suboptimal. As demonstrated in Figure 6.26, the rate of ascent near 30,000 ft is significantly lower when comparing the airspeed for the best ROC at sea level, V_Y, with the speed at which the best rate of ascent is achieved at these altitudes. This phenomenon can be attributed to the engine operating near its maximum thrust, resulting in difficulty accelerating for the ascent. The reason for the significant time discrepancy between the two climb periods shown in Table 6.22 can be attributed to the former reason. The climb duration is relatively high but no requirements were imposed on the climb. Therefore, it's possible that the weight of fuel is underestimated.

Table 6.22: The time and horizontal distance required to climb to an altitude of 30,000 ft.

	Constant speed V_Y	Optimal speed
Time to altitude of 30,000 ft [min]	22	15
Horizontal distance covered during climb [nm]	127	87

6.5.6. Descent

The descent can be done at multiple speeds. The most common method is maintaining the cruising speed and reducing thrust to achieve acceptable descent rates. Since there are no humans on board the aircraft, high initial descent rates (e.g. 5,000 ft/min) can be considered, and then reducing them during the landing phase (below 4,000 ft according to the SKYbrary Aviation Safety website [37]). To achieve the landing speed and slope specified in the landing performance section (see 6.5.3), the estimated rate of descent during the landing phase is 580 feet per minute. The descent distance and time are 39 nm and 11.3 min, respectively.

6.5.7. Turn

This section intends to analyze the general level constant-velocity turn. To maintain a stable altitude without slipping or skidding, an airplane must generate a lift that equals its weight while also producing a centripetal force that counteracts the centrifugal force. The set of equations describing the motion of the airplane in the turn conditions is written as follows:

$$T - D = 0$$
$$L \cos \phi - W = 0 \tag{6.33}$$
$$L \sin \phi - \frac{W}{g} \frac{V^2}{R_{\text{turn}}} = 0$$

where ϕ is the bank angle, i.e. the angle between the lift and the horizontal direction.

Figure 6.27 illustrates how the aircraft can turn at specific airspeeds. As the aircraft executes a turn, the load factor rises in direct proportion to the turn rate, influenced by the aircraft's physical characteristics, including its speed and radius of gyration.
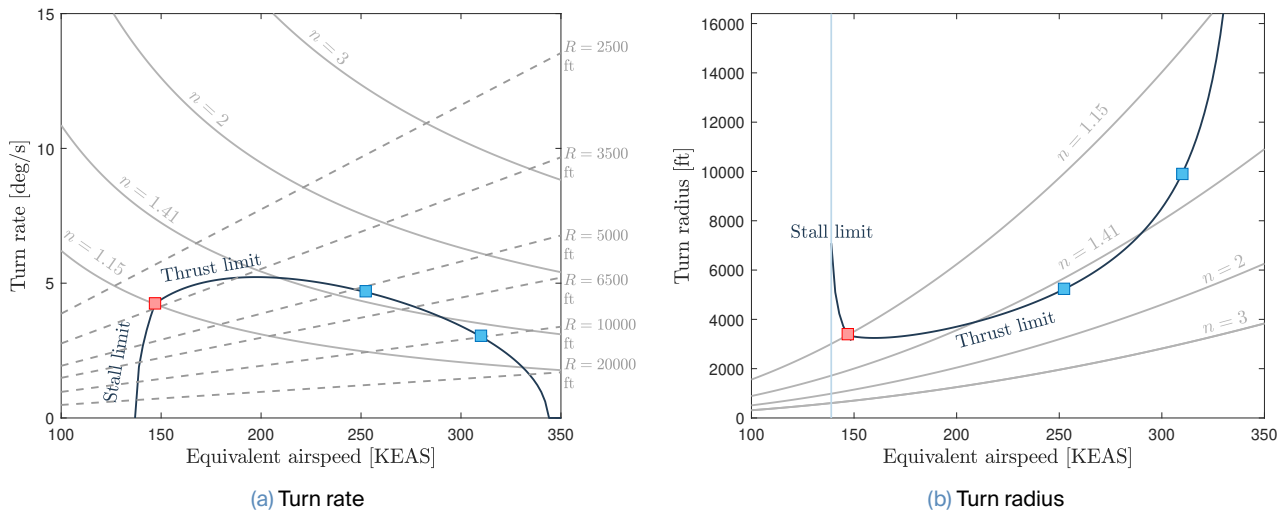
(a) Turn rate

(b) Turn radius

Figure 6.27: Turn performance maps at cruise altitude (30,000 ft). The blue line depicts the boundary created by the thrust and stall limitations. The red box represents the corner speed, while the blue boxes indicate the ingress/egress and loiter speeds. The gray dotted lines on the graph located on the left signify constant turning radii in feet, while the gray straight lines represent the constant load factors. A bank angle of 30° and 45° corresponds to load factors of 1.15 and 1.41, respectively.

The performance maps show that aircraft turning capabilities are limited by the stall velocity and the maximum thrust provided by the engine in function of the airspeed. The progression of stall and maximum thrust limits is defined by an increase in turning rate at a constant velocity, which subsequently results in an increase in the load factor. The increased load factor causes an escalation in drag, which reduces the range of acceptable velocities as the aircraft attains higher turn rates and load factors. The admissible velocity range is restricted not by the structural capabilities of the aircraft, but by its turning capacity at a constant altitude. If the turn rate or turn radius fall outside the permissible values for a constant level and velocity turn, the aircraft will experience a loss of altitude during the turn.

At cruising conditions, defined as an equivalent speed of 310 knots for ingress/egress and 252 knots for loiter, the RADAR aircraft demonstrates the capability to perform a turn at a constant speed without any change in altitude. Table 6.23 presents the maximum achievable turning rate, corresponding bank angle, load factor, and turn radius of the aircraft. The maneuverability of the aircraft is limited due to the small wing and thrust.

Table 6.23: Cruise turn performance. The calculations were done at cruise altitude (30,000 ft) and using the maximum thrust that the engine can produce at the respective cruise velocities. The values presented below are derived from the equivalent ingress/egress and loiter speeds obtained from Figure 6.27.

	Loiter	Ingress/Egress
Maximum turn rate [°/s]	4.7	3.1
Maximum load factor [-]	1.47	1.32
Maximum bank angle [°]	47	41
Minimum turn radius [ft]	5,240	9,780

6.5.8. Glide

In the event of engine failure resulting in the inoperability of the single-engine, the ability of an aircraft to glide safely to the nearest airport is of critical importance. This section evaluates the calculation of the aircraft's glide range and sink rate from its cruising altitude to the ground. The weight of the aircraft is taken into account for each segment of the mission when half of the mission's fuel has been consumed. The drag increment due to the engine failure has been previously detailed in the section 6.3.1.

Table 6.24: Glide performance evaluated at the middle of each phase.

	Flight phases		
	Ingress	Loiter	Egress
Best glide speed [KEAS]	183	168	157
L/D_{max} [-]	13.5	12.8	13.7
Minimum Angle-of-descent [deg]	4.2	4.4	4.2
Glide distance [nm]	67	63	68
Rate of descent [ft/min]	1,370	1,323	1,159

7 Trade off study

It can be demonstrated the impact of the primary design factors on additional parameters in this section. These baseline values will increase or decrease by ten percent to illustrate the variance. It is compared with the obtained variation values to better comprehend a configuration or the chosen optimal parameter. Aspect ratio, cL reference value and Mach numbers will be the key modified parameters. For values that have changed by more than (5%), the negative impact is highlighted in red, while the positive impact is highlighted in green.

7.1. C_L impact

The wing area (S_{ref}) is calculated based on the lift coefficient (c_L), assuming that the total lift is provided by the wing and cL reference value is an initial guess. The effect of the C_L value taken as a reference on other values is shown in Table 7.1. The reference C_L value is set to 0.30, 0.35, 0.40 and 0.50 and its effects on other variables are examined. Increasing the cL value is directly proportional to the increase in the lift produced, but the total drag created by the 3-D wing effect also increases.

Table 7.1: Lift coefficient impact on other variables.

	$C_L = 0.30$	$C_L = 0.35$	$C_L = 0.40$	$C_L = 0.50$
$(C_L/C_D)\big|_{\text{Ingress}}$ [-]	-3.29 %	**13.84**	2.45 %	5.56 %
$(C_L/C_D)\big|_{\text{Egress}}$ [-]	-6.90 %	**9.612**	5.49 %	13.45 %
$(C_L/C_D)\big|_{\text{Loiter}}$ [-]	-1.04%	**16.978**	0.36 %	5.34 %
Take-off weight [lb]	6.57 %	**5717**	-4.57%	-10.19 %
Range ingress [nm]	-0.13 %	**850**	0.07 %	0.21 %
Range egress [nm]	-1.30 %	**1842**	0.51%	0.63 %
Take-off distance [ft]	-3.16 %	**3783**	4.44 %	15.96 %
Landing distance [ft]	-6.92 %	**1695**	7.15 %	22.04 %

7.2. Mach egress and ingress impact

Table 7.2 shows the impact of varying Mach numbers on different variables during ingress and egress. It can be observed that as the Mach number increases, the lift-to-drag ratio during ingress decreases and

during egress increases. The take-off weight of the aircraft remains constant at all Mach numbers, but the range during ingress and egress decreases as Mach number increases, with the greatest reduction observed at $M = 0.95$. Additionally, the take-off, landing and lift-to-drag ratio during loiter distances remain constant at all Mach numbers.

Table 7.2: Mach ingress and egress impact on other variables.

	$M = 0.80$	$M = 0.86$	$M = 0.90$	$M = 0.95$
$(C_L/C_D)\big|_{\text{Ingress}}$ [-]	13.06 %	**13.84**	-10.24 %	-24.51 %
$(C_L/C_D)\big|_{\text{Egress}}$ [-]	20.24 %	**9.612**	-14.14 %	-33.37%
Take-off weight [lb]	0 %	**5717**	0%	0 %
Range ingress [nm]	8.27 %	**850**	-7.57 %	-19.66 %
Range egress [nm]	14.71 %	**1842**	-11.69 %	-29.23 %
Take-off distance [ft]	0 %	**3783**	0 %	0 %
Landing distance [ft]	0 %	**1695**	0 %	0 %

7.3. Aspect ratio impact

The aspect ratio value designed for the RADAR aircraft is 10. The effect of this value on other variables is given in table 7.3. When $AR = 9$, which is the value below the reference value, is considered as a general effect, its effect on other parameters was negative. In addition, when a value above the reference value ($AR = 11$ or 12) is considered, the negative and positive effects on other parameters remained very small. The reference value ($AR = 10$), which was chosen by examining the table and considering its effect on the value parameters, is the optimum value for the RADAR aircraft.

Table 7.3: Aspect ratio impact on other variables.

|	$AR = 9$	**$AR = 10$**	$AR = 11$	$AR = 12$
$(C_L/C_D)\big|_{\text{Ingress}}$ [-]	-2.46 %	**13.84**	-2.42 %	-2.40 %
$(C_L/C_D)\big|_{\text{Egress}}$ [-]	-3.33 %	**9.612**	-3.35 %	-3.36 %
$(C_L/C_D)\big|_{\text{Loiter}}$ [-]	-0.25 %	**16.978**	2.16 %	4.04 %
Take-off weight [lb]	-0.24 %	**5717**	0.34 %	0.77 %
Range ingress [nm]	-1.81 %	**850**	-2.1 %	-2.22 %
Range egress [nm]	-2.7 %	**1842**	-3.07 %	-3.20 %
Take-off distance [ft]	-0.33 %	**3783**	0.52 %	1.18 %
Landing distance [ft]	-0.93 %	**1695**	0.91 %	1.81 %

8 Cost Analysis

Cost analysis plays a crucial role in the design process, particularly when it comes to estimating the cost-effectiveness of the development, manufacturing and operation of the aircraft. Considering the target market and expected attrition rate, an economic evaluation is crucial. The cost analysis is thus divided into Research Development Test and Evaluation (RDTE) costs, production costs, and operating costs.[16]

8.1. Method Applied

To estimate the cost of developing an aircraft, a statistical method called the Cost-Estimating Relationship (CER) is used. This approach considers the tasks involved in designing, testing, and producing the aircraft, as well as labour rates and macroeconomic factors. The DAPCA-IV model utilizes a Consumer Price Index (CPI) relative to 2012 to estimate costs, but since it's difficult to estimate CPI for 2028, the CPI for 2023 is used. The Quantity Discount Factor (QDF) assumes that as the number of units produced increases, the cost per unit decreases. The Eastlake model, which employs a more realistic model, estimates QDF using the equation $\text{QDF} = \left(F_{\text{Exp}}\right)^{1.4427 \cdot \ln N}$, where Fexp represents experience effectiveness and N is the number of units produced. Figure: 8.1a shows the relationship between the number of units produced and QDF.
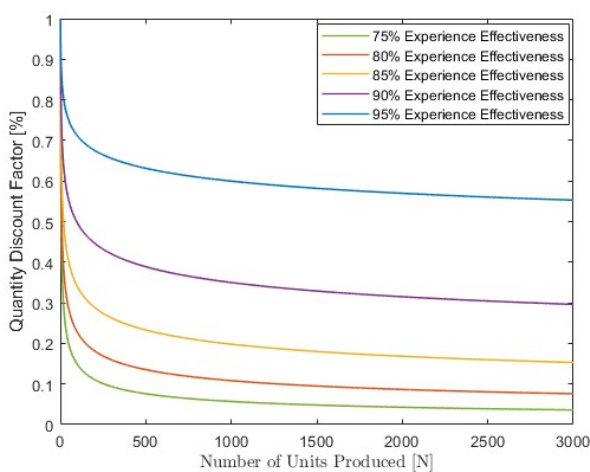
(a) Quantity Discount Factor vs Number of units produced.
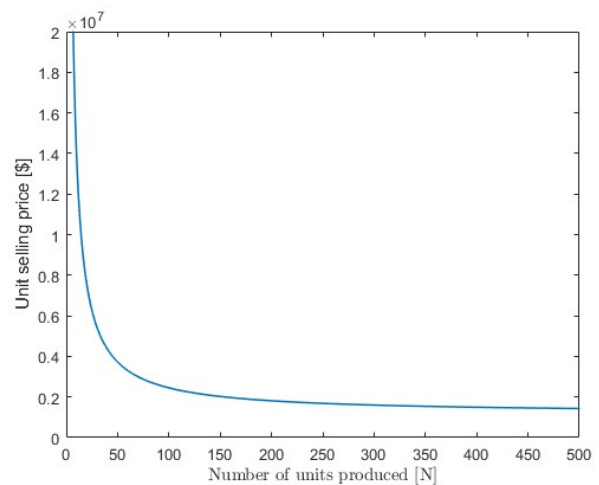
(b) Unit selling price vs Number of units produced.

The DAPCA-IV model requires a Consumer Price Index (CPI). Therefore the CPI 2023 used is 1.33 [38]. It should also be noted that N = 500 aircraft are expected to be manufactured during a 5-year period. Figure: 8.1b shows the number of aircraft to be manufactured during a five-year period and the amount of the discount.

8.2. Man-hour Calculation

The engineering, tooling, and manufacturing departments are three crucial parts of the project that should be estimated in terms of man hours. The engineering, tooling, and manufacturing man-hours are presented in Table:8.1. The man-hour calculation for RADAR aircraft has been found from the formulas below.[16]

$$H_{\text{ENG}} = 0.0396 \cdot W_{\text{airframe}}^{0.791} \cdot V_c^{1.526} \cdot N^{0.183} \cdot F_{\text{CERT}} \cdot F_{\text{CF}} \cdot F_{\text{COMP}} \cdot F_{\text{PRESS}} \tag{8.1}$$

Equation: 8.1 shows the number of engineering man-hours(H_{ENG}), W_{airframe} weight of the structural skeleton, V_C maximum level airspeed in KTAS, F_{CERT} certified as 14 CFR Part 23, F_{CF} simple flap system, F_{COMP} a factor to account for the use of composites in the airframe and F_{PRESS} represent the pressurization of the aircraft.

$$H_{\text{TOOL}} = 1.0032 \cdot W_{\text{airframe}}^{0.764} \cdot V_c^{0.899} \cdot N^{0.178} \cdot Q_m 0.066 \cdot F_{\text{TAPER}} \cdot F_{\text{CF}} \cdot F_{\text{COMP}} \cdot F_{\text{PRESS}} \tag{8.2}$$

Equation:8.2 shows the number of tooling man-hours (H_{TOOL}), Q_m represents the production rate in number of aircraft per month, F_{TAPER} represent the taper of the wing.

$$H_{\text{MFG}} = 9.6613 \cdot W_{\text{airframe}}^{0.74} \cdot V_c^{0.543} \cdot N^{0.524} \cdot F_{\text{CERT}} \cdot F_{\text{CF}} \cdot F_{\text{COMP}} \tag{8.3}$$

Equation8.3 shows the number of manufacturing man-hours.

Table 8.1: The engineering, tooling, and manufacturing man hours for 500 units.

Variable	Man hours [hours]
Number of Engineering Man-hours	365,507
Number of Tooling Man-hours	160,387
Number of Manufacturing Man-hours	987,706

8.3. Fixed costs

Fixed costs are expenses that do not change based on factors like production volume or sales volume. As production volume rises, fixed expenses help to reduce unit cost but, when output volume declines, the unit cost remains unchanged.

Fixed costs for RADAR aircraft include the total cost of tooling, the total cost of flight test operations, the total cost of development and support and the total cost of engineering.

$$C_{\text{TOOL}} = 2.0969 \cdot H_{\text{TOOL}} \cdot R_{\text{TOOL}} \cdot \text{CPI} \tag{8.4}$$

Equation:8.4 shows the total cost of tooling, (R_{TOOL}) represents the rate of tooling labour in $ per hour. The rate of tooling labour per hour was taken as 65\$ [38].

$$C_{\text{ENG}} = 2.0969 \cdot H_{\text{ENG}} \cdot R_{\text{ENG}} \cdot CPI \tag{8.5}$$

Equation 8.5 shows the total cost of engineering, (R_{ENG}) represents the rate of engineering labour in $ per hour. The rate of engineering labour per hour was taken as 92\$ [38].

$$C_{\text{DEV}} = 0.06458 \cdot W_{\text{empty}}^{0.873} \cdot V_c^{1.89} \cdot N_p^{0.346} \cdot \text{CPI} \cdot F_{\text{CF}} \cdot F_{\text{PRESS}} \cdot F_{\text{CERT}} \cdot F_{\text{COMP}} \tag{8.6}$$

Equation 8.6 shows the total cost of development support, N_p represents the number of prototypes. One prototype was considered.

$$C_{FT} = 0.009646 \cdot W_{\text{airframe}}^{1.16} \cdot V_H^{1.3718} \cdot N_P^{1.281} \cdot CPI \cdot F_{\text{CERT}} \tag{8.7}$$

Finally, equation 8.7 shows the total cost of flight test operations. Table 8.2 provides the fixed cost values for 500 RADAR aircraft that will be manufactured during a 5-year period.

Table 8.2: Total fixed cost for 500 units.

Variable	Cost per unit [$]
Total cost of engineering	93,779,962
Total cost of tooling	29,072,798
Total cost of development support	4,286,409
Total cost of flight test operations	149,340
Total fixed cost	127,288,510

8.4. Variable costs

Variable costs are costs that vary depending on variables such as production or sales volume. Variable costs increase as the amount of production increases, and they decrease when the amount of production decreases.

$$C_{\text{MFG}} = 2.0969 \cdot H_{\text{MFG}} \cdot R_{\text{MFG}} \cdot \text{CPI} \qquad (8.8)$$

Equation 8.8 shows the total cost of manufacturing, R_{MFG} represents the rate of manufacturing labour per hour and which was taken 58 \$ [38]

$$C_{QC} = 0.13 \cdot C_{\text{MFG}} \cdot F_{\text{CERT}} \cdot F_{\text{COMP}} \qquad (8.9)$$

From the Equation:8.9 shows total cost of quality control, F_{CERT} represent certified as a 14 CFR Part 23 aircraft and $F_{\text{COMP}} = 1 + 0.5 f_{\text{comp}}$ represent a factor to account for the use of composites in the airframe.

$$C_{MAT} = 24.896 \cdot W_{\text{airframe}}^{0.689} \cdot V_H^{0.624} \cdot N^{0.792} \cdot CPI \cdot F_{\text{CERT}} \cdot F_{\text{CF}} \cdot F_{\text{PRESS}} \qquad (8.10)$$

Equation 8.9 shows the total cost of materials, F_{CF} represents a simple flap system and F_{PRESS} represents the pressurization of the aircraft. A total of \$15,000 per aircraft was approved as the avionics cost.

$$C_{PP} = 1035.9 \cdot N_{\text{pp}} \cdot T^{0.8356} \cdot CPI \cdot N \qquad (8.11)$$

Equation 8.11 shows the total cost of the engine, N_{pp} represents the number of engines and a turbofan engine was chosen as the engine type. T represents the rated trust.

Table 8.3: Total variable cost for 500 aircraft.

Variable	Cost per unit [\$]
Total cost of engine	378,332,479
Total cost of manufacturing	159,765,404
Total cost of quality control	21,288,740
Total cost of materials	21,247,267
Total cost of avionics	7,500,000
Total variable cost	588,133,892

8.5. Break-even analysis

The goal of break-even analysis is to identify the point at which income generated equals expenditures expended. To estimate the point at which income from aircraft operations equals the overall costs paid in running an aircraft. Together with the variable costs like fuel and other operating expenses, this also covers fixed expenditures like the price of the aircraft, insurance, crew salary, and maintenance expenses. Break-even analysis values for RADAR aircraft are given in Table 8.4 and Figure 8.2.

Table 8.4: Break even analysis.

Variable	Cost per unit [$]	Aircraft to break even
Revenue1 (total cost)	1,430,800	500
Revenue2 (total cost+%10 profit)	1,573,900	320
Revenue3 (total cost+%20 profit)	1,717,000	235
RADAR Production Price	1,430,800	
RADAR Selling Price	1,717,000	

A break-even analysis is performed to understand how many aircraft need to be sold before a profit is made and thus when investors will start recuperating their investments.The break-even analysis for 500 aircraft is given in Figure:8.2.
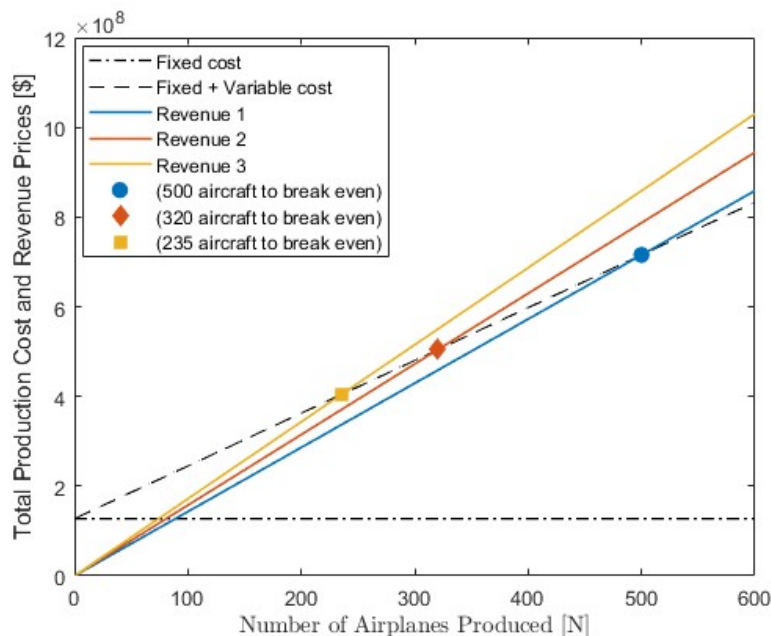

Figure 8.2: Break even analysis for 500 aircraft

8.6. Total annual costs and Operational costs

The total annual cost for aircraft depends on many factors. These factors include aircraft type, service life, maintenance requirements, fuel consumption, operating costs, crew expenses, and insurance costs.

$$C_{AP} = F_{\mathsf{MF}} \cdot R_{\mathsf{AP}} \cdot Q_{\mathsf{FLGT}} \tag{8.12}$$

Equation:8.12 shows the total maintenance cost, F_{MF} are the maintenance to flight hour ratio and equal to 0.35, R_{AP} = $\$60$ per hour is the hourly rate for a certified airframe and powerplant mechanic and Q_{FLGT} = 1460 is the number of flight hours per year. It was calculated that it would fly for four hours every day for a year.

$$C_{\mathsf{STOR}} = 12 \cdot R_{\mathsf{STOR}} \tag{8.13}$$

Equation:8.13 shows the storage cost, R_{STOR} represents the storage rate which was assumed to be $\$250$ per month.

$$C_{FUEL} = \frac{BHP_{\mathsf{CRUISE}} \cdot SFC_{\mathsf{CRUISE}} \cdot Q_{\mathsf{FLGT}} \cdot R_{\mathsf{FUEL}}}{6.5} \tag{8.14}$$

Equation 8.14 shows the annual fuel cost, BHP_{CRUISE} represent the typical horsepower during cruise, SFC_{CRUISE} represents the typical specific fuel consumption during cruise, R_{FUEL} price of fuel in gallon on the date of the 24nd of April 2023 was of R_{FUEL}=$ 3.86/gallon.

$$C_{\mathsf{INS}} = 500 + 0.015 \cdot C_{AC} \tag{8.15}$$

Equation 8.15 shows the annual insurance cost, C_{AC} represents the insured value of the aircraft. This equals the total cost of the aircraft.

$$C_{\mathsf{INSP}} = 7300\$ \tag{8.16}$$

Equation 8.16 represents the annual inspection cost.

$$C_{\mathsf{OVER}} = 5 \cdot N_{PP} \cdot Q_{\mathsf{FLGT}} \tag{8.17}$$

Equation 8.17 shows the engine overhaul cost.

For the crew cost, the number of crew members required to operate the aircraft is taken as 3, the hourly rate of crew per hour is taken 50 $.

The cost per each hour flown is as follows using the formula $C_{HR} = \frac{C_{\text{YEAR}}}{Q_{\text{FLGT}}}$ where C_{YEAR} using the following Equation :

$$C_{\text{YEAR}} = C_{AP} + C_{STOR} + C_{\text{FUEL}} + C_{\text{INS}} + C_{\text{INSP}} + C_{\text{OVER}} \tag{8.18}$$

The values used in calculating the total annual cost for the RADAR aircraft are given in Table 8.5.

Table 8.5: Total annual cost.

Variable	Cost per unit [$]
Maintenance Cost	30,660
Storage cost	3,000
Annual fuel cost	623,275
Annual insurance cost	21,963
Annual inspection cost	7,300
Engine overhaul fund	7,300
Total Yearly Cost	693,488
Cost per Flight Hour	475

8.7. Life cycle emissions

Estimating the life cycle emissions of the aircraft involves assessing the environmental impact that the aircraft will have through its entire life cycle, from the extraction of the raw materials to the end of its useful life. Thus, emissions from production, in-service and disposal of the aircraft will have to be considered. The following greenhouse gases (GHG) are produced by the production of aluminium [39], steel [40], carbon fibre [41] and by burning fuel [42]: carbon dioxide (CO_2), methane (CH_4) and nitrous oxide (N_2O). While the following are produced only from the manufacturing of aluminium: tetrafluoromethane (CF_4) and hexafluroethane (C_2F_6) [43] Using the Global Warming Potential (GWP) and Assessment Report 5 (AR5) [44], the number of emissions produced by the gases could be determined by

$$emission = \frac{CO_2}{GWP} \cdot weight, \tag{8.19}$$

where $C0_2$ is the amount of $C0_2$ produced per pound of the material or fuel [45]. The total emissions for the different phases are given in Table 8.6

Table 8.6: Lifecycle emission of the different phases of an aircraft life.

	Weight [lbs]	$C0_2$ [lbs^{-1}]	$C0_2$ [lbs]	CH_4 [lbs]	N_2O [lbs]	CF_4 [lbs]	C_2F_6 [lbs]
GWP			1	28	265	6,630	11,100
Production (5-year period)							
Aluminium	843500	1.8	1518300	54225	5729	229	136
Steel	73000	4.07	297110	10611	1121	~	~
Carbon fibre	25600	20	512000	18285	1932	~	~
Total			2327410	83122	8783	229	136
In-service (1-year period)							
Fuel	888720	6.97	6194378	221228	23375	~	~
End of service							
The components will either be reused, donated or recycled.							

Water vapour accounts for 30 % of the exhaust emission. Although water vapour on its own is not dangerous, it has the indirect effect of creating contrails. The contrails trap the infrared rays resulting in a warming-up effect that is three times greater than the warming-up impact of carbon dioxide [42].

9 Conclusion

In response to the request for proposal from the AIAA due to the increase in frequency and intensity of natural disasters across the world, the RADAR aircraft was designed and presented. The aircraft was able to achieve the main mission goals of search, identify and deliver life-saving packages to victims of natural disasters. The aircraft design and the use of some innovative technologies allowed it to achieve the mission requirements. The aircraft was designed to reach the search area as quickly as possible and then loiter for many hours thus allowing a large area to be searched. A long range thermal optical imaging camera was installed in order to identify victims from the loiter altitude. A guided parachute system was implemented in order to to deliver the packages as close to the victims as possible.

The various components of the aircraft were sized and designed, ultimately leading to a light aircraft according to FAA weight classes. The final configuration is a high wing, conventional tail, internal fuselage-mounted turbofan engine aircraft with a retractable tricycle landing gear.

The static and dynamic stability was computed and the aircraft was shown to be stable under all conditions. The performance of the aircraft was computed and then optimized for the different flight missions. Thus, allowing the aircraft to loiter for a long time while arriving at the disaster scene as quickly as possible. A trade-off study was conducted on the critical components and parameters of the aircraft, this led to a high aspect ratio wing being selected which improved the performance as a longer range could be achieved. A complete cost analysis was performed and the design was found to be economically viable.

The next logical step would be to pursue a deeper CFD analysis. While ensuring that a consistent review of the new and innovative technologies is performed to evaluate whether they would improve the performance of the aircraft. A more detailed trade-off study can be performed to investigate if a more optimum configuration exists. In conclusion, RADAR is an economically viable aircraft to perform search, identify and deliver missions.

Bibliography

[1] National Centers for Environmental Information. Natural Hazards Viewer. 2022. url: `https://www.ncei.noaa.gov/maps/hazards/` (visited on 04/16/2023).

[2] Alberto Cuadra and Craig Whitlock. How Drones Are Controlled. 2014. url: `https://www.washingtonpost.com/wp-srv/special/national/drone-crashes/how-drones-work/` (visited on 03/28/2023).

[3] RF WORLD. Advantages of Satellite communication and disadvantages of Satellite communication. 2012. url: `https://www.rfwireless-world.com/Terminology/Advantages-and-Disadvantages-of-satellite-communication.html` (visited on 03/28/2023).

[4] The Business Research Company. Satellite Communication Global Market Report 2023. 2023. url: `https://www.thebusinessresearchcompany.com/report/satellite-communication-global-market-report#:~:text=The%5C%20satellite%5C%20communication%5C%20market%5C%20size,used%5C%20in%5C%20advanced%5C%20space%5C%20operations.` (visited on 02/24/2023).

[5] Acal BFi. MWIR or LWIR thermal cameras for surveillance applications? 2021. url: `https://www.acalbfi.com/sites/default/files/2021-09/MWIR_or_LWIR.pdf` (visited on 02/21/2023).

[6] Teledyne Flir. Star SAFIRE® 380-HD. url: `https://www.flir.com/products/star-safire-380-hd/` (visited on 02/21/2023).

[7] Mayo Clinic Staff. Water: How much should you drink every day? 2022. url: `https://www.mayoclinic.org` (visited on 03/28/2023).

[8] Airborne Systems. Family of Guided Precision Aerial Delivery System. 2016. url: `https://airborne-sys.com/wp-content/uploads/2016/09/ASG_JPADSFamily_20170201-French-1.pdf` (visited on 03/25/2023).

[9] CargoFlash. Do all commercial cargo aviation companies use pressurised planes? 2021. url: `https://www.cargoflash.com/blog/Do-all-commercial-air-freighters-use-pressurised-planes-in-2022` (visited on 04/25/2023).

[10] Pilot Institute. Aircraft Pressurization Systems: How They Work and When They Are Required. 2021. url: `https://pilotinstitute.com/aircraft-pressurization-systems/` (visited on 04/25/2023).

[11] Gulfstream. The Gulfstream G650 Family. url: `https://www.gulfstream.com/en/aircraft/gulfstream-g650er/` (visited on 02/24/2023).

[12] Dassault Aviation. Falcon 8X. url: `https://www.dassault-aviation.com/en/civil/falcon-family/falcon-8x/` (visited on 02/24/2023).

[13] Bombardier. Global 7500. url: `https://businessaircraft.bombardier.com/en/aircraft/global-7500#bba-pdp-section-1` (visited on 02/24/2023).

[14] Daniel P. Raymer. Aircraft Design: A Conceptual Approach. 6th ed. American Institute of Aeronautics Ast., 2010.

[15] Egbert Torenbeek. Synthesis of subsonic airplane design. Delft University Press, 1976.

[16] GUDMUNDSSON Snorri. General aviation aircraft design: applied methods and procedures. First edition. ; Waltham, MA: Butterworth-Heinemann, 2014.: Oxford, 2014.

[17] Mohammad H. Sadraey. Aircraft Design: A Systems Engineering Approach. 1st. Wiley, 2012. isbn: 978-0-470-38241-2.

[18] Koen Hillewaert and Remy Princivalle. Introduction to airbreathing propulsion systems. Aerospace design project, Uliège, 2022.

[19] Nihad E. Daidzic. "Estimation of Performance Airspeeds for High-Bypass Turbofans Equipped Transport-Category Airplanes". In: Journal of Aviation Technology and Engineering 5.2 (2016).

[20] European Union Aviation Safety Agency. Type Certificate Data Sheets. 2023. url: `https://www.easa.europa.eu/en/document-library/type-certificates` (visited on 04/24/2023).

[21] Matthias Bartel and Trevor Young. "Simplified Thrust and SFC Calculations of Modern Two-Shaft Turbofan Engines for Preliminary Aircraft Design". In: 7th AIAA ATIO Conf 2 (2012), p. 8.

[22] Dassault Aviation. CO2e - Methods of Calculation. url: `https://www.dassault-aviation.com/fr/passion/avions/dassault-militaires/alpha-jet/` (visited on 02/14/2023).

[23] Nationwide fuels. 9 Facts About Kerosene You Might Not Know. 2013. url: `https://www.nationwidefuels.co.uk/oil-guides/facts-about-kerosene-you-might-not-know/` (visited on 02/17/2023).

[24] Wikipedia. Nose cone design. 2018. url: `https://en.wikipedia.org/wiki/Nose_cone_des ign` (visited on 11/18/2022).

[25] M.F. Ashby. Material selection in mechanical design. 2011.

[26] Katharina Fromm. Matériaux pour les batteries du futur. 2019. url: `https://www.nfp-energie .ch/fr/projects/1019/` (visited on 02/17/2023).

[27] David Carwile. Which Aircraft Parts Are Replaced the Most Frequently. 2022. url: `https://www .aviationaxis.com/blog/which-aircraft-parts-are-replaced-the-most-frequent ly/` (visited on 04/26/2023).

[28] L. Noels. Conceptual design. Aerospace design project, Université de Liège, 2022-2023.

[29] G. Dimitriadis. Flight Dynamics and Control course. University of Liège, 2022-2023.

[30] R. D. Finck. USAF (United States Air Force) Stability and Control DATCOM (Data Compendium). MC-DONNELL AIRCRAFT CO ST LOUIS MO, 1977.

[31] M. V. Cook. Flight Dynamics Principles: A Linear Systems Approach to Aircraft Stability and Control. Elsevier, 2018.

[32] Adrien Crovato et al. "A discrete adjoint full potential formulation for fast aerostructural optimization in preliminary aircraft design". In: Aerospace Science and Technology 138 (2023), p. 108332. doi: `https://doi.org/10.1016/j.ast.2023.108332`. url: `https://gitlab.uliege.be/a m-dept/dartflo`.

[33] H. Schlichting and K. Gersten. Boundary-Layer Theory. 8th ed. Springer-Verlag Berlin Heidelberg, 2000.

[34] John Clauser. "The turbulent boundary layer". In: Advances in Applied Mechanics 4 (1956), pp. 1–51.

[35] FAR Part 23 - Airworthiness standards: Normal, utility, acrobatic and commuter category airplanes. Tech. rep. Federal Aviation Administration, 2016.

[36] Petrol Plaza. How Large Aircraft Fuel Up. 1997. url: `https://www.petrolplaza.com/knowled ge/1796` (visited on 04/26/2023).

[37] SKYbrary Aviation Safety. Descend, Approach and Landing. 2021-2023. url: `https://www.sky brary.aero/descend-approach-and-landing` (visited on 04/24/2023).

[38] United States Department of Labor. U.S. BUREAU OF LABOR STATISTICS. 2023. url: `https://w`
      `ww.bls.gov/` (visited on 04/24/2023).

[39] United States Environmental Protection Agency. Aluminum Industry. 2022. url: `https://www.e`
      `pa.gov/f-gas-partnership-programs/aluminum-industry` (visited on 02/21/2023).

[40] Sustainable Ships. What is the carbon footprint of steel? url: `https://www.sustainable-shi`
      `ps.org/stories/2022/carbon-footprint-steel` (visited on 02/21/2023).

[41] M. Shioya and T. Kikutani. Synthetic Textile Fibres: Non-polymer Fibres. Woodhead Publishing,
      2015.

[42] Jeff Overton. Issue Brief | The Growth in Greenhouse Gas Emissions from Commercial Aviation.
      2022. url: `https://www.eesi.org/papers/view/fact-sheet-the-growth-in-greenhou`
      `se-gas-emissions-from-commercial-aviation` (visited on 02/21/2023).

[43] Aluminium France. Climate and carbon footprint. url: `https://www.aluminium.fr/en/stake`
      `/climate-and-carbon-footprint/` (visited on 02/21/2023).

[44] Greenhouse gas protocol. Global Warming Potential Values. url: `https://ghgprotocol.org`
      `/sites/default/files/Global-Warming-Potential-Values` (visited on 03/21/2023).

[45] Climatiq. CO2e - Methods of Calculation. url: `https://www.climatiq.io/docs/guides/co2`
      `e-calculation` (visited on 02/21/2023).